Development of Computational Models of Pedunculopontine Nucleus Stimulation for Clinical Trials and Mechanistic Studies

A Thesis
SUBMITTED TO THE FACULTY OF
UNIVERSITY OF MINNESOTA
BY

Laura M. Zitella Verbick

IN PARTIAL FULFILLMENT OF THE REQUIREMENTS
FOR THE DEGREE OF
DOCTOR OF PHILOSOPHY

Advisor: Matthew D. Johnson

March 2016

Acknowledgements

First and foremost, I would like to thank my advisor, Matt Johnson. I couldn't have completed my Ph.D. without your expert guidance and mentorship. You are one of the smartest and most humble people I know, and I have learned so much from you. Your contagious excitement, optimism, and unwavering confidence in me has helped me through many challenges. I felt very lucky to have an advisor that was not only supportive of me in the research lab, but also invested in my future, making sure I had the necessary skills and experiences to reach my goals.

Thank you to my committee members and collaborators Jerry Vitek, Noam Harel, and Hubert Lim for all of your advice, support, and contributions to this thesis. My work has greatly benefited from your expertise and assistance. Also thanks to Ken Baker, a member of my preliminary oral exam committee, for your guidance throughout this thesis.

Thank you to members of the Vitek and Baker labs, especially Heather Hudson and Jianyu Zhang, for vital help with the experimental aspects of this thesis. Thank you also to Yuval Duchin for your assistance with the diffusion tractography aspects of this thesis and to Paul Yager for the PET data analysis. A special thank you to the undergraduates that contributed many hours to these projects: Katelynn Brintz, Katerina Paone, Kelsey Sievert, and Valeria Beletsky. Finally, thank you to all of the members of the NRTL lab, past and present, for all of your help, support, and comradery: Ben Teplitzky, Allison Connolly, Maureen Keane, Filippo Agnesi, Joe Xiao, David Zhang, Edgar Pena, Ed Bello, Logan Grado, Kevin Mohsenian, and Julia Slopsema.

Thank you to my family and friends. I truly could not have accomplished this without your love and support. Thank you to my parents, brother, and sisters for your constant encouragement, even from afar. Thank you to all of my fellow graduate students and my friends for being an incredible support system. Thank you especially to Katie and

Kerianne for keeping me sane through the many struggles of graduate school. Finally, thank you to my husband Zach for your faithful support, boundless love and patience.

Finally, I gratefully acknowledge the funding sources that made this work possible: the National Science Foundation IGERT: Systems Neuroscience fellowship (IGERT DGE-1069104) and the MNDrive Brain Conditions fellowship. Also to the grants that supported this research: National Institutes of Health (R01-NS081118, R01-NS085188, R01-EB008645, P41-EB015894, P30-076408, Human Connectome Project U54-MH091657, NS-068231), Michael J. Fox Foundation.

Dedication

This thesis is dedicated to my parents, Sue and Vince,

…for instilling in me a love and appreciation for science,

…for always encouraging me to follow my dreams, and

…for your endless love and support.

Abstract

Deep brain stimulation (DBS) in the pedunculopontine nucleus (PPN), a component of the mesencephalic locomotor region in the brainstem, has been proposed to alleviate gait and balance disturbances associated with Parkinson's disease; however, clinical trials results have been highly inconsistent. Such variability may stem from inaccurate targeting in the PPN region, modulation of fiber pathways implicated in side effects, and lack of understanding of the modulatory effects of DBS in the brainstem. Here, we describe the development and refinement of computational models that can predict the neuromodulatory effects of PPN-DBS in both the non-human primate and human. These models included (1) brain atlas-based models that combined detailed biophysically realistic neuron and axon models with a finite element model simulating the voltage distribution in the brain during DBS, (2) high-field 7T MRI techniques to visualize and create volumetric morphologies of structures in the brainstem for use in the models, and (3) clinically relevant subject-specific computational models that incorporate the anisotropic conductivity of the brain tissue. Based on the validated results of these models, we can conclude that the neuronal pathways modulated by DBS in the brainstem are highly sensitive to both lead location and stimulation parameters. These computational models of DBS will be useful in future clinical trials, both prospectively to plan DBS lead trajectories and improve stimulation titration and retrospectively to investigate the underlying mechanisms of therapy and side effects of stimulation.

Table of Contents

List of Tables

List of Figures

List of Abbreviations

AC	Anterior commissure
AChE	Acetylcholine esterase
BET	Brain extraction tool
ChAT	Choline acetyl transferase
ChR2	Channelrhodopsin-2
CN	Cuneiform nucleus
CT	Computed tomography
CTG	Central tegmental tract
DBS	Deep brain stimulation
DOF	Degrees of freedom
DWI	Diffusion weighted imaging
FDG	Fludeoxyglucose
FDG-SUV	Fludeoxyglucose-standard uptake values
FEM	Finite element model
FLUT	Paranode main segments
FOG	Freezing of gait
FOV	Field of view
GP	Globus pallidus
GPi	Globus pallidus internal segment
IC	Inferior colliculus
IPG	Implantable pulse generator
LL	Lateral lemniscus
MGB	Medial geniculate body
ML	Medial lemniscus
MLF	Medial longitudinal fasciculus
MLR	Mesencephalic locomotor region
MPTP	1-methyl-4-phenyl-1,2,3,6-tetrahydropyridine
MRI	Magnetic resonance imaging
MYSA	Myelin attachment segments
NHP	Non-human primate
NODE	Node of Ranvier
ON	Oculomotor nerve
ONu	Oculomotor nucleus
PAG	Periaqueductal gray

PBS	Phosphate buffered saline
PET	Positron emission tomography
PC	Posterior commissure
PD	Parkinson's disease
PF	Pallidofugal tract
PI	Postural instability
PnO	Pontine reticular formation
PPN	Pedunculopontine nucleus
PPNc	Pedunculopontine nucleus pars compacta
PPNd	Pedunculopontine nucleus pars dissipata
PPTg	Pedunculopontine tegmental nucleus
REM	Rapid eye movement
RN	Red nucleus
SCP	Superior cerebellar peduncle
SN	Substantia nigra
SNc	Substantia nigra pars compacta
SNr	Substantia nigra pars reticulata
SPTh	Spinothalamic tract
STIN	Internode segments
SWI	Susceptibility-weighted imaging
STN	Subthalamic nucleus
T1-W	T1-weighted
T2-W	T2-weighted
UPDRS	Unified Parkinson's disease rating scale
VA	Ventralis anterior
VLo	Ventralis lateralis pars oralis
VPLc	Ventralis posterior lateralis pars caudalis
VPLo	Ventralis posterior lateralis pars oralis
VPM	Ventral posteromedial nucleus of thalamus
YFP	Yellow fluorescent protein
ZI	Zona incerta

1 Introduction

1.1 Pathophysiology and Treatment of Parkinson's disease

Parkinson's disease (PD) is a neurodegenerative disorder caused by the progressive loss of neurons within the brain, including but not limited to dopamine-producing neurons within the substantia nigra pars compacta (SNc) and cholinergic neurons within the pedunculopontine nucleus (PPN). In the end stages of the disease Lewy bodies and Lewy neurites overtake neurons in the thalamus and neocortex [1]. PD is characterized by several cardinal motor symptoms including muscle rigidity, akinesia, tremor, bradykinesia, postural instability, and freezing of gait. While most of the symptoms are associated with dopaminergic depletion and its effects on the basal ganglia, gait and postural control abnormalities are hypothesized to result from the degeneration of cholinergic PPN neurons [2], [3].

However, the role of PPN in PD symptoms, based on a changing input from basal ganglia structures, is highly debated. One thought is that basal ganglia output is increased, therefore causing an increase in GABAergic inhibitory input to the remaining brainstem cholinergic and non-cholinergic neurons. This in turn may underlie problems with initiating programmed movements, akinesia, and other posture and gait symptoms [4]. Postural problems may also stem from the reduced number of cholinergic PPN neurons as PD progresses causing problems with multi-sensory integration in thalamus [5].

The most prevalent treatment for the motor symptoms of Parkinson's disease is dopamine-replacement drugs such as levodopa; however, with long term use and increased dosages these drugs may elicit side effects such as dyskinesias. Additionally, aspects of gait and postural control are often not well managed with dopamine-replacement therapy. Indeed, gait and balance disturbances can greatly affect quality of life, as fall-related injuries can significantly burden both the patients and their families.

1.1.1 Deep Brain Stimulation for Parkinson's disease

Deep brain stimulation (DBS) is a surgical treatment option for PD, which is used in conjunction with dopamine-replacement therapy, when medication alone leads to less time in the therapeutic 'on' state and increased incidence of dyskinesias. In many cases, a lower dosage of medication is possible during DBS treatment. DBS is an invasive neurosurgical procedure in which a four electrode contact lead is implanted through a cranial burr hole and into a target brain region exhibiting pathophysiological activity related to the expression of PD motor signs, usually the subthalamic nucleus (STN) or globus pallidus internal segment (GPi). Prior to the procedure, magnetic resonance imaging (MRI) is obtained to assist in localizing the target structure. Additionally, microelectrode recordings map the target region to ensure an accurate lead placement in case brain shift has occurred during the surgery. After several weeks of recovery time, the patient returns to the surgical center for subcutaneous placement of the implantable pulse generator (IPG) below the clavicle and tunneling of the extension cable under the skin to connect the DBS lead to the IPG. Following implantation, an initial programming session is conducted in which a clinician stimulates through each contact or combination of contacts to find the stimulation setting that most optimally treats the patient's symptoms without evoking side effects. Usually, patients return to the clinic periodically for adjustments of these settings as their disease progresses.

1.1.2 Why Focus on PPN?

Stimulating FDA-approved DBS targets for Parkinson's disease (STN, GPi) can markedly reduce motor symptoms of tremor, rigidity, and bradykinesia. However, problems with balance, posture, and gait are not treated adequately in many patients. STN DBS has been shown to play a role in amplitude scaling such as improving gait hypokinesia by increasing stride length [6]–[10]. In many cases, the effects of STN DBS on gait are similar to those of suprathreshold doses of L-dopa; however, studies have also reported a fading of the gait benefits from STN DBS over time, which is possibly a result of disease progression or suboptimal programming [11]. In fact, a survey found that 42% of patients with PD reported a postoperative worsening of gait after STN DBS, with

increased risks of falls and freezing of gait [12]. It is possible that this worsening was due to suboptimal stimulation settings that accentuated asymmetry in limb coordination [11]. In this case, one could remedy this issue by adjusting stimulation settings appropriately; this was done in one study that showed a reduction in freezing episodes when the frequency of STN stimulation was reduced to 60 Hz after gait disorders developed [13].

GPi DBS has also been shown to improve gait parameters, but long term studies evaluating the effectiveness of GPi DBS on gait symptoms over time are lacking [11]. A review of clinical trials that evaluated gait following DBS found that both STN and GPi DBS improved gait parameters and standing postural control, however their effects on postural control during gait and anticipatory postural adjustments either worsened (STN) or had no change (GPi) [14]. For this reason, brain regions known to be involved in gait and postural control, such as PPN, are being investigated as potential targets for treatment of these motor sign with DBS.

1.2 Anatomy of PPN area

The mesencephalic locomotor (MLR) region, located in the posterior midbrain, is composed of the cuneiform and pedunculopontine nucleus. The cuneiform nucleus (CN) lies dorsal to PPN, while the locus coeruleus is on the caudal pole and the retrorubral field is positioned rostrally. The inferior colliculus (IC) also lies dorsal to PPN, while the pontine reticular formation (PnO) is dorsal and caudal to PPN [15]. The anatomical locations of these structures is generally similar for rats, cats, non-human primates (NHPs), and humans, though slight variability is present. However, the circuitry and distribution of neurons in the PPN varies between species. There are also differences in nomenclature, with the pedunculopontine nucleus being referred to as the pedunculopontine tegmental nucleus (PPTg) in some human and rodent studies and atlases [16], [17]. This thesis will refer to the PPN of the non-human primate (NHP), unless otherwise specified.

Several different fiber tracts course through and near the MLR, which when stimulated could lead to side effects or potential interference with modulation of PPN during PPN-

DBS. The fibers of the superior cerebellar peduncle (SCP) partially course through the medial portion of the PPN as they travel ventrally from the deep cerebellar nuclei before decussating in the midbrain and projecting to the red nucleus and ventral posterior lateral pars oralis (VPLo) nucleus of thalamus. It has also been shown that SCP has collaterals that terminate in PPN, suggesting that PPN is an interface between the cerebellum and basal ganglia [18]. Because of this, it is largely unknown whether the effect of stimulating SCP during PPN DBS is beneficial or detrimental to the treatment of gait disorders [19], [20]. Also medial of the PPN is the central tegmental tract (CTG), which contains fibers that descend from the parvocellular region of the red nucleus (RN) to the accessory nuclei of the inferior olive [21], [22]. Stimulation or lesioning of this tract is associated with palatal myoclonus, a spasm of the palatal muscles on the roof of the mouth [23], known to occur when there is disconnect within a loop that involves the CTG, inferior olive, contralateral dentate nucleus and ipsilateral RN [24].

The medial lemniscus (ML), a pathway involved in proprioception, vibration, and fine touch, originates in the dorsal column nuclei and projects via the gracile and cuneate nuclei to the ventral posterior lateral pars caudalis (VPLc) nucleus of thalamus [25]. Stimulation of the ML might cause paresthesias, a tingling sensation according to the somatotopic area activated within ML. Nearby is the lateral lemniscus (LL), a portion of the ascending auditory pathway, which extends from the cochlear and superior olivary nuclear complex to the inferior colliculus and medial geniculate body (MGB). Stimulation of the LL may elicit a buzzing sound specific to the auditory frequency modulated within LL. Also lateral of PPN is the spinothalamic tract (SPTh), responsible for carrying information about pain, temperature and crude touch to the VPLc nucleus of thalamus. Stimulation of this pathway is thought to cause sensations of warmth in PPN-DBS patients, though perceptions of crude touch and pain could also be elicited in theory.

The rubrospinal tract passes medioventrally of PPN, originating in the magnocellular part of the RN and descending to the contralateral part of the spinal cord. Contralateral facial pulling and blinking are the side effects of current spread to this tract. Mediodorsally of PPN, the medial longitudinal fasciculus (MLF) traverses from the abducens nucleus to

the oculomotor nuclear complex, connecting the neurons controlling the lateral rectus muscle (abducens) with those controlling the medial rectus (oculomotor nucleus (ONu)). This pathway is important for lateral gaze and may cause oscillopsia if stimulated.

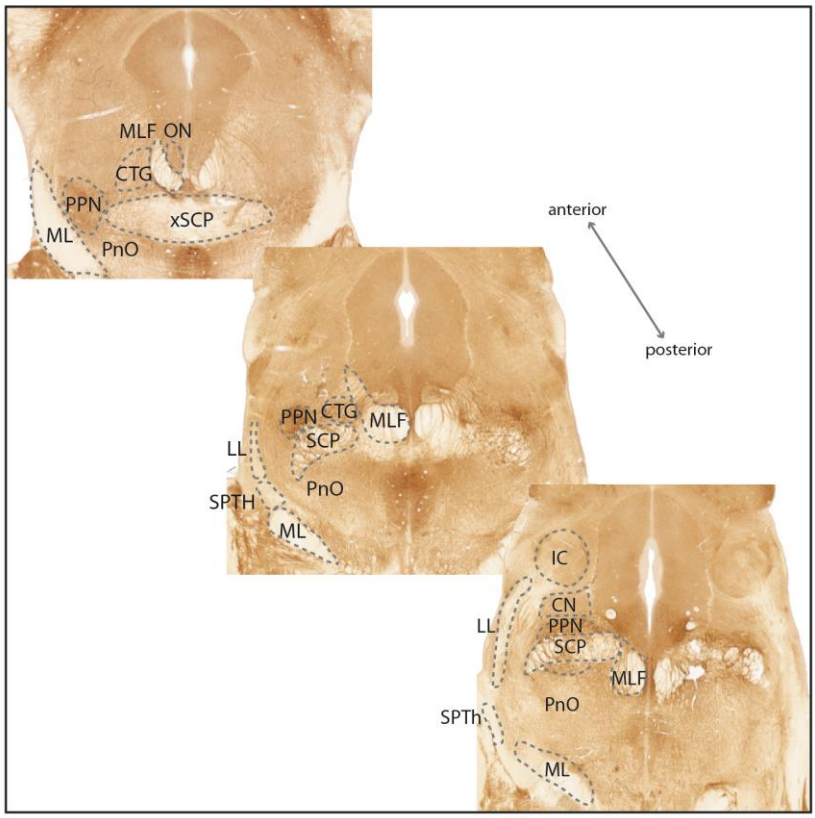

Figure 1. Anatomy surrounding the pedunculopontine nucleus in the non-human primate**.**
Nuclei are outline in a solid line, while fiber pathways are outlined in a dashed line. Three slices are shown, progressing from an anterior slice at the level of the decussation of the superior cerebellar peduncle (xSCP) in the upper left hand corner to the level of the inferior colliculus (IC) in the lower right hand corner. Cuneiform nucleus (CN), Central tegmental tract (CTG), Lateral lemniscus (LL), Medial lemniscus (ML), Medial longitudinal fasciculus (MLF), Oculomotor nucleus (ONu), Pontine reticular formation (PnO), Pedunculopontine nucleus (PPN), Superior cerebellar peduncle (SCP), Spinothalamic tract (SPTh)

1.3 Functional anatomy of the PPN area

1.3.1 Internal Structure

Several different cell types have been identified within the PPN area. Cholinergic neurons are the most commonly mentioned in the literature, but non-cholinergic neuron types including glutamatergic, GABAergic, noradrenergic, dopaminergic, and peptidergic are also present [26]–[31]. Historically, the PPN has been divided into two different regions: the pars compacta (PPNc) and the pars dissipata (PPNd). The PPNc is a region

of clustered neurons in the dorsolateral part of the caudal PPN, most of which are cholinergic (90%) [32]; however, only thirty percent of the total cholinergic neurons in PPN are located in the PPNc [33]. In PD patients, there is a 50% degeneration of these cholinergic PPNc neurons [34], [35]. The second most numerous cell type in the PPN, the glutamatergic, is found in the PPNd. Interestingly, almost half of the PPN cells in NHPs (40%) have been found to be both glutamatergic and cholinergic [26].

1.3.2 Electrophysiological Properties

Intracellular recordings have characterized at least two different PPN cell types based on their electrophysiological membrane properties. Type I neurons, which are thought to be glutamatergic, are characteristically bursty. These bursting action potentials can be elicited in response to either excitatory or inhibitory input [36]. These neurons are thought to be involved in gait initiation, specifically in phasic pace-setting. Further, these neurons may contribute to basal ganglia control of gait initiation, as GPi and substantia nigra pars reticulate (SNr) project to non-cholinergic PPN neurons and these neurons in turn project to the spinal cord [4].

Type II neurons have a slower, repetitive firing pattern, firing single action potentials that are followed by a large afterhyperpolarization. These neurons are located in rostral and central PPN, where half are characterized as cholinergic. It is hypothesized that these neurons are involved in pace-setting, or controlling the velocity of steady-state gait [4]. Both types of neurons have been shown to exhibit changes in firing rate during contralateral passive limb movement [37]. Additionally, some groups have found a third type of PPN neurons that display characteristics of both type I and type II neurons.

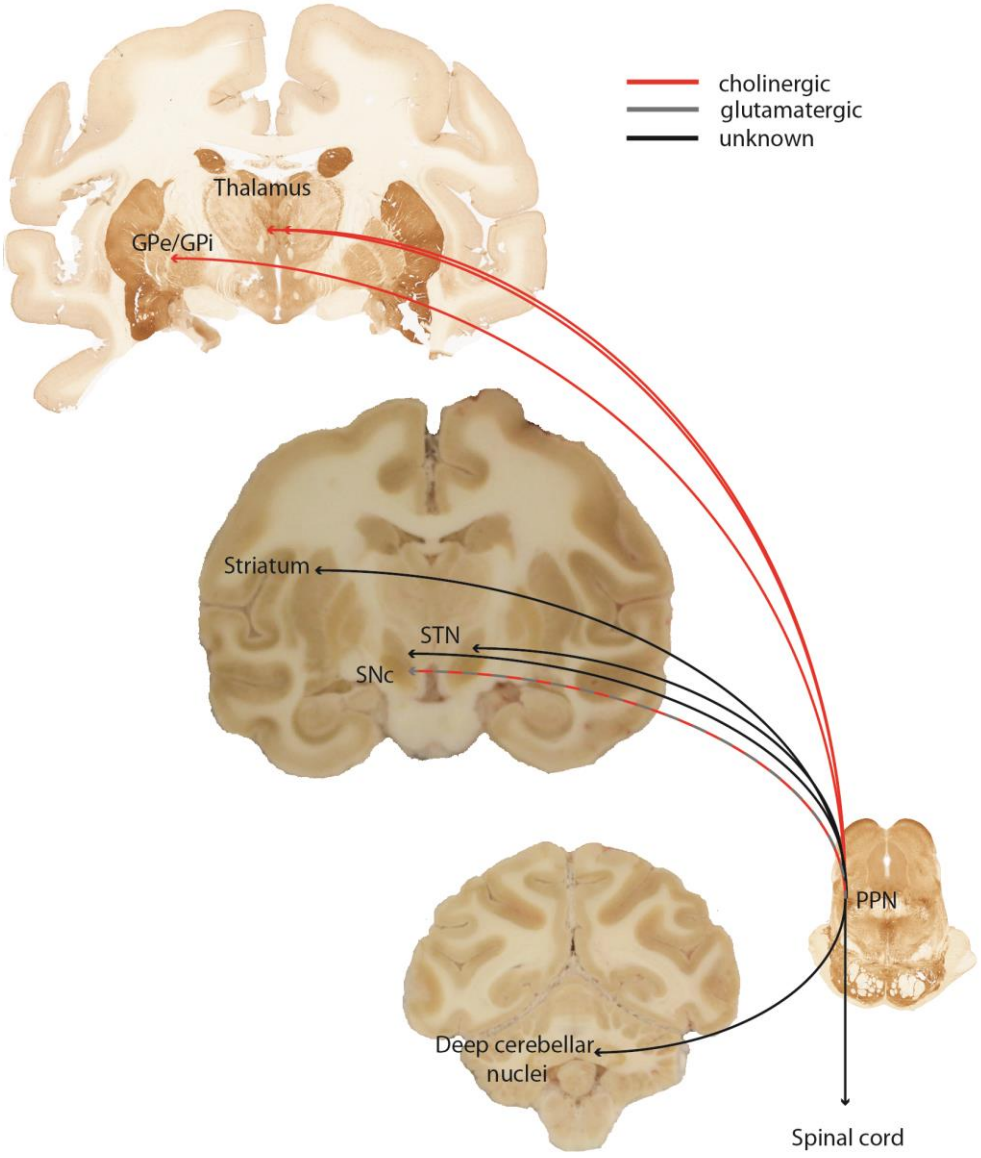

Figure 2. Efferent Connectivity of PPN.
PPN is highly connected to other structures in the brain. Those connections known in the NHP or human are shown here on coronal NHP brain slices. The color of the projection identifies the neurotransmitter if it is known (cholinergic in red and glutamatergic in grey).

1.3.3 Efferent Connectivity

PPN projects to many structures in the brain including those in the basal ganglia, thalamus, and cerebellum (Figure 2). Ascending, mostly cholinergic, projections from PPN innervate many nuclei of the thalamus, especially reticular nuclei and intralaminar nuclei such as the parafascicular nucleus and the central median nucleus (CM) [26], [38].

Bilateral projections to thalamus have been observed in humans via measured changes in regional cerebral blood flow in thalamus from positron emission tomography (PET) during unilateral PPN DBS [39]. Ascending projections also innervate many basal ganglia structures, including the GPi and globus pallidus external segment (GPe), STN, and SNc. Bilaterally, STN receives excitatory input from caudal PPN [40]. On the other hand, both cholinergic and glutamatergic PPN neurons are known to project to dopaminergic SNc neurons [41], with approximately 25% of cholinergic neurons in the PPN projecting to the SNc in the NHP [42]. A smaller number of PPN neurons, probably cholinergic, project to the globus pallidus (GP) via the ansa lenticularis and lenticular fasciculus [42]. There have been multiple studies documenting a projection from PPN to the striatum in the NHP as well [40], [43].

Descending projections innervate the deep cerebellar nuclei, reticular formation, locus ceruleus, raphe nuclei, and spinal cord, although most studies of descending projections have been done in only the rat and cat. Descending cholinergic neurons are thought to travel to the medullary reticular formation, which then projects to the spinal cord. There are also direct projections from the PPN to the cervical and thoracic spinal cord, which are thought to be mostly non-cholinergic [44], [45].

1.3.4 Afferent Connectivity

Due to its involvement in numerous functions, the PPN receives inputs from many different areas of the brain. Experiments in cats have revealed a substantial GABAergic input from the SNr [46]. These afferents originate in the lateral part of SNr and are thought to modulate postural muscle tone [47]. Afferents from medial SNr to the CN are thought to modulate locomotion [46]. Studies in NHPs have shown that these nigral pathways project to neurons in PPN and CN, while GABAergic pallidal pathways project only to PPN [48]. Similarly, pallidotegmental projections from caudal GPi terminate only on the non-cholinergic neurons of rostral PPN [49]–[51]. These pathways then project to the pontomedullary reticular formation. It has been hypothesized that the nigral-CN pathway controls axial posture while the pallidal-PPN pathway modulates locomotion [48]. However, it is still unknown whether these mechanisms hold true in the human

brain and what drives the SNr to control locomotion or posture. PPN also receives direct and indirect inputs, some glutamatergic, from the STN [48], [49], [52], [53]. Projections have also been found in PPN from the centromedian-parafascicular-subparafascicular complex region of thalamus [54]. Ventral striatum also sends GABAergic projections to the PPN in the NHP [40], [55], [56].

Afferents to PPN also originate in the cerebral cortex. In NHPs, functional neuroimaging and probabilistic diffusion tractography have suggested projections from motor cortex that display a somatotopic organization from medial to lateral with orofacial, forelimb, and hindlimb regions [57]. A strong functional connectivity between the supplementary motor cortex and medial and lateral PPN in both NHPs and humans has also been suggested based on neuroimaging data [58], [59]. This connection is thought to contribute to anticipatory postural adjustments and positively correlated with the severity of freezing in PD patients. A gait imagery fMRI study by Karachi et al. discovered two distinct networks between cortex and the MLR that are associated with gait [60]. The first connects the motor and premotor areas and the cerebellum with the CN and dorsal PPN and is involved in locomotion, whereas the second connects the posterior parietal and dorsolateral prefrontal cortex with ventral PPN and the integration of sensory information.

Reciprocal connections exist between the cerebellar output (fastigial nucleus) and PPN. The cerebellotegmental projection is excitatory, with fastigial fibers synapsing on the dendrites of PPN neurons [18]. This connection has also been shown in humans via probabilistic diffusion tractography [61]. This pathway is thought to send information about body position and postural responses during movement in the cerebellum to areas that control posture and gait in the brainstem and cortex. A probabilistic tractography study in humans showed that connectivity between PPN and the cerebellum is very important in preventing freezing of gait. Freezers showed no cerebellotegmental tracts, while healthy controls and PD patients without freezing of gait had intact connections [62]. Multiple other inputs to PPN have been discovered in lower order species, including inputs from cervical and lumbar segments of the spinal cord to cholinergic PPN neurons

and inputs from limbic areas, the reticular activating system, caudate, putamen, and the superior colliculus [4].

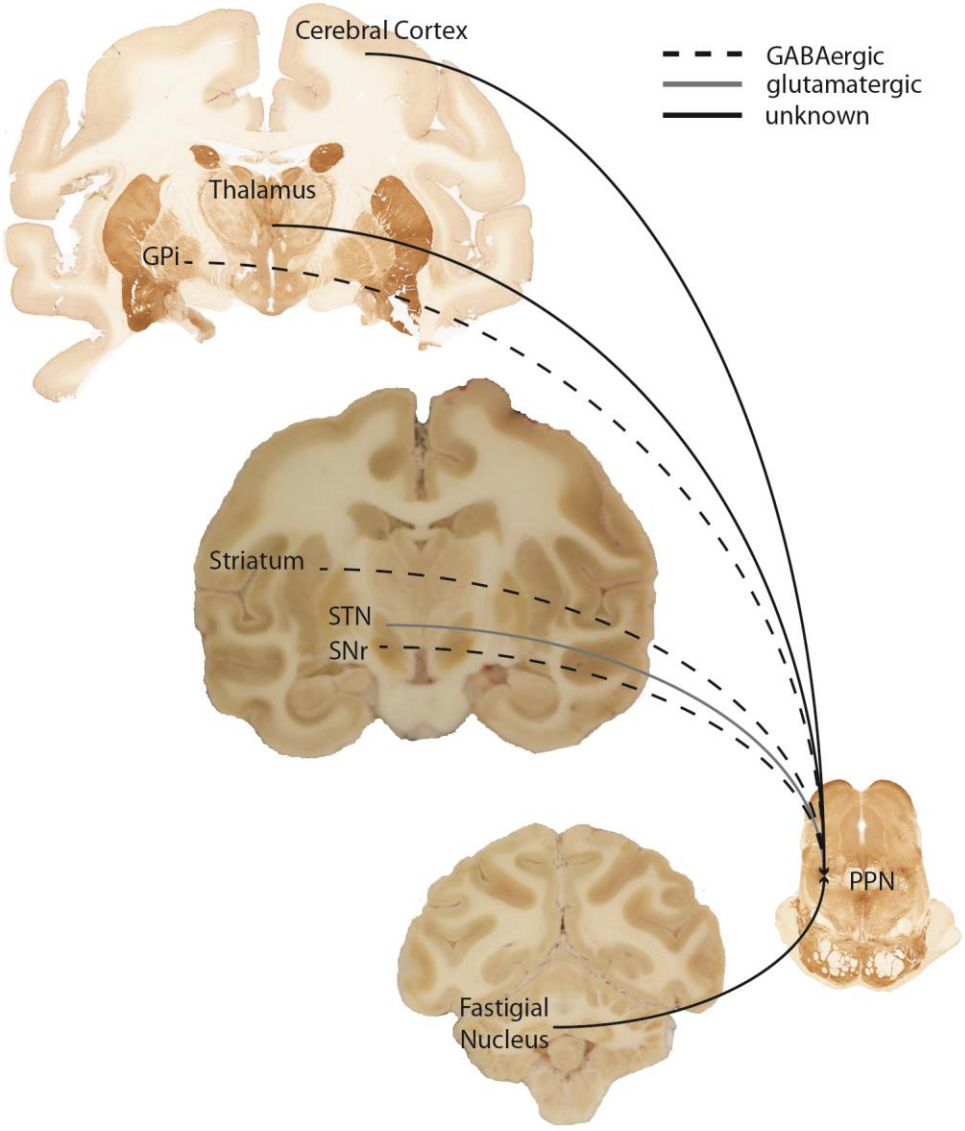

Figure 3. Afferent Connectivity of PPN.
PPN receives input from many structures in the brain due to its involvement in many different functions. The known connections in NHP or human are shown here on coronal NHP brain slices. The color of the projection identifies the neurotransmitter if it is known (dashed black line for GABAergic and grey line for glutamatergic).

1.3.5 Control of Locomotion

The connectivity of PPN exhibits its diverse functionality. One of the main functions of the PPN has been postulated to be involvement in gait after controlled locomotion was

induced by stimulating the PPN area in decerebrate animals [63], [64]. Extracellular recordings in the brainstem of decerebrate cats have also provided insight into the role of PPN in locomotion [65]. To date, three cell groups have been identified within the PPN based on their firing patterns related to gait. Two groups are described as 'non-bursting' neurons, probably subtypes of cholinergic type II neurons. The first group, 'on' cells, fire in a tonic pattern during locomotion but decrease firing rate or cease to fire when locomotion stops. The second group, 'off' cells, fire spontaneously in a tonic pattern but decreases their firing rate as locomotion speeds up and increases their firing rate just before locomotion ceases. These cells are thought to modulate the duration of locomotion. Due to the connections of cholinergic PPNc neurons with the spinal cord, thalamus and SNc, they may be relaying sensory information that is necessary to maintain gait [4]. The last group of cells, which are distributed widely in the region, are classified as 'bursters' and probably non-cholinergic type I neurons. These cells fire in a bursting pattern during locomotion and may play a role in modulating the frequency of stepping. They may also play a role in the initiation of gait programs due to the innervation of glutamatergic PPNd neurons by GPi and outputs to spinal cord [4].

A study was conducted in which PPN neurons were recorded in NHPs during a lever task. Based on this study, two types of cells were found to respond both prior to movement and throughout the upper extremity movement task [66]. One cell type increased its firing rate, whereas the other decreased its firing rate. Unlike studies in decerebrate cats, the groups were inseparable by spike width or firing rate classification. The change in firing rate so close to movement onset (and not cue presentation) implies the involvement of PPN in the initiation and execution phase of movement rather than the planning or preparation phase. This activity occurred for both contralateral and ipsilateral movements. Interestingly, intraoperative microelectrode recordings in humans prior to PPN DBS surgery revealed some neurons in the PPN area that also were responsive to contralateral limb movements [37]. Out of 103 neurons, 37 were responsive to either passive or voluntary movement. In 80% percent of the responsive cells, the response was excitatory. These responsive neurons were not characteristic of only one cell type, but of

all three, suggesting that both cholinergic and glutamatergic neurons may contribute to basal-ganglia motor control. Similar percentages of cells recorded superior (37%) and inferior (33 %) to PPN, as defined on 1.5 T MRI, were also responsive to movement suggesting motor control may not be limited to the PPN alone.

1.4 History of PPN area DBS

Based on its involvement in locomotion, the PPN is postulated to be a therapeutic DBS target for the gait and balance symptoms of PD that are not addressed by medication or traditional DBS targets. There have been many studies to evaluate the effectiveness of PPN DBS on axial motor signs of PD such as freezing of gait (FOG), postural instability (PI), and falls (Table 1). Typically, the motor signs of PD are measured using the Unified Parkinson's Disease Rating Scale (UPDRS) in which clinicians rate each motor sign on a scale ranging from 0 (not present) to 4 (severe) [67]. Additional measures of therapy include questionnaires regarding gait and falls or quality of life, reaction time tasks, or kinematic analysis. While some open label trials have shown improvement in small numbers of patients [68], [69], many other trials have seen only a reduction in falls [70], [71], caused side effects [72], [73], or had no effect [74].

One of the earliest open label trials by Plaha and Gill implanted two patients bilaterally in PPN to find that some high frequency stimulation (180-210 Hz) worsened gait and motor symptoms, stimulation between 30 and 175 Hz had differing effects on each patient, and stimulating at a frequency of 20-25 Hz improved both gait dysfunction and postural instability both on and off medication [69]. A double blind study by Moro et al. later implanted six subjects unilaterally in the PPN [75]. The study reported no difference in UPDRS III scores after 6 or 15 months, possibly a result of quite variable lead locations, but did report a significant reduction in falls in both the on and off medication state. Transient paresthesias, warm sensation, and oscillopsia were reported side effects for certain amplitude and frequencies. Another double blind study by Ferraye et al implanted six patients in PPN who developed persistent gait and freezing problems years after STN DBS [74]. After PPN DBS, there was no overall improvement seen in freezing, gait, or

postural instability measured with the UPDRS. Two patients on levodopa did have objective freezing improvements during a walking task, but other patients' freezing of gait worsened. Interestingly the best effects were seen in patients whose leads were implanted slightly posterior to the PPN, possibly in the subcuneiform and cuneiform region.

Multiple studies by Thevathasan et al. have shown that bilateral PPN DBS, specifically in the mid-lower and caudal PPN, is therapeutic based on the Gait and Falls questionnaire [70], [71] as well as a double blind study in which a turning task was employed [76]. These studies also implied that bilateral PPN stimulation may produce a better effect than unilateral PPN stimulation [71], [76]. Another study by Thevathasan et al. observed an improvement in reaction time during PPN stimulation [77]. Welter et al. evaluated the effects of bilateral PPN stimulation in four PD patients, utilizing multiple outcome measurements [73]. This included a clinical evaluation using the Rating Scale for Gait Evaluation (RSGE) and UPDRS, cognitive and psychiatric tests, and a recorded gait initiation walking test on a force platform. While this randomized double blind study showed no significant differences in the RSGE score, some complex effects of PPN DBS did emerge. This included a significant improvement in FOG, an improved quality of life, modification of anticipatory postural adjustments and decrease in double-stance duration. This study concluded that traditional clinical tests were unable to detect subtle changes of PPN DBS.

A larger study by Mazzone et al. implanted 24 PD and 4 progressive supranuclear palsy (PSP) patients, most unilaterally, in the PPN [78]. Despite differing lead locations in relation to PPN, clinical evaluations revealed a significant group decrease in UPDRS III scores, subitems 27-30 scores and Hoehn and Yahr disability scale scores after one year of stimulation. The only side effects reported were paresthesias, which disappeared over time. All patients required a bipolar stimulation setting for therapy at frequencies of 25 or 40 Hz. Based on their findings and the differing lead locations of their patients, they argued that there may not be one single location within PPN that provides therapy.

Study	#	Target, Stimulation Frequency	Lead	Study Design	Effects on FOG, PI, Falls	Side Effects	Follow-up
Mazzone et al 2013 [78]	24 PD, 4 PSP	6 bilateral PPN, 21 unilateral PPN (25 Hz, 40 Hz)	3389	Open Label	Significant reduction in UPDRS III, HY scores	Transient paresthesias, intraoperative bleeding in GPi (1), one patient not implanted	3.8 ± 1.5 years
Thevathasan et al 2010 [77]	11 PD	10 bilateral PPN, 1 unilateral PPN (20-35 Hz) (3 had ZI DBS that was turned off for study)	3387	Single Blind	Improvement in speed of reaction, acutely improved UPDRS 27-30, chronically improved falls	Transient paresthesias	2-38 months
Thevathasan et al 2012 [71]	7 PD	5 bilateral PPN (20-40 Hz), 2 unilateral PPN (30-35 Hz)	6 3389, 1 3387	Open Label	Improvement in Gait and Falls questionnaire (10.5-58.3%)	None reported	10-13 months
Moro et al 2010 [75]	6 PD	Unilateral PPN (50 Hz, 70 Hz)	3387	Double Blind	No significant effects on FOG or PI, but significant reduction in falls.	Contralateral paresthesias, warm sensation, unilateral oscillopsia	3 & 12 months
Thevathasan et al 2011 [70]	5 PD	Bilateral mid-lower PPN (35 Hz)	3387	Open Label	Significant improvement based on Gait and Falls questionnaire.	Voltage-dependent oscillopsia	6 months & 2 years
Welter et al 2015 [73]	4 PD	Bilateral PPN area (20,40 Hz)	3389	Double Blind	Significantly improved anticipatory postural adjustments, double-stance duration, and quality of life.	Voltage-dependent paresthesias, oscillopsia. 2/6 patients didn't complete study due to Infection (1) and midbrain hematoma (1)	4 & 6 months
Plaha and Gill 2005 [69]	2 PD	Bilateral PPN (20,25Hz)	3389	Open Label	Improvement in FOG, PI, Falls, and UPDRS II score both on/off medication	Worsened gait and motor at certain frequencies	A few days
Wilcox et al 2010 [79]	1 PPFG	Bilateral PPN (35 Hz)	3387	Open label	Significant improvement in FOG, PI, falls	Feelings of unsteadiness, physical exhaustion (DBS off)	14 months

Table 1. Summary of selected studies displaying the results of PD patients implanted in the PPN area. *PPFG: primary progressive freezing of gait*, *PSP: Parasupranuclear palsy*

PPN DBS in combination with another DBS target may further improve the overall therapeutic outcomes for PD patients (Table 2). Schrader et al. implanted one patient bilaterally in both the PPN and GPi, showing that PPN DBS mildly improved gait initiation and freezing of gait, but combined DBS of PPN and GPi had a larger, albeit still modest, improvement [68]. Similarly, Stefani et al. implanted six patients in PPN and STN [72]. While PPN DBS was effective for gait and posture, significant improvement was seen in the ON medication state during combined STN and PPN DBS compared to individual target stimulation ON medication. Peppe et al. also implanted patients bilaterally in both the PPN and STN, using gait kinematics to evaluate the effects of stimulation [80]. No significant changes were seen in the ON medication state, only in the OFF medication state. This included significant increases in mean gait velocity during STN DBS and combined STN and PPN DBS when compared to OFF DBS. The kinematic variable of joint angle displacement during the stance and swing stride phases was compared to control subjects. While the kinematics of some joints improved during PPN DBS alone, STN DBS and combined STN and PPN DBS were more effective. However, no stimulation settings provided any additional benefit to medication. Mazzone et al. implanted 12 PD and 2 PSP patients in the PPN, where six were also implanted in a basal ganglia target, either the GPi or STN. While improvements in gait, posture, and speech were observed, simultaneous stimulation of both the PPN and either GPi or STN was found to be more effective at treatment of motor symptoms and reducing medication [81]. Further studies are needed to discern whether dual implants in a basal ganglia target and in PPN are necessary for treating gait and balance symptoms in PD.

Combined stimulation of PPN with other targets such as the zona incerta (ZI) has been tested as well. Khan et al. implanted four patients bilaterally in the caudal ZI and PPN to test the effects of single or multiple target stimulation [82]. While combined stimulation of PPN and ZI produced the greatest improvement in UPDRS-III scores, the results of a PET analysis are the most intriguing. Combined stimulation displayed an additive effect on regional cerebral blood flow changes to that seen in individual target stimulation. This included areas of the basal ganglia, thalamus, cerebellum, and sensorimotor cortical

areas. Another case study in which a patient with primary progressive freezing of gait (PPFG) symptoms is implanted bilaterally in the PPN displayed improvement in gait and posture was further analyzed with fluorine-18-deoxy-D-glucose (F-18FDG) PET [79]. This study identified abnormal hypoactive regions in the cerebellum and brainstem where FDG uptake was normalized during PPN stimulation.

Study	#	Target, Stimulation Frequency	Lead	Study Design	Effects on FOG, PI, Falls	Side Effects	Follow-up
Mazzone et al 2009 [81]	12 PD, 2 PSP	5 bilateral PPN+STN, 1 bilateral PPN, 6 unilateral PPN, 1 unilateral PPN+GPi (all 25 Hz)	3389	Open Label	Greatest improvement in UPDRS III (18, 27-30) with multiple targets	Transient paresthesias, cortical arousal response, grammar processing improvement	1-24 months
Ferraye et al 2010 [74]	6 PD	Bilateral PPN area (15-25 Hz) + STN (previously implanted)	3389	Double Blind	Variable results, but no significant changes	Seizures (1), frequency dependent oscillopsia, paresthesias, limb myoclonus, lead placement on average 2 mm anterior to PPN	4-6 & 12 months
Stefani et al 2007 [72]	6 PD	Bilateral PPN (25 Hz) + STN (130-185 Hz)	3389	Open Label	PPN + STN improved axial symptoms more than PPN alone	Paresthesias, lead placement possibly in nucleus peripeduncularis	3 & 6 months
Peppe et al 2010 [80]	5 PD	Bilateral PPN (25 Hz) + STN (185 Hz)	3389	Open Label	In OFF levodopa state only, STN and combined STN-PPN DBS improved joint angle kinematics and mean gait velocity	None reported	1 year
Khan et al 2012 [82]	4 PD	Bilateral PPN (60 Hz, 1 patient at 25 Hz) + ZI (60 Hz)	3389	Open Label	Greatest improvement in UPDRS-III scores during PPN+ZI stimulation	None reported	3-44 months
Schrader et al 2013 [68]	1 PD	Bilateral PPN (25 Hz) and GPi (130 Hz)	3387 GPi, 3389 PPN	Single blind	Moderate effects on gait initiation and FOG	Voltage-dependent warm facial sensation, phosphenes	4 weeks

Table 2. Summary of selected studies displaying the results of PD patients implanted in multiple targets.

Some PPN DBS studies have found that lower stimulation frequencies (<30 Hz) provided more therapeutic benefit than the higher frequencies (> 80 Hz) used for traditional DBS targets [83]. However, the results are complicated, as stimulation at frequencies between 80 and 130 Hz have resulted in a variety of patient-specific outcomes, including therapy [69], worsening [69], or no effect [75], [83]. Only one study has systematically investigated the effects of different frequencies (2 to 185 Hz) in six patients [75]. The results show that a frequency between 50 and 70 Hz produced better motor scores in an open label study at 2 months; however, no significant improvement was seen in the double blind study at 3 and 12 months. Even so, most studies have used a stimulation frequency around 25 Hz to investigate the effects of PPN DBS. The positive results associated with low frequency stimulation in the PPN may be due to a lower intrinsic firing rate of PPN when compared to STN and GPi. The firing rate in PPN was reportedly around 14-25 Hz in PD patients [37], [83]–[85]and 18-20 Hz in parkinsonian rats [86].

1.5 Challenges of PPN DBS

The exact reasoning behind the mixed clinical trial results is unknown; however, it may be due to factors such as patient selection, DBS lead designs, lead location, uncertainty regarding the most therapeutic stimulation site, stimulation settings, or the methods of gait analysis. Patient selection is a challenge of PPN DBS, as the proper symptoms for this type of stimulation are unknown other than obvious gait and balance difficulties. The level at which these symptoms are responsive to dopaminergic drugs is another unidentified criteria. It has been suggested that a younger patient population may improve PPN DBS outcomes, perhaps due to a lower level of degeneration of cholinergic neurons in PPN [78]. Unfortunately, this may be similar to other treatments such as STN and GPi DBS whose therapies concerning gait and balance have been shown to decrease over time [87], [88]. Whether this is due to disease progression or habituation to stimulation, care should be taken when evaluating therapy to compare ON- and OFF-DBS conditions during the same time period.

The relationship between the size of the nuclei in the region and the diameter of the DBS lead is another issue, as the lead may be forming a large lesion when it is implanted. Also, the DBS lead used in the clinic has four cylindrical contacts for stimulation. These contacts each have a length of 1.5 cm with either 0.5 mm or 1.5 mm spacing. The size of these contacts in relation to the small size of PPN in humans makes it exceedingly difficult to selectively stimulate a brainstem region. As shown in Chapter 2, DBS leads with smaller, segmented electrodes may allow for more therapeutic stimulation through current steering.

Furthermore, optimal lead location is difficult to execute due to the depth of the target area, challenges with verification of lead location due to the low resolution of clinical MRI, and lack of contrast differences in PPN on MRI due to its ambiguous borders. In clinical trials, there has been no consistent verification of accurate lead placement. In fact, post implantation MRI showing lead placement displays highly inconsistent results [75], [72]. In addition to MRI, other targeting methods include intraoperative microelectrode recordings to target PPN using electrophysiological markers. While some cells within the PPN region are thought to have distinctive firing patterns, as mentioned above, others have reported that most of the neurons (57%) fire randomly [37].The lack of defined borders is another challenge [81], [89]. Another intraoperative targeting method is based on somatosensory evoked potentials, which allows for a rough calculation of the distance between the lead and the obex. This method only allows for determination of the z direction (depth) of the lead to ensure it has reached the pons [90]. However, based on a study of a large number of subjects with varying lead locations and therapeutic results, it has been suggested that lead location within PPN is not as important as previously thought [78]. This is controversial given the open label approach to this study and the utilization of low-field MRI to identify lead locations and PPN region morphologies. The study also implies that therapeutic stimulation may not be stimulating the remaining cholinergic cells of PPN, but rather passing fibers in the region. This last point reiterates the uncertainty in the optimal therapeutic stimulation site. The complexity and lack of understanding of the functionality of the nuclei in this region as well as the

vast array of fiber pathways make it difficult to determine the modulatory effects of stimulating different structures. ***Through this dissertation, I hypothesized and subsequently demonstrated that activation of pathways in the PPN area and the resultant therapy is in fact highly sensitive to lead location and stimulation parameters.***

The results of clinical trials have only increased the known complexity of stimulation in this region due to the mixed therapeutic results and vast array of side effects reported. Side effects have included urinary incontinence [91], oscillopsia [75], [70], [92], and frequency and intensity dependent paresthesias [69], [75], [74]. Other effects of PPN DBS have included a frequency dependent increase in rapid eye movement (REM) sleep or an increase in alertness [93]–[95]. Renal function has also been influenced in PPTg stimulation in mice [96], [97]. It is difficult to compare these side effects and therapy across studies though because of the lack of reporting of specific lead locations, the fact that most studies are open label, differing stimulation settings, and the inadequate measurement and reporting of results.

Finally, one of the largest challenges in stimulating for gait symptoms is quantifying the effects of therapy. Gait and balance problems are multifaceted and sometimes only intermittently visible. This makes it difficult to detect subtle changes from stimulation in a reliable manner, as current clinical tests such as the UPDRS seem inadequate and kinematic analysis of gait is complex and time consuming. Further, clinical trials conducted with a better understanding of the pathways modulated by PPN-DBS therapy and a prospective approach to targeting these pathways is necessary to treat gait and postural control disturbances in Parkinson's disease on a patient-specific basis. The following chapters of this thesis describe efforts to develop translational computational and imaging-based approaches to address these challenges.

Chapter 2 describes the development of computational models to determine the effects of DBS on PPN neurons and surrounding fiber pathways. This study compared atlas-based models in both the NHP and human and briefly explored the use of a segmented electrode as an alternative to the clinically available 4-contact DBS lead. These models could

ideally be used to predict optimal stimulation settings and lead locations. In order for these models to be clinically relevant, subject-specific models must be developed due to the slight variations in anatomy between patients. Chapter 3 details the development of high-field MRI tools to visualize the structures in the brainstem. These tools enable subject-specific computational models and could also assist with DBS lead trajectory planning. Finally, Chapter 4 describes the development of a subject-specific computational model in an NHP. This study necessitated the need for incorporating anisotropic conductivity into the brain tissue in the models and used the presence of side effects to validate the fiber pathway models.

2 Atlas-based PPN DBS Models

This chapter reprinted with permission from IOP Publishing.

Laura M. Zitella, Kevin Mohsenian, Mrinal Pahwa, Cory Gloeckner, and Matthew D. Johnson, "Computational modeling of pedunculopontine nucleus deep brain stimulation," *J Neural Eng*, 10.4 (2013): p. 045005.

2.1 Overview

2.1.1 Objective

Deep brain stimulation (DBS) near the pedunculopontine nucleus (PPN) has been posited to improve medication-intractable gait and balance problems in patients with Parkinson's disease. However, clinical studies evaluating this DBS target have not demonstrated consistent therapeutic effects, with several studies reporting the emergence of paresthesia and oculomotor side effects. The spatial and pathway-specific extent to which brainstem regions are modulated during PPN-DBS is not well understood.

2.1.2 Approach

Here, we describe two computational models that estimate the direct effects of DBS in the PPN region for human and translational non-human primate (NHP) studies. The three-dimensional models were constructed from segmented histological images from each species, multi-compartment neuron models, and inhomogeneous finite element models of the voltage distribution in the brainstem during DBS.

2.1.3 Main Results

The computational models predicted that: 1) the majority of PPN neurons are activated with −3V monopolar cathodic stimulation; 2) surgical targeting errors of as little as 1 mm in both species decrement activation selectivity; 3) specifically, monopolar stimulation in caudal, medial, or anterior PPN activates a significant proportion of the superior cerebellar peduncle (up to 60% in the human model and 90% in the NHP model at -3V); 4) monopolar stimulation in rostral, lateral, or anterior PPN activates a large percentage of medial lemniscus fibers (up to 33% in the human model and 40% in the NHP model at

−3V); and, 5) the current clinical cylindrical electrode design is suboptimal for isolating the modulatory effects to PPN neurons.

2.1.4 Significance

We show that a DBS lead design with radially-segmented electrodes may yield improved functional outcome for PPN-DBS.

2.2 Background

Deep brain stimulation (DBS) within the mesencephalic locomotor region (MLR) of brainstem, which includes the pedunculopontine nucleus (PPN), has been shown to alleviate akinesia and gait disturbances in parkinsonian NHPs [4], [98]. However, DBS within this anatomical substrate in humans has produced inconsistent therapeutic results. Clinical outcomes have ranged from positive effects on most parkinsonian motor signs [69], [72], [83], positive effects only on gait and likelihood of falling [75], [79], or little to no consistent therapeutic benefit [74] . Several factors that may have contributed to such variability include incomplete activation of neuronal pathways within the PPN and modulation of fibers passing near the PPN that have confounding effects on parkinsonian motor signs when activated. Inconsistent results between experimental and clinical DBS studies may also have occurred because PPN morphologies are different between the human and NHP. A method for predicting how implantation trajectory, lead position, and stimulation settings affect neuronal pathways in and around the PPN and how these results differ between NHP models and humans will help to clarify previous clinical findings and inform future research.

The anatomical target underlying the observed therapeutic effects of DBS on parkinsonian gait has largely been posited from correlation analysis of electrode position and clinical outcome, inferring that the brain regions immediately adjacent to the active electrode(s) represent the primary regions that are modulated by DBS [69], [75], [74], [79], [72], [83]. There are two primary challenges with this indirect approach. First, there is a need to develop imaging sequences with enough contrast [99], [100] and physiological markers with enough consistency [37], [90] to define the amorphous

boundaries of the PPN [101]. Second, the approach provides an imprecise estimate of the volume of tissue modulated by DBS and lacks the capacity to quantify the subtle changes in neurophysiology that can occur when adjusting stimulation amplitudes, frequencies, and pulse widths. Experimental DBS studies in NHPs have demonstrated that small deviations in stimulation parameters can result in significantly different firing patterns and rates in neuronal populations downstream of the DBS target [102], [103]. Together, the uncertainty in position and volumetric effects of DBS have led to several controversies over putative targets for therapy [72], [104], [105] and mechanisms of side effects [92], [106] with PPN-DBS.

When considering the mechanisms of DBS, several studies have noted that fiber pathways can play an important role in accurately interpreting therapeutic outcomes [107]–[110] . There are several fiber pathways adjacent to PPN, which given their proximity may be unwantedly modulated during PPN-DBS. The superior cerebellar peduncle (SCP), also known as the brachium conjunctivum, runs medially around the PPN with axons stemming from cell bodies in the contralateral dentate nucleus and interposed nucleus of the cerebellum [111], [112]. SCP fibers are known to carry information to the motor cortex through the red nucleus and thalamus near the fourth ventricle [113]. When the SCP is lesioned at the level of the PPN (i.e. rostral to the decussation), motor coordination deficits can result contralateral to the side of the lesion [114], [115]. Additionally, the medial lemniscus (ML), whose axons arise from cell bodies in the cuneate and gracile nuclei, is a fiber pathway that runs lateral to PPN [113]. Stimulation of the ML is thought to induce sensory paresthesias [37], [74], [116]. There are several other fiber pathways that project near the PPN, including the lateral lemniscus (LL) carrying auditory signals from the cochlear nuclei to the inferior colliculus [113], the central tegmental tract carrying limbic and oculomotor information from the ipsilateral red nucleus to the ipsilateral inferior olivary nucleus [21], [117], and the anterior spinocerebellar tract carrying proprioceptive information to the cerebellum from the posterior grey column of the ipsilateral and contralateral sides of the body to the cerebellum rostral to the trigeminal nerve [113]. Given the close proximity of these fiber

pathways to MLR nuclei, it is important to put activation of MLR nuclei in the context of potential activation of these fibers.

In this study, we have developed a computational modeling framework that includes anatomically and biophysically-realistic models of two classes of PPN neurons as well as SCP, ML, and LL fiber pathways. The models provided a unique opportunity to investigate three questions: (1) What pathways are activated when performing a monopolar review across all four DBS electrodes? (2) How sensitive are these results to location of the DBS lead within the MLR? (3) Can a lead design with segmented electrodes enable more selective modulation of the PPN in cases of misaligned DBS leads?

2.3 Methods

2.3.1 Anatomical surface reconstructions

Three-dimensional surface reconstructions of the PPN, ML, LL, and SCP borders were segmented from coronal plates in a NHP brain atlas [118] (Figure 4a) and from pseudo-horizontal plates in a human brain atlas [16] (Figure 4b). The reconstructions were created by tracing the anatomical boundary of each nucleus or fiber tract across multiple plates (0.45 mm and 0.5 mm spacing between plates for the NHP and human atlas, respectively) and lofting the 2D contours into 3D surfaces using a non-uniform rational B-spline imaging method (Rhinoceros, Seattle, WA).

2.3.2 Deep brain stimulation lead position

The DBS lead was introduced into the anatomical model along an oblique trajectory. In the NHP model, the lead was placed parallel to the fourth ventricle with an angle of 8° along the coronal plane and 25° along the sagittal plane such that the most distal electrode resided at or slightly below the caudal border of PPN (Figure 4a,b). A similar trajectory paralleling the fourth ventricle was used in the human model, adjusting slightly for the altered anatomy of the PPN, with a lead angle of 14° along the coronal plane and 25° along the sagittal plane [100]. These trajectories were similar to the trajectory described by Mazzone et al. [116], who used 25° along the sagittal plane and 11-18°

along the coronal plane, and Ferraye et al. [74] whose planned trajectory was parallel to the floor of the fourth ventricle.

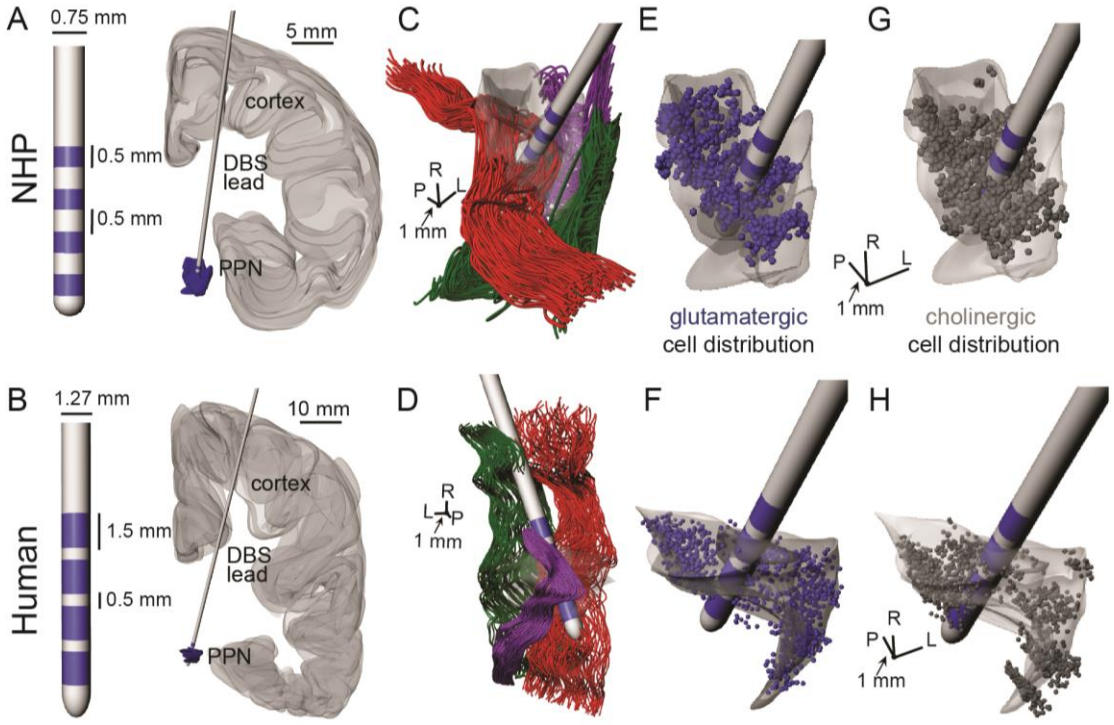

Figure 4. Anatomical framework for modeling PPN-DBS in NHPs and humans.
Spatial dimensions are given for the (a) NHP and (b) human DBS lead and implantation trajectory. (c, d) Modeled fiber pathways that surround the PPN include the SCP (red), ML (dark green) and LL (purple). Orientation in the human model is different from other figures to provide better view of all fiber tracts. (e, f) Histological reconstructions from Lavoie and Parent [26] showing locations of labeled glutamatergic cells (type I). (g, h) The equivalent cholinergic cell distribution (type II) from the same histological studies. L: lateral; R: rostral; P: posterior.

Three electrode geometries were investigated including a clinical DBS lead for the human model, a scaled-down clinical DBS lead for the NHP model [119], and a radially-segmented DBS lead for the human model [120], [121]. A Medtronic 3387 lead (4 electrodes; 1.27 mm diameter; 1.5 mm height; 0.5 mm electrode spacing) was incorporated in the human model and a scaled-down version of the same lead (4 electrodes; 0.75 mm diameter; 0.5 mm height; 0.5 mm electrode spacing) was added to the NHP model. The radially-segmented DBS lead was designed to have greater than eight times the resolution of the standard human electrode. This design consisted of 16

rows, each containing four evenly distributed circular electrodes (0.7 mm diameter; 0.067 mm between rows).

2.3.3 Lemniscus and cerebellar peduncle axon models

Axonal tract morphologies were generated from histological contour reconstructions of ML, LL, and SCP. Each contour was randomly seeded with 400 points using a 'Jordan Curve' algorithm, and each point in a given contour was connected with its 'nearest neighbor' point in an adjacent contour. Spline fits were then applied to the resulting sets of connected points across contours to generate three-dimensional traces for each axon in the population (Figure 4c, d). In the NHP, the SCP tract coursed through the medial-caudal portion of PPN. Fibers that overlapped with the lead were removed from the model before simulation. In the NHP, LL and ML axons coursed along the lateral and anterior side of PPN, respectively, but did not overlap with any portion of the DBS lead. In the human model, no fibers coursed through PPN with ML coursing anteriorly, LL laterally, and SCP medially to PPN. None of the fibers in the human model overlapped with the DBS lead.

Axonal membrane dynamics were applied to each fiber and were consistent with previous studies [107]–[109], [122], [123]. The 2 μm diameter myelinated axon model consisted of NODE (nodes of Ranvier), MYSA (myelin attachment segments), FLUT (paranode main segments), and STIN (internode segments) compartments connected to each other through an axial resistance. The nodes were modeled with fast Na+ channels, persistent Na+ channels, slow K+ channels, and a leakage current responsible for nodal action potential. The paranode segments contained fast K+ currents.

2.3.4 Pedunculopontine nucleus neuron distributions

The three-dimensional surfaces provided a boundary to populate reconstructions of PPN neurons including their axonal projections (Figure 4e-h). Two primary types of neurons within PPN, cholinergic and glutamatergic, were populated within PPN according to a previous histological study [26]. It should be noted that approximately 40% of cells in PPN are known to co-label for glutamate and acetylcholine, indicating that certain cells in

the PPN may have dual effects on their downstream targets [42]. These co-labeled cell types were not explicitly modeled in our study.

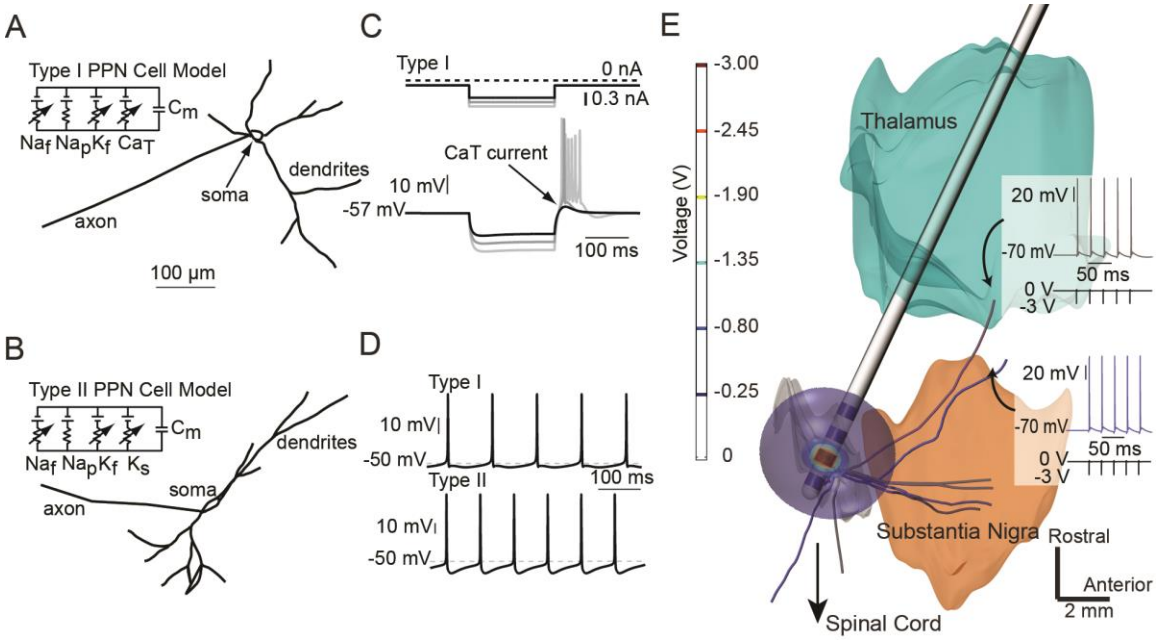

Figure 5. PPN cell model development and coupling with finite element analysis.
(a–d) PPN cell morphologies and biophysical responses. (e) PPN neuron models (type I in grey, type II in blue) in the context of both DBS finite element analysis and model responses to a −3 V cathodic stimulation pulse train.

Type I neurons are considered non-cholinergic, while the majority of type II neurons are immunopositive for ChAT (choline acetyltransferase) (71%) [36]. This distinguishing classifier was used to position the somas of each type of neuron in the PPN according to a previous histological study in NHPs [26]. Specifically, eight 40 µm thick slices were used to localize NADPH-diaphoraselabeled neurons (type I) and ChAT positive neurons (type II) within the PPN. Each position was extracted into our model and the slices were placed to match the constraints of PPN borders based on the brain atlas reconstructions. Soma positions for each cell type were distributed randomly in depth between slices. There was a generally consistent overlap between the brain atlas surface reconstructions of PPN and the borders of PPN defined by soma positions in the NHP histology.

PPN type I and type II neurons were reconstructed from camera lucida drawings [36] in Rhinoceros and were positioned in the PPN reconstruction such that the soma positions were consistent with the soma labeling distribution [26]. Axonal efferents were oriented to project to atlas-based segmentations of thalamus, substantia nigra, brainstem, or spinal cord. A total of 1139 type I neurons and 1154 type II neurons were distributed within the context of the surface reconstruction of PPN. Other projections to the subthalamic nucleus (STN), globus pallidus internus (GPi), cerebral cortex, and striatum were not explicitly modeled, but could be inferred from the activation patterns identified in the modeled axonal projections stemming from PPN.

2.3.5 Pedunculopontine nucleus neuron morphologies

The two PPN neuron types were modeled in a multi-compartment framework in NEURON v7.2 [124] with morphologies and electrophysiological characteristics consistent with previous studies [26], [36], [42], [42], [125]. Type I neurons consisted of an elongated cell body (31 μm long-axis, 13 μm short-axis, 20 μm thickness) with four primary dendrites (100-600 μm in length) and four axonal processes branching to the SNr, thalamus, and spinal cord [41], [42] (Figure 5a). Type II neurons consisted of a larger polymorphic cell body (50 μm long-axis, 24 μm short-axis, 20 μm thickness) with four primary dendrites (250-600 μm in length) and with four primary axonal processes projecting to the SNr, thalamus, and brainstem [41], [42] (Figure 5b). Cells were oriented such that their axonal processes extended to their efferent targets (Figure 5e). If a cell passed through the DBS lead or its encapsulation layer, that cell was labeled as damaged and deleted from the model. In the NHP model, this amounted to 456 type I (40%) and 537 type II (47%) cells labeled as damaged. Similarly, in the human model, 258 type I (23%) and 456 type II (40%) cells were considered damaged.

Current	**Description**	g_{ion} **(S/cm^2)**	
		Type I	*Type II*
Na_F	Fast-acting sodium current	0.008	0.007
Na_P	Persistent sodium current	0.00001	0.00001
K_{DR}	Delayed rectifier potassium current	0.004	0.004
K_A	A-type potassium current	--	0.001
Ca_T	Low-threshold calcium current	0.0004	--

Table 3. Active channel properties.

2.3.6 Pedunculopontine nucleus neuron membrane properties

Type I neurons, which have been characterized by low-threshold Ca2+ spikes without a transient outward current, were modeled with ion channels that generated an average firing rate of 10 Hz (Figure 5c,d) [125], [126]. Ionic currents in the soma and dendritic compartments of these type I neurons were defined according to the summation (Figure 5a):

$$I_{ion} = I_{Na_f} + I_{Na_p} + I_{K_{DR}} + I_{Ca_T} \quad (1)$$

where each channel's current was written in the form of $I_{ion} = \mathrm{g_{ion}}\eta(v - E_{ion})$ such that the maximum conductance $\mathrm{g_{ion}}$ was multiplied by one or more gating variables (η) that ranged from 0 to 1 (detailed in Table 3).

$$\dot{\eta} = \alpha_\eta(1 - \eta) - \beta_\eta = (\eta_\infty - \eta)/\tau_\eta \quad (2)$$

$$\eta_\infty = \alpha_\eta/(\alpha_\eta + \beta_\eta) \qquad \tau_\eta = 1/(\alpha_\eta + \beta_\eta) \quad (3)$$

Type II neurons, which have been characterized by a transient outward A-current without low-threshold Ca^{2+} spiking activity, were modeled with membrane properties consistent with [36], [125] (Figure 5d). While a heterogeneous collection of cholinergic and non-cholinergic type II cells have been identified in rodents, for the purposes of this study, we modeled only type IIa cells [36], [125]. Dynamics of this cell type includes long-duration action potentials (2.3 ms), low-input resistance (123 Ω), a regular firing pattern, and a lower firing rate (8.5 Hz) exhibiting accommodation with depolarizing somatic current injection [125]. Ionic currents in the soma and dendritic compartments of these type II neurons were defined according to the summation (Figure 5b):

$$I_{ion} = I_{Na_f} + I_{Na_p} + I_{K_A} + I_{K_{DR}} \quad (4)$$

The axonal processes for both type I and type II neurons were modeled as a myelinated, double-cable structure that included nodes of Ranvier (diameter, 1.4 μm), paranodal (1.4 μm) and internodal (1.6 μm) segments, and a myelin sheath (outer diameter, 2.0 μm) [107], [109], [122], [123]. PPN model neurons were not instantiated with synaptic

dynamics from axonal afferents given that the distribution, morphology, and type are yet to be established for each cell type. Previous computational modeling studies have indicated that the lowest threshold for generating action potentials using pulse widths at clinical DBS settings (60 - 240 μs) are located in the axonal processes as opposed to cell bodies [127]. This process of eliciting action potentials within the axons will be referred to as 'activation' in the results to follow, and the stimulation amplitude threshold to elicit action potentials after >80% of the stimulus pulses will be defined as the 'threshold voltage'.

2.3.7 Finite element modeling of deep brain stimulation

For all DBS lead types, a three-dimensional finite-element model (FEM) of neural tissue was developed around the DBS lead using COMSOL Multiphysics v4.0 (COMSOL, Burlington, MA). The FEM mesh consisted of tetrahedral elements within a 50 mm radius by 80 mm height cylindrical surface with the outside boundary set as the return pathway to ground. Electrical properties of neural tissue were defined as homogenous and isotropic (0.3 S/m), except for a 0.25-mm thick layer of encapsulation tissue at the electrode surface (0.18 S/m) [128]. The voltage distribution in the tissue was calculated with a frontal solution method of the Laplace equation, via the stationary MUMPS solver in COMSOL.

The applied stimulus pulse train was based on experimentally recorded waveforms produced by a voltage-controlled implantable pulse generator (Medtronic, Minneapolis, MN). The stimulus waveform consisted of a charge-balanced 90 μs cathodic phase followed by a 3 ms anodic phase repeated at a frequency of 30 Hz, which is consistent with previous clinical studies of PPN-DBS [74], [72]. The waveform was scaled such that the peak cathodic amplitude at a particular neuron compartment corresponded to the spatial voltage value from the FEM simulations. The waveform was then filtered by a Fourier FEM simulation to incorporate the capacitive properties of the electrode-tissue interface [129].

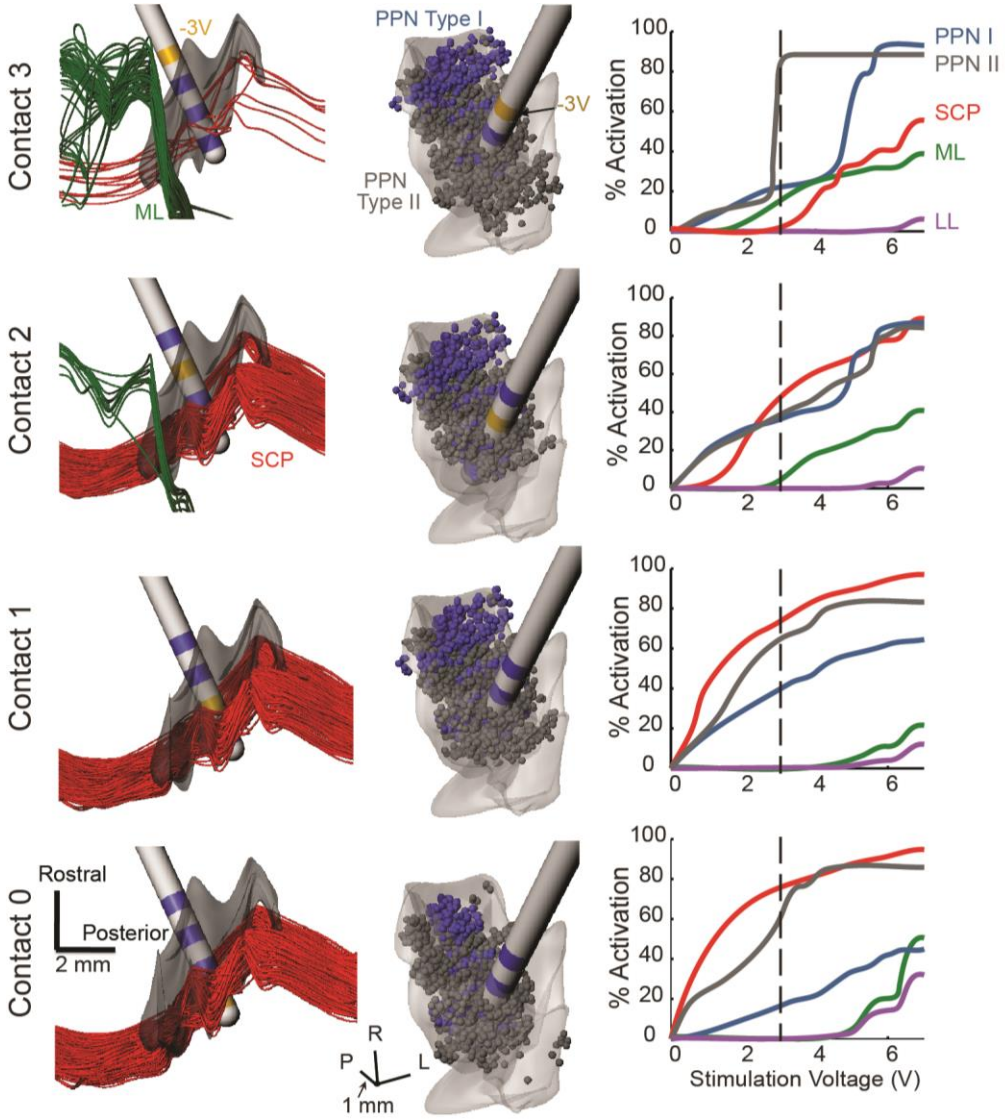

Figure 6. Prediction of neuronal elements activated at -3 V cathodic stimulation in NHPs.
Each monopolar DBS setting is modeled using the clinical lead trajectory. Shown are the fibers of passage (pipes) and PPN soma positions (spheres) activated at -3 V cathodic stimulation for all four electrode contacts. Inactivated fibers and cells are not shown. In some cases, activated fibers and cells obscure the active contact, which is depicted in yellow. Additionally, activation profiles are shown for all fibers and PPN cell types for each monopolar DBS setting over a range of stimulation voltages. The dotted vertical line represents the setting depicted on the left.

2.4 Results

2.4.1 Fiber pathways modulated during PPN-DBS

Computational model predictions of monopolar cathodic stimulation through each of the four electrodes were evaluated for three brainstem fiber pathways that envelope the PPN

(SCP, ML, and LL) (Figure 6, Figure 7). The DBS lead position used for these simulations was consistent with previous clinical studies as noted in the Methods. The two most rostral electrodes (contacts 2 and 3) had the lowest threshold for activation of ML in both the NHP and human models. In contrast, caudal electrodes (contacts 0, 1, and 2) generated higher levels of activation of SCP fibers for both models, especially for the two most caudal electrodes. One distinguishing feature of the human model from that of the NHP model was the strong activation of LL for caudal contacts 0 and 1. No significant activation of LL at stimulation amplitudes under −6V was found in the NHP model, while LL activation could reach nearly 100% in the human model.

2.4.2 PPN cell activation during PPN-DBS

We next quantified the percent activation of PPN cells for each monopolar DBS setting in both the human and NHP models, and then compared the results to threshold voltages necessary to activate adjacent fiber pathways (Figure 6, Figure 7).

The NHP PPN-DBS model results indicated that selective activation of a single PPN cell type was not possible using monopolar cathodic stimulation for any of the electrode contacts studied (Figure 6). For example, while the models pointed towards an overall lower threshold voltage to activate PPN type II over type I cells (contacts 0, 1, and 3), activation was present across both cell types. For monopolar stimulation across contact 2, the voltage-activation relationship was identical between the two cell types. The location of the DBS lead can partially explain these results. For contacts 1 and 3, the lead was slightly closer to PPN type II axons than to type I axons. In the case of contact 0, PPN type I descending axonal projections were located closer to the DBS lead; however, the type I axons coursed parallel to the DBS lead and thus required higher activation thresholds than the more transverse coursing type II axons. Activating the entire population of either type of PPN neurons was also challenging. Even though contacts 1 and 2 were positioned in the central region of PPN, neither contact was able to activate the entire population of PPN neurons until approximately -5V, which also resulted in activation of ~40-80% of SCP. For the two most caudal electrodes (contacts 0 and 1), SCP activation surpassed PPN cell activation.

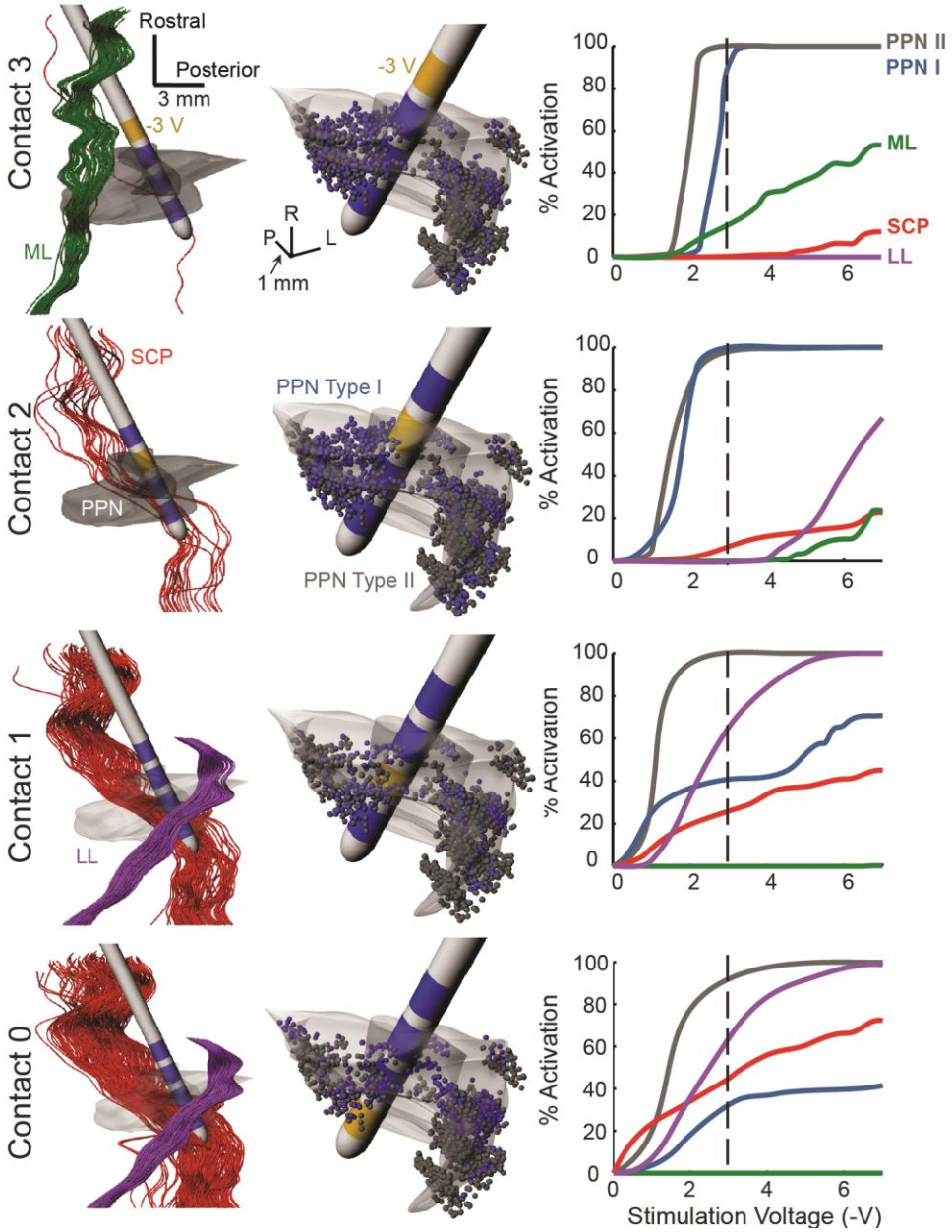

Figure 7. Prediction of neuronal elements activated at -3 V cathodic stimulation in the human model. Each monopolar cathodic DBS setting is modeled using the clinical lead trajectory. The description of the figure labels is identical to that in Figure 6.

In the human model, monopolar stimulation resulted in two distinct activation profiles, corresponding to contacts 2 / 3 and contacts 0 / 1 (Figure 7). For contacts 2 and 3, the two PPN cell types had nearly equal activation due to the proximity of these rostral contacts to the ascending thalamic and nigral projections from PPN. Selective activation of PPN cells over adjacent fiber pathways was possible in the human model when stimulating

through the rostral contacts. For contact 3, however, achieving a high level of activation of both PPN cell types resulted in activation of a small percentage of ML fibers. Large activation of PPN type II cells was also found for contacts 0 and 1, but was accompanied by over 60% activation of LL and over 30% activation of SCP. Similar to the NHP model, PPN type II cells were found to have an overall lower threshold for activation, which again may be due to proximity of the active electrode to the PPN type II population.

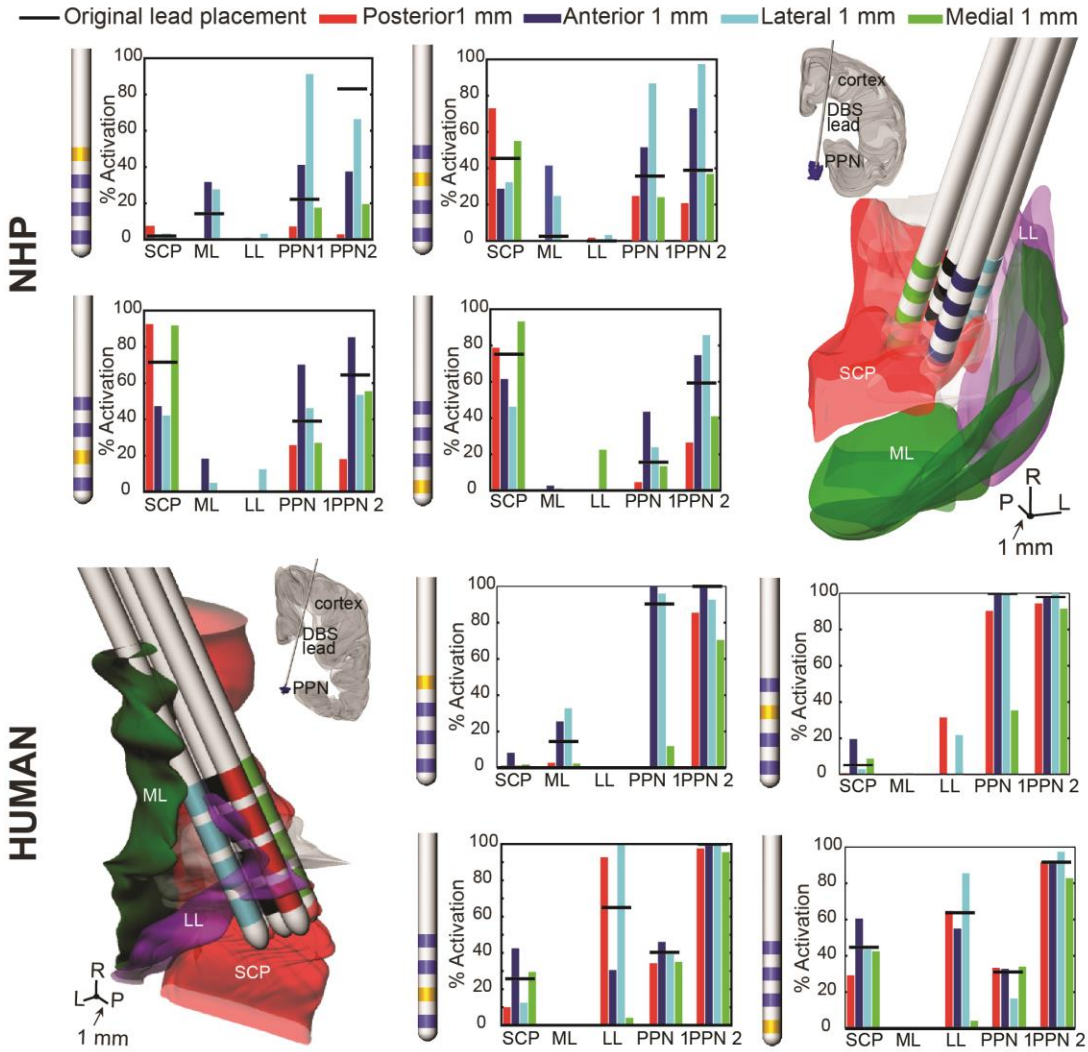

Figure 8. Model sensitivity analysis of off-target lead trajectories.
The effects of moving the lead on activating fiber pathways and PPN cells in NHPs (top) and humans (bottom) are shown. The anatomical images show the trajectory of a DBS lead identical to that used in Figure 6 and Figure 7 (black), as well as a 1 mm shifted trajectories in the anterior (dark blue), posterior (red), medial (green), and lateral (light blue) directions in both the human and NHP models. In both cases, percent activation at each monopolar stimulation setting (-3 V) is shown for each fiber and PPN cell type.

2.4.3 Model sensitivity analysis

Consistent stereotactic implantation of DBS leads in the PPN is challenging given the size and depth of the target **[72]**. Suboptimal clinical outcomes may result if leads are implanted slightly off target **[74]**. Using the same implantation angles, the lead was shifted 1 mm anterior, posterior, medial, or lateral (with respect to the original lead trajectory). We then investigated the effects of stereotactic targeting error on fiber pathway and PPN cell activation using monopolar stimulation at −3V (Figure 8). A 1-mm displacement was found to have a marked effect on activation in both human and NHP models. For example, stimulation via contact 3 in the human model resulted in PPN type I activation ranging from nearly no activation for a posterior or medially shifted lead to nearly 100 percent activation of the population for an anterior or laterally shifted lead. This extreme sensitivity was also found to exist for stimulation via contact 3 in the NHP model for both PPN type I and type II cell activation.

Lead misplacement had a different effect in the human than the NHP model due to differences in the anatomy. Anterior misplacement in the NHP decreased SCP activation by 2% (contact 3) to 24% (contact 1) and increased activation of ML fibers by 18% (contact 1) to 39% (contact 2). LL fibers remained inactivated in all cases in the NHP model. In the human model, moving the lead anterior decreased LL activation by 9% and 35% when contacts 0 and 1 were activated, respectively (the two rostral contacts did not activate LL). SCP activation increased when the lead was moved anterior in all cases, ranging from an 8% (contact 3) to 17% (contact 1) change. PPN type I activation increased for all contacts, while PPN type II activation increased for contacts 0, 1, and 2. In the NHP model, DBS lead implantation error had a strong effect on threshold voltages and relative activation results for both fiber pathways and PPN cells. In contrast, in the human model, the fiber pathway results were, in general, more greatly affected by implantation error than were the PPN cells. In both NHP and human models, there was no ‘ideal’ lead placement that would selectively activate PPN neurons without concurrently activating at least a small percentage of SCP, ML, or LL fiber pathways. In general, there was a trade-off between complete PPN cell activation and activating a large

proportion of the SCP or ML pathways. Since the clinical cylindrical electrode contacts did not provide complete selectivity for PPN cell activation, especially in cases in which the DBS lead was not implanted through the center of PPN, we investigated other DBS lead designs.

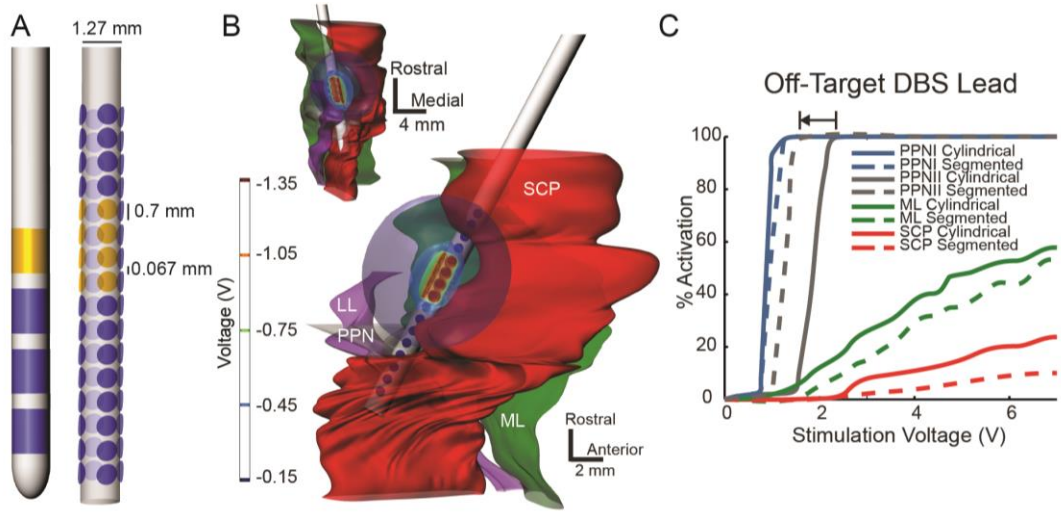

Figure 9. Lead design comparison for improving the selectivity of PPN activation over adjacent fiber pathways for off-target DBS lead implants.
(a) comparison of the clinical cylindrical electrode lead and the revised radially-segmented electrode lead. Active contacts are shown in yellow. (b) Both leads were modeled 1 mm off-target in the anterior direction. Active electrodes in the radially-segmented case faced away from ML in a rostral-posterior direction. (c) Comparison of activation of PPN cells and adjacent fiber pathways using both lead types. LL had no activation below –7 V in both models.

2.4.4 Selectivity with radially-segmented electrodes

Given the suboptimal selectivity results with the clinical DBS lead, which consists of cylindrical electrodes, a DBS lead with radially-segmented electrodes was evaluated using the neuron modeling framework [120]. Lead placement was chosen based on a cylindrical DBS lead implantation trajectory that yielded suboptimal selectivity in the human model (Figure 8, anterior lead placement). Two columns of four electrodes were each activated at the approximate spatial location of contact 3 for the 1-mm shifted anterior lead placement (Figure 9a). This combination of active electrodes resulted in an equivalent active surface area to a single electrode on a 3389 DBS lead. For the radially-segmented electrode DBS lead design, the active contacts were chosen on the posterior side to reduce activation of ML (Figure 9b). Selectivity of activating PPN over SCP, ML, and LL was compared between the two DBS lead types (Figure 9c). The novel lead not

only decreased the stimulation voltage necessary for complete activation of PPN type II neurons, but it also decreased the activation of all fiber pathways, resulting in greater selectivity. This example illustrates how radially- and longitudinally-segmented electrodes can facilitate more robust steering of the electric field not only along the lead, but also around the lead.

2.5 Discussion

Gait and balance problems, which contribute to falls and lack of independence, are arguably the most debilitating and potentially dangerous motor signs of Parkinson's disease [130]–[133]. Current DBS targets for Parkinson's disease, such as the STN, have not been conclusively shown to eliminate gait problems for all patients. STN DBS studies have shown positive results [134]–[138], mixed results [139], and negative results [140], [141] on gait. The PPN is a promising new DBS target for alleviating gait disturbances, given its implicated role in freezing of gait when lesioned [142] and in the generation of locomotor activity when stimulated [64], [143], [144]. In Parkinson's disease, the PPN is thought to be underactive due to overwhelming inhibitory input from GPi [145]–[147] and due to neurodegeneration [148]. However, PPN DBS clinical trials have found inconsistent therapeutic effects in Parkinson's disease patients [69], [83], [84], [126], [149].

The computational models described in this paper provided insight into potential mechanisms underlying these mixed clinical outcomes with PPN DBS. One possible mechanism could be an incomplete activation of PPN neurons with DBS. PPN type I glutamergic cells have been postulated to play a role in gait initiation [4], whereas PPN type II cholinergic cell activation are thought be important for modulating locomotion [143]. Therefore, both cell types are presumably necessary to provide optimal therapy on parkinsonian gait. The models indicated that achieving complete activation of both cell types would be challenging, especially for type I cells. The models also indicated that stimulation amplitudes above -3V were necessary to activate both cell types for most

monopolar electrode configurations. Yet, such amplitudes would likely co-activate fibers of passage.

Another possible explanation for the mixed clinical PPN DBS results could be an overactivation of fiber pathways adjacent to PPN that would obfuscate the therapeutic effects of PPN DBS or that would limit stimulation amplitudes to avoid untoward side effects. In the NHP model, the optimal electrode placement to activate both PPN cell types was in the rostro-lateral PPN or slightly anterior PPN. However, in the former case, a significant percentage of ML fibers would be activated concurrently, likely leading to paresthesia side effects. In the latter case, a very large proportion of SCP would be activated, which could have confounding effects on motor control [20], [150]. In the human model, a rostrally active electrode contact was still important, but a lead trajectory through the middle of PPN was the most beneficial for activating both PPN cell types.

Alternatively, the mixed clinical results could stem from another cell group in the MLR (other than PPN neurons) being the optimal target for DBS. Given that clinical studies on PPN-DBS have reported finding rostral electrode contacts in the more therapeutic cases, the cuneiform nucleus or deep mesencephalic region could potentially be a better therapeutic target for stimulation. In our study, the cellular responses to DBS in these regions were not modeled explicitly, but axons projecting from PPN cell bodies did pass through these areas en route to the substantia nigra and thalamus. Interestingly, the modeling results indicated that rostrally stimulated electrode contracts generated the highest degree of activation of both PPN neuron cell types with good selectivity over activation of SCP. The caveat to using rostral contacts, however, was that the higher the stimulation amplitude used, the more likely ML fibers would also be activated, potentially producing paresthesia side effects. This finding will hold regardless of whether the therapeutic target is PPN or other regions in the rostral portions of MLR.

The models also provided opportunities to interpret how deviation in DBS lead placement affect PPN neuron activation sensitivity and selectivity and how such deviations may explain results reported in previous clinical studies. Moro et al., for example, found that

all patients in their study reported contralateral paresthesia [75], which based on our models likely resulted from the stimulated electrodes being too rostral, posterior, or lateral to PPN. Ferraye et al. noted in their study that the DBS lead targeting was on average 2 mm anterior to PPN with electrodes outside the PPN area [74], similar to that presented in our Figure 9. The observed side effects from this study included ipsilateral oscillopsia, paresthesia and unpleasant sensations of heat, all reversible with reduced voltage. Our human model suggested that for a 1 mm anterior displacement, only contact 2 would have a promising scenario for selective activation of PPN, which may explain the suboptimal outcomes reported in some patients within their study. Stefani et al. [72] showed lead placement that was lateral and rostral to PPN, with putative implantation in the nucleus peripeduncularis (PPD). The placement that was used and the resulting paresthesia side effects reported is consistent with results from our model, since we also found that lateral placement of rostral contacts activated a nontrivial portion of ML. The placement used in their study could explain their findings that PPN-DBS had a therapeutic effect on gait given that a significant portion of PPN cells would likely be activated.

While the anatomy of the NHP and human models show similarities [151], prominent differences were evident in the modeling results. Therefore, one should be cautious when interpreting and translating the results of NHP PPN DBS to human clinical studies of PPN DBS. This finding is important, given current studies investigating the physiological mechanisms of PPN DBS in NHPs [101], [144], [152], [153]. Furthermore, the difference in brainstem anatomy between two humans alone (see [75], Fig. 1) motivates the need for subject-specific models [154]. With structures as small as the PPN that are surrounded so closely by fiber pathways carrying non-motor signals, even slight anatomical differences could have large implications on the effectiveness of PPN DBS therapy. Based on our modeling results, there is little room for implantation error with the current clinical DBS lead design.

The solution to the targeting problem of PPN, and other small DBS target structures, may lie in advancements in DBS lead design. We showed how a DBS lead with radially segmented electrodes could improve activation selectivity of PPN neurons over surrounding fiber pathways. This lead design would provide enhanced flexibility for clinicians, allowing for surgical targeting errors in implantation to be less detrimental to the goal of optimizing therapy for the patient. Additionally, a DBS lead for targeting PPN should be developed with a smaller diameter given that the modeling results indicated that the current clinical DBS lead overlapped with up to 47% of the PPN cells in our models. While additional electrode configurations were not modeled in this study, the increased number of electrodes would provide opportunities to better steer current within the brainstem.

The models do make a number of assumptions that should be noted when interpreting the results. First, the models were developed from histological sections, which may not be representative of the actual sizes and shapes of the underlying anatomy. Future studies that couple our models with high-field imaging data may yield more accurate predictions [99]. Additionally, we assumed that PPN cell soma distributions found in the NHP are homologous to those in the parkinsonian human PPN. Future histological studies in humans will be helpful for comparing PPN cell morphologies between human and NHPs [3], [151]. Also, the membrane dynamics of the modeled PPN neurons were based on healthy rat electrophysiology, given the lack of equivalent data in the parkinsonian human and NHP. We also did not incorporate synapses into the models because their properties have not yet been identified experimentally, which likely produced a conservative estimate of the extent of modulation in the PPN. Finally, it is important to note that a 1 mm displacement of the DBS lead in the NHP model is equivalent to a relatively smaller displacement (~2 mm) in the human model. We modeled the same displacement in both models given that surgical targeting errors are likely to be the same in our experience.

Together, the human and NHP models developed in this study provide a new method to contextualize previous clinical studies in patients with PPN DBS lead implants and compare those results with translational studies in NHPs. These models also provide a useful surgical planning tool for investigators who seek to optimize PPN DBS therapy for treating parkinsonian gait disturbances.

2.6 Acknowledgements

This study was supported by the College of Science and Engineering, the Institute for Translational Neuroscience at the University of Minnesota, and an NIH grant (NS081118). LZ and CG were supported by an NSF-IGERT (Systems Neuroengineering, DGE-1069104) fellowship. We thank Allison Connolly, Ben Teplitzky, Joe Xiao, and Filippo Agnesi for helpful discussion.

3 High-field Imaging Techniques: Brainstem

This chapter modified and reprinted with permission from PLOS ONE.

Laura M. Zitella, Benjamin A. Teplitzky, Daniel J. Kastl, Yuval Duchin, Gregor Adriany, Essa Yacoub, Noam Harel, and Matthew D. Johnson, "*In vivo* 7T MRI of the non-human primate brainstem." *PLOS ONE* 10.5 (2015): e0127049.

3.1 Overview

3.1.1 Objective

Structural brain imaging provides a critical framework for performing stereotactic and intraoperative MRI-guided surgical procedures, with procedural efficacy often dependent upon visualization of the target with which to operate. Here, we describe tools for *in vivo*, subject-specific visualization and demarcation of regions within the brainstem.

3.1.2 Approach

High-field 7T susceptibility-weighted imaging and diffusion-weighted imaging of the brain were collected using a customized head coil from eight rhesus macaques. High-resolution probabilistic diffusion tractography was used to identify fiber tracts, with the results compared to those extracted from sequential application of a two-dimensional nonlinear brain atlas warping algorithm. The nonlinear brain atlas warping algorithm was also used to identify the borders of brainstem nuclei. All techniques were compared to post-mortem histology in two animals.

3.1.3 Main Results

This combination of imaging modalities enabled identifying the location and extent of several brainstem nuclei, including the periaqueductal gray, pedunculopontine nucleus, and inferior colliculus as well as fiber tracts such as the superior cerebellar peduncle, medial lemniscus, and lateral lemniscus. Probabilistic fiber tractography provided accurate representation of fiber tracts when compared to the warping algorithm and histology. In the susceptibility-weighted imaging, white matter tracts within the brainstem were also identified as hypointense regions, and the degree of hypointensity was found to be age-dependent.

3.1.4 Significance

These clinically-relevant high-field imaging approaches have potential to enable more accurate and comprehensive subject-specific visualization of the brainstem and to ultimately improve patient-specific computational models and neurosurgical targeting procedures, including DBS lead implantation.

3.2 Background

Structural brain imaging has become an important tool for guiding neurosurgical procedures, including microelectrode mapping, catheter insertion, ablation, and deep brain stimulation (DBS) lead implantation [1,2]

In practice, however, imaging detailed neuroanatomy of the brainstem with conventional MR scanners (1.5-3T) has been difficult [157] due to overall lack of contrast, small region of interest, and ambiguous borders between nuclei and fiber tracts [100], [158]. Higher field strength scanners have yielded higher-resolution images at 7T [159], [160] and 8T [161], while alternative sequences have provided higher contrast images in parts of the brainstem [162]–[170]. Diffusion-weighted imaging (DWI) at 3T [171]–[173] and 7T [170], [174], [175] and diffusion tractography at 1.5T [61], [176], [177] and 3T[158], [178] have been useful to identify fiber tracts within the brainstem non-invasively; however, these techniques do not include probabilistic tractography and have not been previously validated. Other studies utilizing very high resolution *ex vivo* imaging and histology have been able to identify regions within the human brainstem [179] and validate tractography [180]. However, *ex vivo* imaging is not practical for direct targeting applications so there is need to further integrate *in vivo* high field imaging and high-resolution probabilistic tractography approaches for visualization of structures within the brainstem.

While the development of *in vivo* high field imaging [181], [182] with advanced diffusion weighted imaging sequences [175], [183], [184] has potential to increase the spatial resolution of imaging the brainstem [185], there is also a necessity to validate the contrast maps [58] and quantify how they vary amongst subjects [61]. For example, current *in*

vivo MRI-based techniques to localize the pedunculopontine nucleus (PPN) in the human brainstem have utilized an atlas to predict the coordinates of the PPN in relation to the 4th ventricle and the contrast of proton-density MRI to estimate the general area of the PPN. The atlas-based methods have produced reasonable localization in the lateral and anteroposterior coordinates (within 0.5 mm) but large inaccuracies in the rostrocaudal coordinates (3.3 mm) [100].

Here, we show that a multi-modal imaging approach using 7T MRI *in vivo* enables accurate identification of the PPN, inferior colliculus (IC), and periaqueductal gray (PAG) as confirmed with histology in two subjects. The acquired dataset enabled: 1) investigating what contrast exists in the NHP brainstem using high-field 7T susceptibility-weighted imaging, 2) developing methods to identify structures not directly visible even with high-field MRI, 3) generating probabilistic fiber tractography of the brainstem, 4) assessing the anatomical variability of brainstem structures across eight rhesus macaques, and 5) comparing the nuclei and fiber tract reconstructions to post-mortem histology. Improvements in the visualization of anatomical targets using these tools hold promise for more accurate subject-specific surgical targeting of interventions in the brainstem [186] ultimately influencing the clinical outcomes of neurosurgical interventions in this region of the brain.

3.3 Methods

3.3.1 Data Acquisition

Eight rhesus macaque monkeys (*macaca mulatta, 7 females, 1 male*, Table 4) were scanned at the Center for Magnetic Resonance Research at the University of Minnesota, using a passively shielded 7T magnet (Magnex Scientific) operating with a Siemens console and head gradient insert capable of 80 mT/m and a slew rate of 333 mT/m/s. A radio frequency head coil, consisting of 16 transmit and 16+6 receive channels, with 4 smaller element coils positioned on top of the head for higher sensitivity and 2 ear-loop coils to enhance signal detection from brainstem structures, was designed specifically for primate studies [187]. All procedures were approved by the Institutional Animal Care and

Use Committee of the University of Minnesota and complied with United States Public Health Service policy on the humane care and use of laboratory animals. Animals were housed individually in a Primate Products Enhanced Environment Housing System (12/12 hour light dark cycle) in the Research Animal Resources facility of the University of Minnesota. The animals were given a range of environmental enrichment (e.g. toys, mirrors, TV), provided with water *ad libitum*, and given a range of food options including fresh fruit and vegetables. All efforts were made to provide good care and alleviate unnecessary discomfort, and no adverse events occurred. Animals were anesthetized with isoflurane (2.5%) during the imaging sessions and monitored for depth of anesthesia. At the conclusion of the study and in order to validate the imaging data, two animals were randomly chosen to be deeply anesthetized with sodium pentobarbital and perfused with a fixative solution containing 4% paraformaldehyde, consistent with the recommendations of the Panel on Euthanasia of the American Veterinary Medical Association.

Subject	**Gender**	**Age**	**Resolution (mm)**		
			T1-W	**T2-W**	**SWI**
M1	F	22	0.667 iso	0.4x0.4x0.7	0.4 iso
M2	F	22	0.667x0.667x0.33	0.4x0.4x0.8	0.4 iso
M3†*	F	18	0.5 iso	0.33 iso	0.33 iso
M4*	F	14	0.5 iso	0.33 iso	0.33 iso
M5†	F	13	0.5 iso	0.5 iso	0.4 iso
M6†	F	10	0.667x0.667x0.7	0.4x0.4x0.8	0.4 iso
M7	F	9	0.5 iso	0.5 iso	0.4 iso
M8†	M	4	0.5x0.5x0.249	0.4x0.4x0.8	0.33 iso

Table 4. Subject characteristics and imaging protocols (*iso: isometric*),
† tractography performed, * histological confirmation

Imaging sequences included T1-weighted imaging (T1-W), T2-weighted imaging (T2-W), susceptibility-weighted imaging (SWI), and diffusion-weighted imaging (DWI). T1-W images and T2-W images were acquired with a 3D-MPRAGE sequence and a 2D turbo spin echo sequence, respectively, with the resolutions shown in Table 4. SWI was acquired with a 3D flow-compensated gradient echo sequence using a field of view (FOV) of 128 x 96 x 48 mm^3, matrix size of 384 x 288 x 144 (0.33 – 0.4 mm isotropic

resolution), TR/TE of 35/29 ms, flip angle of 15°, BW of 120 Hz/pixel, and acceleration factor of 2 (GRAPPA) along the phase-encoding direction. DWI was acquired with a single refocused 2D single-shot spin echo EPI sequence [188] using a FOV of 128 x 84 x 99 mm^3, matrix size of 128 x 84 x 50 (1 mm isotropic resolution), TR/TE of 3500/53 ms, BW of 1860 Hz/pixel, and an acceleration factor of 3 (GRAPPA). Diffusion-weighted images (b-value = 1500 s/mm^2) were acquired with diffusion gradients applied along 142 uniformly distributed directions. Fifteen additional non-diffusion-weighted images (b = 0 s/mm^2) were also acquired. To correct for geometric distortions in the EPI images due to magnetic field inhomogeneity we utilized TOPUP [189] in FSL. This technique exploits multiple non-diffusion-weighted (b0) scans with opposite (anterior-posterior and posterior-anterior) phase-encoding directions to calculate and compensate for the deformation field.

3.3.2 **Nonlinear Atlas Registration**

To identify nuclei and fiber tracts that were not visible on the MRI, a rhesus macaque brain atlas [118] was registered and nonlinearly warped to each subject's MRI volume, which was aligned in anterior commissure-posterior commissure (AC-PC) space (Analyze) and resliced in the coronal plane. The algorithm (MATLAB) used a nonlinear affine transformation [190], [191] to individually warp 2D atlas slices to corresponding MRI slices. The first and last atlas plates of the desired warped region were matched identically to coronal MRI slices, and the remaining slices were generated from the existing MRI to match the atlas plates exactly. The slices were cropped to include only the brainstem to reduce computational time of the warping algorithm (Figure 10a,b), which solved for the transformation that minimized the distance between manually-defined seed points on an atlas image with those placed on an MR image (Figure 10c). A fold-back control feature was added in cases when the Jacobian of the transformation function was negative, in which case the warping procedure was compartmentalized into a series of smaller partial deformations to avoid the sign change. The resultant deformed atlas images were imported sequentially into a non-uniform rational B-spline modeling

program (Rhinoceros) to generate 3D surface reconstructions of the individual nuclei and fiber tracts [120], [192] (Figure 10d-f).

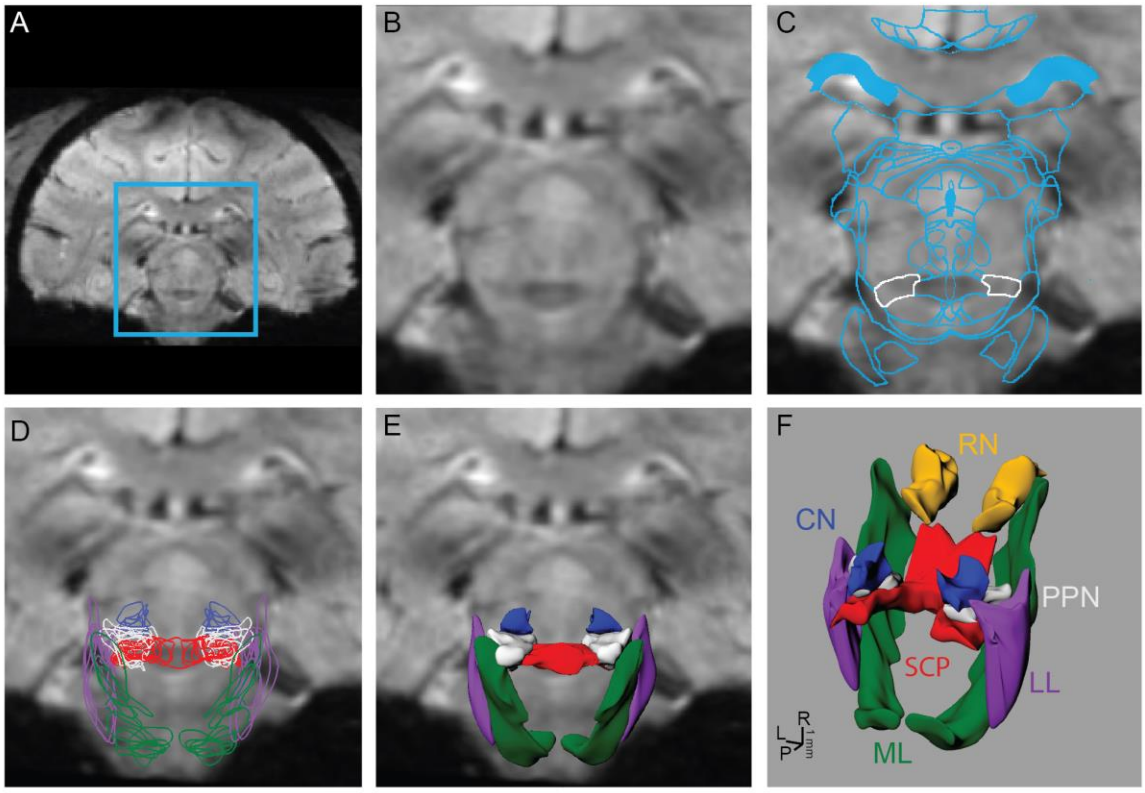

Figure 10. Process for reconstructing brainstem nuclei and fiber tracts in 3D from 7T MRI.
The brainstem region outlined in blue (A) was cropped (B) from each coronal 7T SWI MR image. (C) An affine deformation algorithm based on user-defined seed points was used to warp contours from a rhesus macaque brain atlas to the MRI of each subject. The PPN is outlined in white. (D) Algorithm-defined contours from nuclei and fiber tracts within brainstem were outlined on each slice and then (E, F) lofted to create surface renderings.

3.3.3 **Probabilistic Diffusion Tractography**

In order to obtain accurate 3D visualization of the fiber pathways within the brainstem, we leveraged the warped slices described above to guide the seed points for probabilistic diffusion tractography in FSL in four subjects (M3, M5, M6, and M8) [193]–[195]. SWI DICOM image sets were converted to NIfTI files (dcm2nii DICOM to NIFTI converter) and imported into FSL. The cranium was removed from the images using the brain extraction tool (BET) in FSL [196]. For all subjects, FLIRT linear registration tool in FSL with 7 degrees of freedom (DOF) was able to obtain a sufficient alignment between the SWI data and diffusion data [197]–[199], with the latter undergoing a pre-processing

routine using the *bedpostx* command to estimate diffusion parameters. An inter-modal cost function (correlation ratio and mutual information-based options) was used because the two images were of different modalities. The output transformation matrix was used to transform the coordinates of objects between SWI and DWI spaces.

Masks were created in the SWI data in FSLView by manually highlighting pixels where a particular tract began in the caudal brainstem or cerebellum. For the superior cerebellar peduncle (SCP) and medial lemniscus (ML) tracts, a mask of the entire thalamus was segmented manually in FSL and used as a waypoint for the tractography analysis. This ensured that the tracts were not overly guided and that the tractography results could be evaluated for how selectively they projected to their functionally-specific region of thalamus. This process is shown for the placement of the seed mask in the caudal pons to run the tractography algorithm for the ML and its projection into the ventral posterolateral pars caudalis nucleus of thalamus (ventralis caudalis in humans) (Figure 11). In order to reconstruct the portion of the lateral lemniscus (LL), a seed mask was placed just dorsal to the medial lemniscus seed mask with a waypoint mask segmented in the medial geniculate body (MGB) by way of the inferior colliculus (IC). Tractography of the SCP was more complicated due to its decussation in the midbrain. From the decussation, the majority of the crossed fibers are known to ascend to the red nucleus and either terminate there or continue rostrally to the motor nucleus of thalamus [113]. In order to identify this pathway, the seed masks were placed in the posterior pons with way point masks placed at the decussation of the SCP and the entire contralateral thalamus. In two animals (M6 and M8), an additional waypoint in the red nucleus (RN) was used to better identify the SCP tract.

The masks were then transformed into DWI space using the inverse of the transformation matrix calculated using FLIRT. To compute the tractography, each mask was specified as a seed point mask or a waypoint mask in the *probtrackx* command. The resultant NIfTII file, the output of *probtrackx*, was then transformed back into SWI space for visualization purposes. A threshold was applied to the tracts (Amira, Hillsboro, OR), and AC-PC

alignment was used to align the warped nuclei with the tracts as a validation of both the tracts and the warping algorithm.

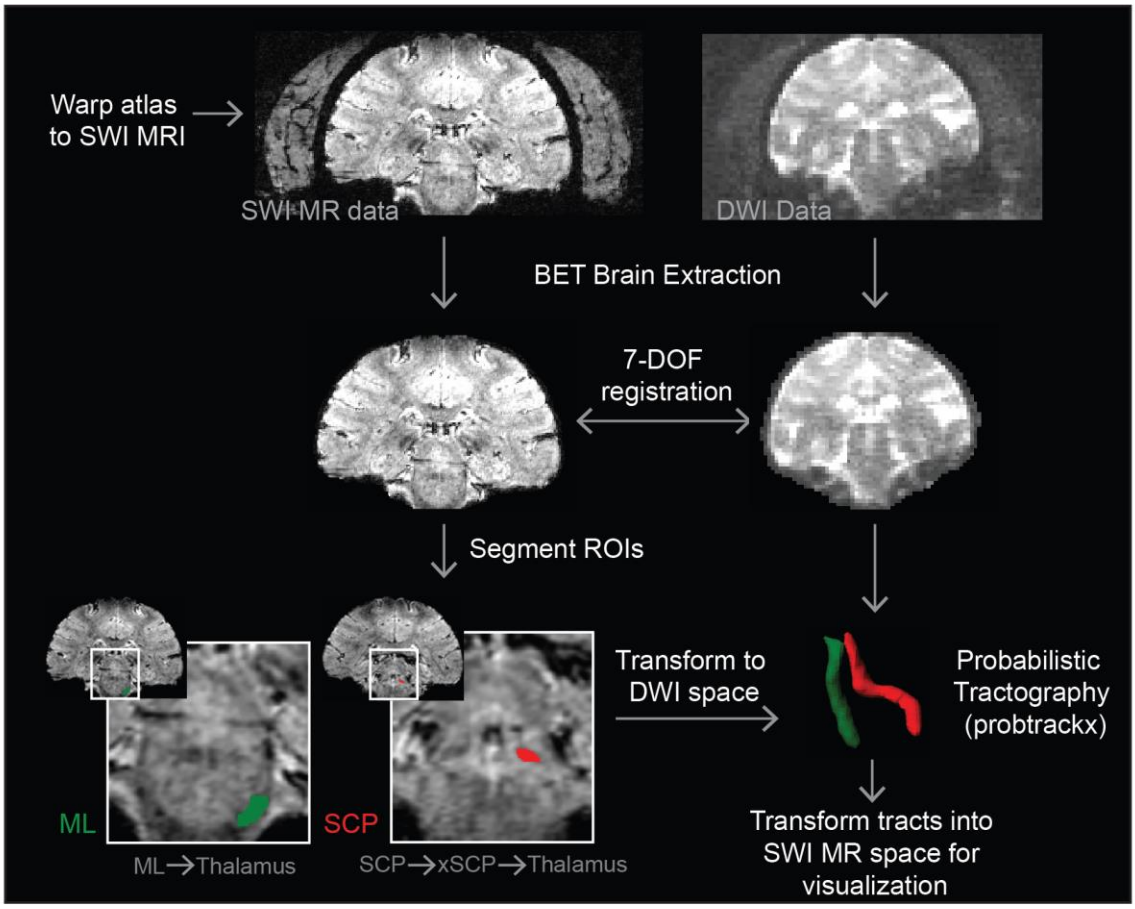

Figure 11. Process to compute subject-specific diffusion tractography.
The method combines the warping algorithm and diffusion tractography methods in FSL to identify fiber tracts. Colored regions are the segmented regions used in FSL to identify both ML and SCP tracts.

3.3.4 **Immunohistochemistry**

Following completion of all imaging studies, monkey M3 and M4 were deeply anesthetized and given a lethal dose of sodium pentobarbital (100 mg/kg, i.v.). Transcardial perfusion consisted of 0.9% NaCl at room temperature (r.t.) delivered at a rate of approximately 50 ml/min for 40 min followed by 4% paraformaldehyde at 4°C delivered at the same rate for 60 min. The brain was removed and post-fixed with 4% paraformaldehyde in 25mM phosphate buffered saline, pH 7.4 (PBS) at 4°C for 7 days. After fixation, the brain was blocked and cryoprotected in 15% sucrose in PBS at 4°C.

Coronal sections, 50 µm thick were cut using a freezing microtome and stained using immunohistochemistry.

The immunohistochemical method used for M3 and M4 was carried out on free-floating sections using avidin-biotin-peroxidase complex method. Brain sections were washed in 0.1% bovine serum albumen (Jackson ImmunoResearch Laboratories, West Grove, PA; cat# 001-000-162) in PBS (PBS+BSA) for 3 × 10 min at room temperature (r.t.). Sections were then incubated in 0.3% Triton X-100 in PBS+BSA containing the primary antibody, a monoclonal anti-acetylcholinesterase (anti-AChE [HR2]; AbCam, Cambridge, MA, USA; cat# ab2803; diluted 1:5000) for 24 h at 4°C. Sections were then washed in PBS+BSA for 3 × 10 min at r.t. before being incubated in PBS+BSA containing the secondary antibody, a biotinylated goat anti-mouse IgG (Vector laboratories, Burlingame, CA; cat# BA-9200; diluted 1:200) for 45 min. at r.t. Sections were processed using the ABC Elite kit (Vector laboratories, Burlingame, CA; cat# PK-6100; diluted 1:50), washed again in PBS+BSA for 3 × 10 min at r.t., and finally reacted with a solution of 3% H_2O_2, 73µg/ml 3,3′-diamino benzidine tetrahydrochloride in 0.05 M Tris, pH 7.6. Sections were then mounted on charged glass slides and allowed to dry overnight. Slides were dehydrated through 100% ethanol, cleared in Histoclear II (Electron Microscopy Sciences, Hatfield, PA; cat# 64111), and coverslipped using DPX Mountant (Sigma-Aldrich, St. Louis, MO; 06522). Images were captured under 10x magnification and automatically stitched together using Adobe Photoshop (CS5; San Jose, CA).

3.4 Results

3.4.1 **Probabilistic Tractography across Subjects**

Tractography in the brainstem can be difficult to calculate accurately in cases of small feature sizes and high density of divergent fiber tracts that can include decussations. In four subjects (8 hemispheres), structural SWI scans and warped slices were used as a guide to define seed points and waypoints for probabilistic tractography analysis of the SCP, ML, and LL (Figure 12). Whereas a single region of interest for seed and way points was sufficient to identify ML and LL fiber tracts, additional waypoints were

needed to delineate SCP at its decussation. Additionally, in 4 of 8 hemispheres, inclusion of an RN waypoint was necessary to obtain a fiber tract that targeted the cerebellar-receiving area of thalamus. While fiber tract consistency was evident across hemispheres, subject-specific variability was also present (Figure 12). The fiber tractography results were compared to atlas-warped reconstructions of fiber tracts transformed into diffusion tractography space. The reconstruction overlap within the brainstem between tractography and nonlinear atlas warping, was 45±4% (mean ± std. dev.) for SCP, 45±24% for ML, and 39±13% for LL, which reflected consistent albeit slight misalignments in which tract borders identified through the nonlinear warping approach were rendered slightly caudal to the diffusion tractography volume reconstructions.

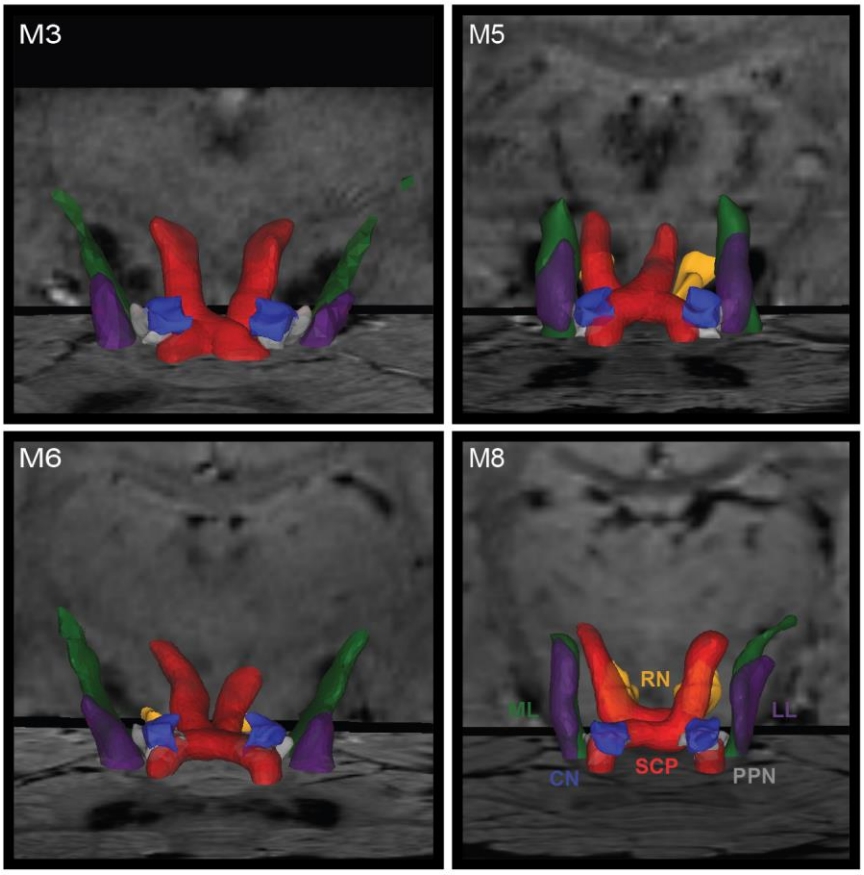

Figure 12. Brainstem tractography displayed with warped nuclei in four rhesus macaques.
Tractography is shown for SCP (red), LL (purple), and ML (green). SCP is shown to course through PPN (grey) and around RN (gold).

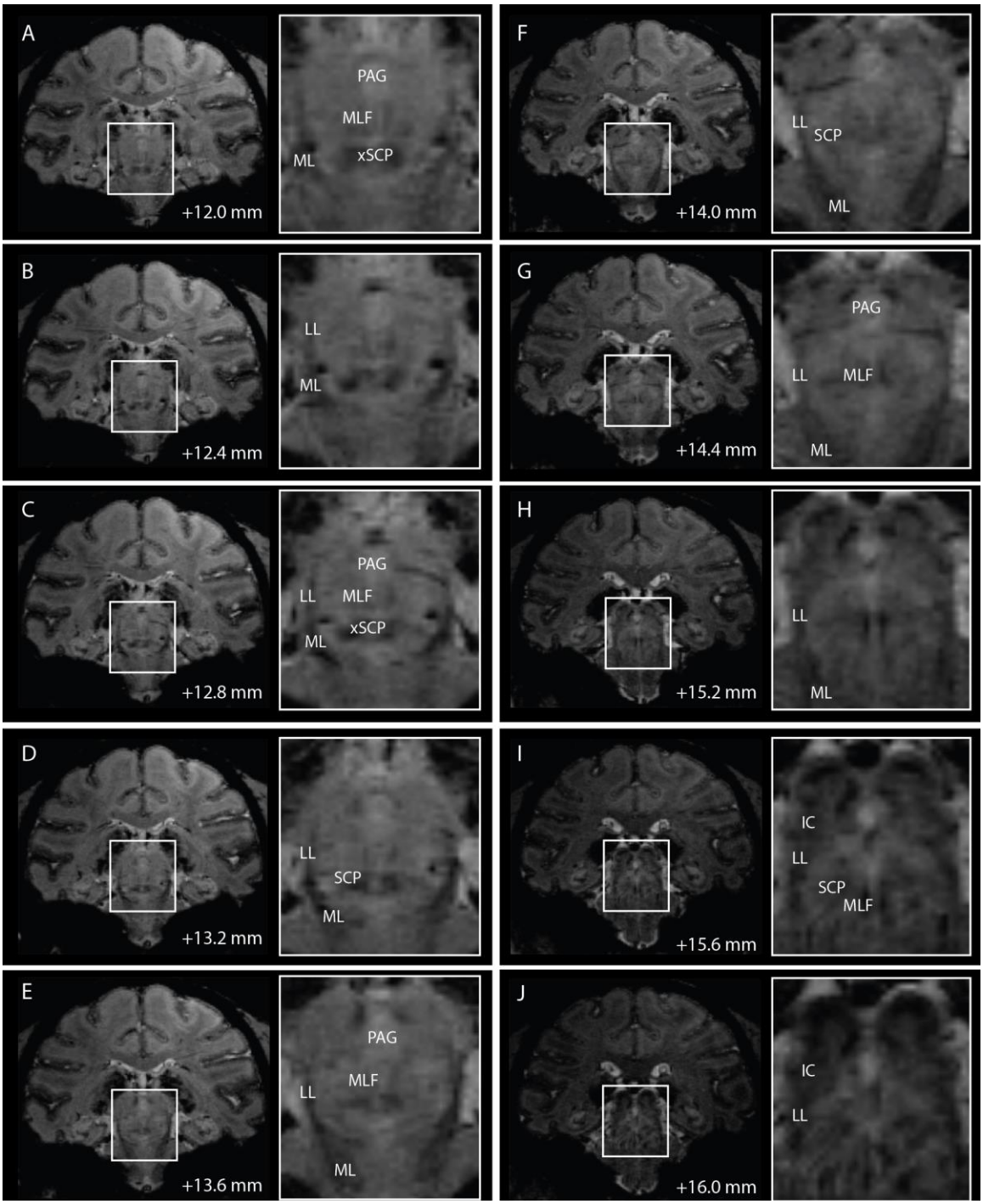

Figure 13. Coronal slices of 7T SWI of the brainstem in subject M2.
Distance of each slice from the midline crossing of the anterior commissure are noted at the bottom of each coronal slice.

3.4.2 **Visualization in Brainstem with 7T Imaging**

While nuclei such as the red nucleus were visible on T2-W images, little contrast was present within other brainstem regions with either T1-W or T2-W imaging. Conversely, high field 7T SWI using the sequences described above provided improved contrast to visualize borders of several brainstem nuclei and white matter tracts that are relevant to neurosurgical targeting procedures (Figure 13).

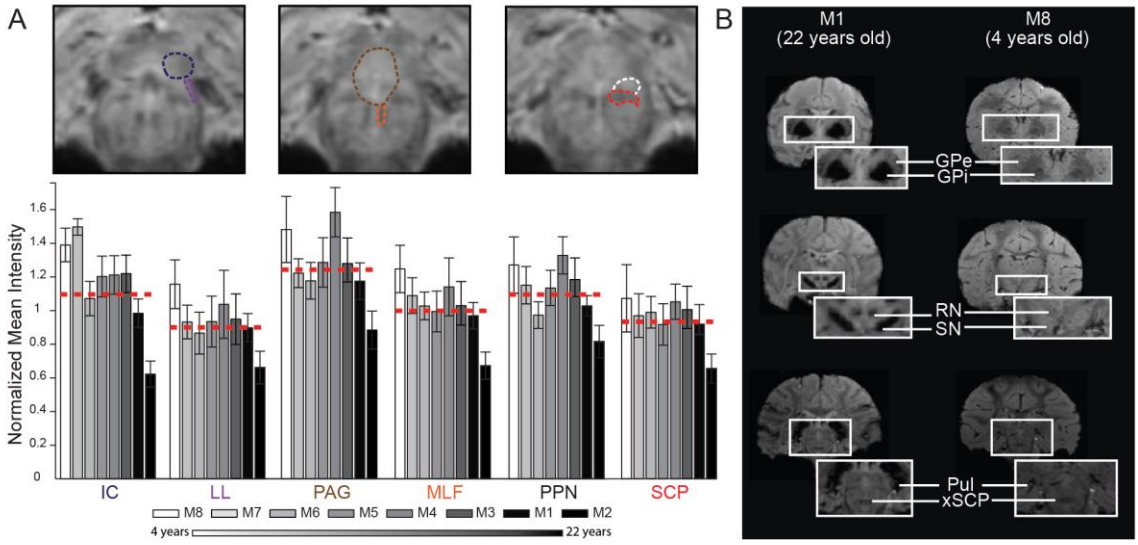

Figure 14. Comparisons of SWI normalized pixel intensity across brainstem regions and rhesus macaques. (A) Analysis of three paired brainstem nuclei and adjacent fiber tracts, each corresponding to an investigational target for DBS therapy. Pixel intensity values were calculated by averaging pixel intensities for each region (0 = black, 255 = white) from the raw SWI scans and dividing by the average pixel intensity values of the anterior commissure about the midline. Columnar intensity values are plotted in age order with white being the youngest and black being the oldest subject. (B) Example of age-dependent SWI pixel intensity across basal ganglia, thalamus, and brainstem structures.

Regional variation in brainstem pixel intensity was quantified for three DBS target nuclei (IC, PAG, and PPN) and compared to the pixel intensity within a white matter tract adjacent to each target (LL, medial longitudinal fasciculus (MLF), and SCP, respectively) (Figure 14). Anatomical borders for each nucleus and fiber tract were defined from the warped atlas reconstructions in each primate. Normalized mean pixel intensity was then calculated by dividing the average pixel intensity for each region by the average pixel intensity of the anterior commissure about the midline for each subject. The anterior commissure was chosen for normalization since its intensity was not found to correlate with age, based on a linear regression analysis (r^2=0.0735, slope=0.6057, p=0.4839). In

almost all cases, white matter tracts displayed a lower mean intensity ratio than nuclei adjacent to them within the brainstem, where a lower ratio represents a more hypointense region on the susceptibility-weighted image.

Additionally, SWI data showed age-dependent normalized mean intensities for nuclei and white matter tracts, with older animals exhibiting greater hypointense imaging within the brainstem (Figure 14a). For example, M8 (4 years) had a ratio of 1.07 for SCP, while M2 (22 years) had a ratio of 0.656. Overall, correlation analysis (Spearman's ρ, df=6, N=8, $p<0.05$) showed that normalized mean intensity for two out of the three fiber tracts had a statistically significant dependence on age (MLF: r=-0.8571, p=0.0065, and SCP: r=-0.7143,p=0.0465) as did the inferior colliculus (IC: r=-0.8095, p=0.0149) but not LL (r=-0.6190, p=0.1017), PPN (r=-0.5238, p=0.1827) and PAG (r=-0.5238, p=0.1827). These age-dependent intensity findings were found to extend to other subcortical nuclei as well, including the RN, GP (internal and external segments), and substantia nigra (Figure 14b).

3.4.3 Comparison of Brainstem Nucleus Morphology across Subjects

Morphological dimension of a select group of brainstem nuclei, including the RN, PPN, and CN, were quantified using two approaches. First, the volumes were calculated from 3D lofted surfaces of each of these brainstem nuclei using reconstructions from each hemisphere of each subject (Figure 15a). Amongst all subjects, the data showed similar volumes between hemispheres for each nucleus (Kruskall-Wallis test, $p>0.05$). To further quantify the morphologies of each of these brainstem nuclei, the 3D lofted surfaces were compartmentalized into tetrahedrons using Delaunay triangulation. The centroids of each tetrahedron were averaged according to the volume of each tetrahedron and the centroid of the entire 3D surface was calculated. Vertices extending from the centroid and intersecting with the lofted surface were tabulated in a histogram for reach nucleus (Figure 15b, c). In comparison to RN and CN, PPN had relatively more morphological variability amongst subjects, which presumably stems in part from PPN being a distributed collection of cholinergic and glutamatergic neurons oftentimes embedded within SCP as shown through our histological analysis below.

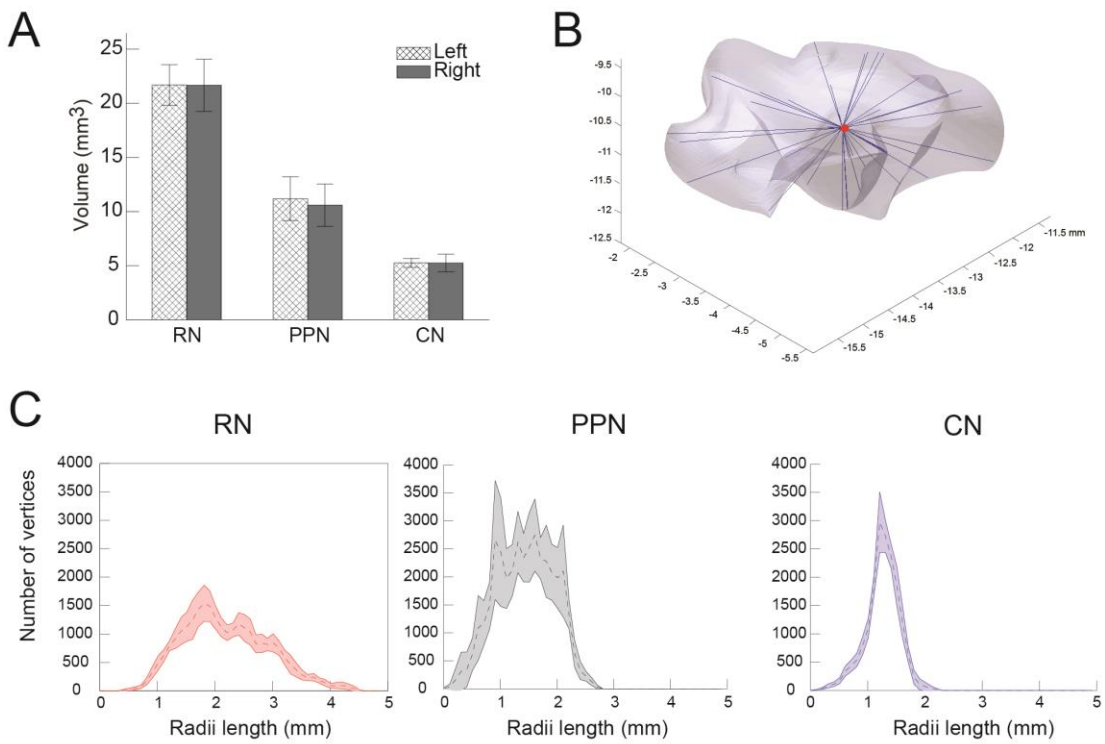

Figure 15. Morphological comparison of reconstructed nuclei across hemispheres and subjects.
(A) Reconstructed volumes were compared between hemispheres and amongst subjects (mean ± standard deviation). (B) Morphological symmetry was assessed using radiating vertices from a reconstructed volume's centroid as shown for the PPN (NHP M3, left hemisphere). (C) Histograms of the vertices' lengths for RN, PPN, and CN with fill regions indicating standard deviation across hemispheres and subjects (n=14).

3.4.4 **Histological Confirmation of 7T Imaging in Brainstem**

To confirm the location of nuclei and fiber tracts resultant from the atlas-based warping algorithm and tractography, post-mortem histology was performed on M3 and M4. In the case of PAG, little contrast was visible in either the T1-W or T2-W MRI, whereas SWI scans showed consistent hyperintensity of the PAG in comparison to adjacent fiber tracts including the MLF and deep white layer of the superior colliculus in all animals (Figure 16). While all primates displayed subject-specific variability, the hyperintensity of PAG was consistent with the AChE-labeled histological sections and the warped atlas results of the PAG in both M3 and M4.

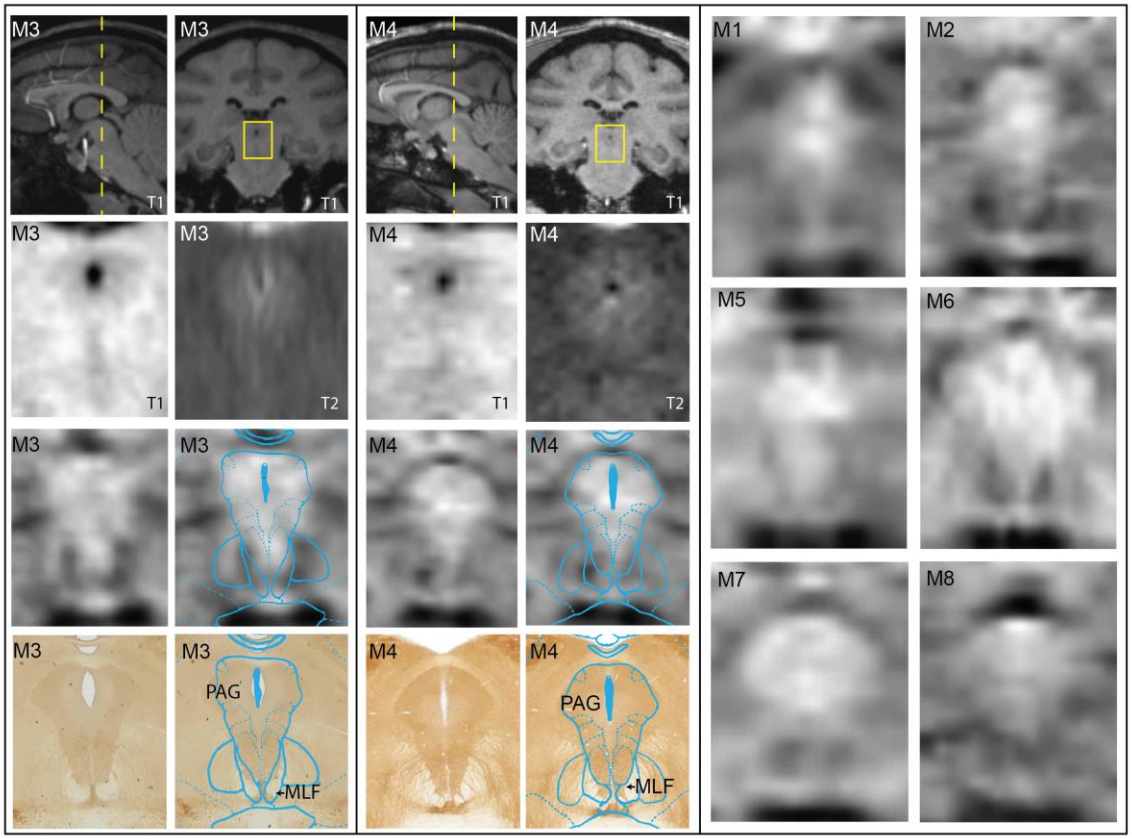

Figure 16. Imaging PAG with comparisons between MRI modalities and immunolabeled histology. Coronal SWI, T1, and T2 images were matched to corresponding histological slices stained with AChE from the same animal (M3 and M4). The corresponding warped atlas was overlaid on both the SWI and the histology. On the right, matched coronal SWI slices are shown for all other animals. Histograms for all coronal MRI slices were not altered, but stretched to encompass the entire spectrum (0-255).

Figure 17 shows 7T imaging results of the PPN region and its adjacent fiber tracts. Similar to the PAG region, there was no meaningful contrast in either the T1-W or T2-W MRI at this level of the brainstem. AChE labeling identified cholinergic cells within PPN in the histological sections and further demarcated adjacent fiber tracts as regions with no labeling. Cholinergic cell labeling was especially notable within and lateral to SCP, which was consistent with a gradation from a hypointense core of the SCP to a diffuse hyperintense region on the lateral border of SCP. Relative hypointense distributions were also found to be consistent with the LL and ML fiber tracts.

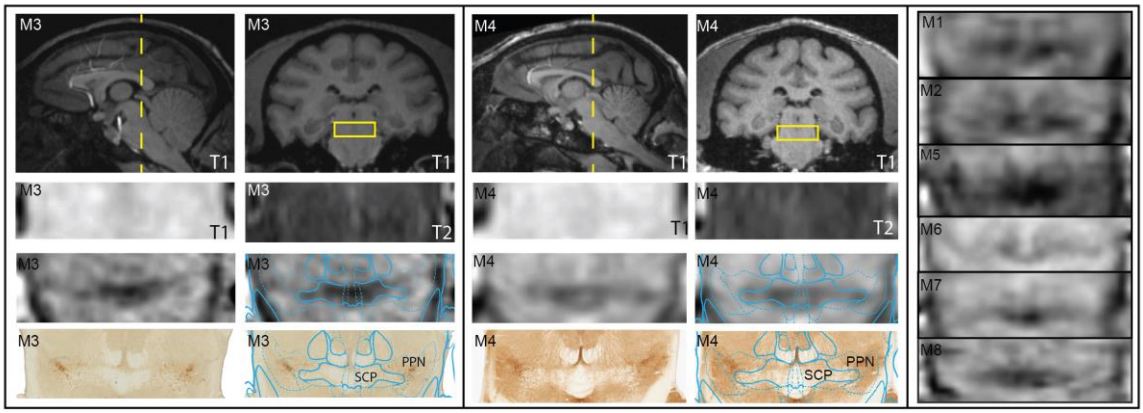

Figure 17. Imaging PPN with comparison between MRI modalities and immunolabeled histology.
Coronal SWI, T1, and T2 MRI were matched to corresponding histological slices stained with AChE from M3 and M4. The corresponding warped atlas was overlaid on both the SWI and the histology. Matched coronal SWI slices are shown for all other animals for comparison. Histograms for all coronal MRI slices were not altered, but stretched to encompass the entire spectrum (0-255).

The warped atlas and histology results were also compared with coronal SWI of the IC (Figure 18). T1-W and T2-W images, while able to demarcate IC, had no variation in contrast within the structure. SWI in eight rhesus macaques (posterior SWI in M2 was not imaged) showed consistency across subjects in visualizing the external borders of IC as well as a fairly robust consistency for most subjects in demarcating the central nucleus of IC as a region of relative hypointensity.

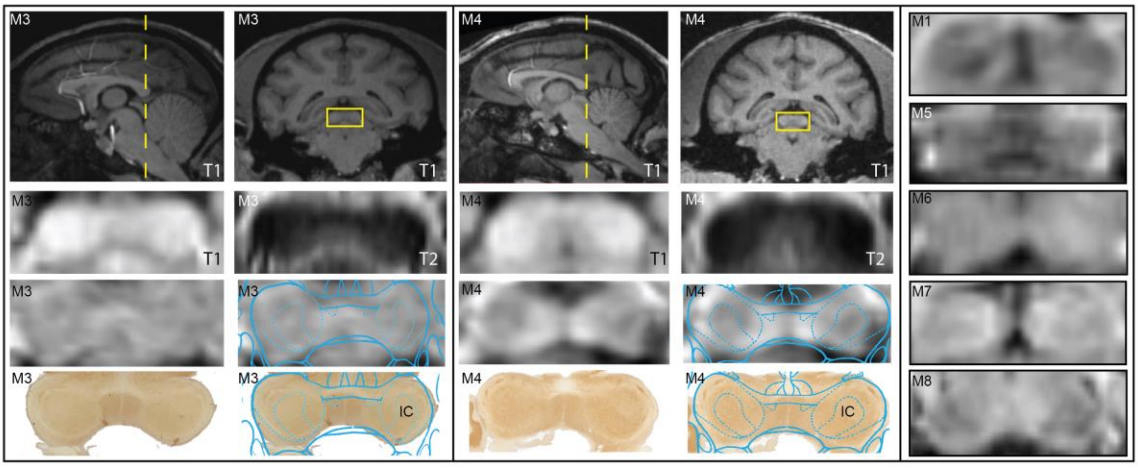

Figure 18. Imaging IC with comparison between MRI modalities and immunolabeled histology.
Coronal SWI, T1, and T2 MRI were matched to corresponding histological slices stained with AChE from M3 and M4. The corresponding warped atlas was overlaid on both the SWI and the histology. Matched coronal SWI slices are shown for all animals for comparison (except M2 in which the 7T MRI scans did not extend to the level of the IC). Histograms for all coronal MRI slices were not altered, but stretched to encompass the entire spectrum (0-255).

3.5 Discussion

Here, we developed a multimodal imaging approach using 7T MRI to identify nuclei and fiber tracts *in vivo* within the NHP brainstem and verified the interpretation of these imaging results with post-mortem histology. This approach to subject-specific imaging, which consisted of SWI at 7T coupled with a nonlinear brain atlas warping algorithm and high angular diffusion weighted imaging with probabilistic tractography, has potential for greatly improving imaging of the brainstem for neurosurgical targeting applications. A similar approach, used by Lenglet et al. [175], combined high-field 7T SWI and DWI in humans to visualize white matter pathways within and between the basal ganglia and thalamus. In this case, manual segmentation coupled with probabilistic diffusion tractography in FSL allowed for delineation of the nigrostriatal, subthalamopallidal, pallidothalamic, and thalamostriatal pathways in humans. Our approach expands upon these techniques with the addition of a nonlinear brain atlas warping algorithm, the application of probabilistic tractography to the brainstem region, and importantly histological confirmation of the imaging results.

DBS within the brainstem is currently under investigation for treatment of parkinsonian freezing of gait (PPN) [69], [75], [79], [72], [83], relieving central pain (PAG) [200], and restoring hearing (IC) [201]. While these regions of the brainstem are certainly difficult to target given their depth and high degree of vascularization [202], the lack of contrast within the brainstem with standard MRI sequences can further limit subject-specific targeting of DBS leads. Visualization of both nuclei and surrounding fiber tracts is important for DBS targeting, as fiber tracts play an important role in accurately interpreting therapeutic outcomes for targets in the basal ganglia [107]–[110] as well as targets in the brainstem [186]. In PPN DBS, for example, adjacent fiber pathways can be activated including SCP, ML, and LL resulting in potential motor coordination problems, paresthesias, and auditory disturbances, respectively [37], [74], [113]–[115]. Similarly, stimulation in the region of the dorsal PAG for relief of pain can lead to adverse sensory side effects, nausea, contralateral piloerection, and cold sensations in the face [203]. For auditory midbrain stimulation targeted to the central nucleus of the IC, targeting errors

can result in poor activation of the underlying tonotopy and potential induction of side effects including paresthesia, dizziness, facial twitch, and temperature sensation [204].

Imaging in NHPs, as opposed to humans, provided a means to both further the translational potential of animal models of DBS and histologically corroborate the interpretation of the high-field imaging data that would otherwise be difficult to accomplish in humans. It is important to note, however, that the methods developed in this study to better visualize nuclei and white matter tracts in the brainstem are directly transferable to human MRI and DWI, as was demonstrated by Lenglet, et al. when visualizing the connectivity patterns of the human basal ganglia [175]. Animal models have been used as investigational tools for many studies including DBS in the brainstem [144], [201], [205], [206] as they are useful for dissecting mechanisms of therapy and optimizing means for delivering therapy. As part of these studies, accurate targeting of DBS leads is critical towards generating data with meaningful and translational outcomes. Using NHPs also enabled histological analysis to relate labeling within fixed tissue with 7T SWI contrast within the brainstem. These results indicated that for SWI in the brainstem, white matter tracts had a relative hypointensity compared to gray matter regions and further that the degree of image intensity depended upon age with older animals exhibiting greater relative hypointensity in the brainstem. Interestingly, the observed image hypointensity in brainstem fiber tracts may not necessarily apply to other brain regions, such as the GP, red nucleus, and substantia nigra, which exhibited strong hypointensity relative to their surrounding white matter tracts.

While many regions within the brainstem had visible contrast differences to adjacent brainstem structures, other regions were more difficult to demarcate. Here we employed a nonlinear warping algorithm to tailor a brain atlas to each subject's imaging data to identify these structures. Current nonlinear warping methods utilize 3D warping based on the cortex, ventricles, or 3D points [207]–[209] or incorporate both MRI and other imaging modalities such as PET [210], [211] or computed tomography (CT) [212]. Deformations, which rely on matching cortical surfaces and relegating this information to the deformation of deep structures, may not provide adequate deformation because it is

not clear that cortical morphology is relevant to morphology of deep structures [213]. The richness of seed point information in the 2D slices, especially at 7T, could provide more accurate results [214]. This process also enabled cropping the cortex from the images and focusing on the brainstem to perform local deformations. The warping algorithm identified nuclei consistent with histological results, which allowed for the accurate placement of seed points for running the tractography analysis. Probabilistic diffusion tractography using high angular diffusion weighted imaging [175] also has strong value especially when fiber tracts run in close proximity to one another and decussate as was the case for the SCP. Care must be taken when interpreting these results, as probabilistic diffusion tractography does not visualize the actual tracts but determines the most likely direction of the fiber tracts based on a measure of diffusion along many directions. However, the combination of the tractography and the precise anatomical borders of the tracts obtained from the SWI could provide a means to more accurately define fiber tracts and their directions within the brain, which would be especially useful for computational models of DBS [108], [120], [186], [215], [216].

Certain limitations should be considered upon interpretation of the results in this study. First, it should be noted that the data set used seven females and one young male rhesus macaque. The choice of these subjects was based on being able to place the receiver coils closer to the brain than would otherwise be possible in older male rhesus macaques with large cranial musculature. Additionally, the warped nuclei and fiber tracts are limited to the regions delineated in the atlas, and these demarcations among nuclei and fiber tracts in the atlas are discrete, whereas some anatomical boundaries are not well defined, as shown for the interdigitation of PPN and SCP. Furthermore, there is a discrepancy between the voxel size of the SWI (0.33-0.4 mm) and the DWI (1 mm). These factors provide some context for the slight variations between the atlas-based fiber tract identification methods and diffusion tractography results. Inherent variability of tracts between animals further necessitates the use of subject-specific techniques that are not based on atlases. Although Duchin, et al. showed that the use of 7T compared to 3T has negligible differences in distortion in the region of the midbrain, further studies are

needed to examine the issue of geometric distortion in the brainstem at high fields and develop methods for their corrections. Other considerations include the use of a brain atlas generated from a single rhesus macaque [118], the method used to loft 3D objects from the warped slices, and the probabilistic nature of the fiber tractography calculation. Additionally, 3D rendering of histology-based fiber tracts [217] may be used to validate tractography and warping methods. While high-field *in vivo* MRI is poised to help demarcate regions within the brainstem pre-surgically for neurosurgical targeting procedures, it cannot account for other factors that contribute to targeting inaccuracies during surgery including probe deflection, brain shift, and microdrive imprecision [218].

Together, these multi-modal imaging techniques (7T SWI, 7T DWI and probabilistic tractography, and nonlinear brain atlas warping) provide subject-specific methods to more precisely identify regions of the brainstem and provide an enabling set of tools to assist in the neurosurgical procedures targeting the brainstem.

3.6 Acknowledgements

We thank the Center for Magnetic Resonance Research (CMRR) for providing the imaging resources and the Minnesota Supercomputing Institute for providing the computational resources to complete this study. We thank all members of the Neuromodulation Research and Technology Lab for their support and assistance. This work was supported by grants from the National Institutes of Health (R01 NS081118, R01 NS085188, P41 EB015891, P30 076408, Human Connectome Project U54 MH091657), the Michael J. Fox Foundation, and the National Science Foundation (IGERT DGE 1069104 to LZ and GRFP 00006595 to BT).

4 Subject-specific PPN DBS Models in the NHP

This chapter reprinted with permission from Frontiers in Computational Neuroscience.

Laura M. Zitella, Benjamin A. Teplitzky, Paul Yager, Heather M. Hudson, Katelynn Brintz , Yuval Duchin, Noam Harel, Jerrold L. Vitek, Kenneth B. Baker, Matthew D. Johnson. "Subject-specific computational modeling of DBS in the PPTg area," *Frontiers in Computational Neuroscience* 9.93 (2015) doi: 10.3389/fncom.2015.00093.

4.1 Overview

4.1.1 Objective

Subject-specific computational models of DBS are a promising tool to investigate the underlying therapy and side effects; however accuracy of these models is imperative. This study uses side effects as a quantitative measure to determine the most accurate model parameters.

4.1.2 Approach

In this study, a parkinsonian rhesus macaque was implanted unilaterally with an 8-contact DBS lead in the PPN region. Fiber tracts adjacent to PPN, including the oculomotor nerve, central tegmental tract, and superior cerebellar peduncle, were reconstructed from a combination of pre-implant 7T MRI, post-implant CT, and post-mortem histology. These structures were populated with axon models and coupled with a finite element model simulating the voltage distribution in the surrounding neural tissue during stimulation. This study introduces two empirical approaches to evaluate model parameters. First, incremental monopolar cathodic stimulation (20 Hz, 90μs pulse width) was evaluated for each electrode, during which a right eyelid flutter was observed at the proximal four contacts (−1.0 to −1.4 mA). Eyelid flutter was attributed to stimulation of the oculomotor nerve. Multiple model parameters were tested, including changes in axon diameter, neural tissue conductivity maps, and lead location, and compared to the experimental data. Second, PET imaging was collected OFF-DBS and twice during DBS (two different contacts).

4.1.3 Main Results

The experimental current amplitudes followed closely with model predicted activation of the oculomotor nerve when assuming an anisotropic conduction medium. The results of the PET imaging supported the model predicted activation of the central tegmental tract and superior cerebellar peduncle.

4.1.4 Significance

Incorporating anisotropic neural tissue conductivity produced much more accurate models, as compared to isotropic neural tissue conductivity models. Subject-specific models provide a framework to more precisely predict pathways modulated by DBS.

4.2 Background

Gait and balance difficulties in Parkinson's disease can be especially debilitating since they increase the risk of falling. For some patients, these symptoms are resistant or poorly managed by levodopa treatment and typical targets of deep brain stimulation (DBS) including the subthalamic nucleus (STN) and internal segment of the globus pallidus (GP). In contrast, low-frequency electrical stimulation delivered within or near the pedunculopontine nucleus (PPN), a component of the mesencephalic locomotor region (MLR) of the brainstem, has shown promising results [69], [68], [219]. Clinical outcomes, however, have varied from patient to patient across these studies, due in part to variation in surgical targeting, uncertainty in the therapeutic target, and the likely modulation of highly excitable, side effect inducing fiber pathways [220] outside the MLR.

A previous computational modeling study showed that clinical outcomes of DBS within the PPN area are likely to be highly dependent upon lead position and stimulation settings [186]. For instance, the superior cerebellar peduncle passes through the PPN en route from the deep cerebellar nuclei to the red nucleus and cerebellar receiving area of the motor thalamus by means of a decussation just rostral to PPN. At present, how selective activation of this pathway affects freezing of gait is unknown, though stimulation of the cerebellothalamo-cortical circuit has been postulated to be beneficial for gait [15]. DBS

in the PPN area may also modulate medial fiber tracts such as the medial longitudinal fasciculus (MLF) or the oculomotor nerve (ON). Side effects from activation of either of these fiber tracts would be expected to affect the eyes and eyelids. Neuronal activation volumes that extend lateral of PPN may include the medial lemniscus (ML) and lateral lemniscus (LL) and lead to paresthesias [221] and changes in auditory perception [204], respectively. Further, spread of current rostral to the PPN may modulate the central tegmental tract (CTG), which rises from the nucleus solitarius and carries gustatory input to the ventral posteromedial nucleus of the thalamus (VPM). There is some evidence that activation of this tract may result in palatal myoclonus [222].

While previous subject-specific computational models of DBS have been developed for the STN [109], [223], [224], tailoring models to the PPN area has been limited because of the poor image contrast within the brainstem with standard MR scanner technology. In recent years, however, advances in structural imaging have made visualizing fiber tracts within the brainstem more readily available. In this study, we leverage susceptibility-weighted imaging (SWI) and diffusion-weighted imaging (DWI) to create subject-specific computational models of PPN-DBS, which can predict activation of individual fiber tracts within the brainstem for any given DBS setting. In order for these models to be informative for clinicians, the models must provide accurate predictions of neuronal activation. The challenge becomes defining behavioral or functional outcome measures to confirm or otherwise modify the selection of model parameters including tissue conductance anisotropy and inhomogeneity, cellular morphology, axonal diameter, and ion channel kinetics among others. Here, we propose two approaches in the context of PPN DBS, namely eliciting an oculomotor side effect and performing DBS within the context of positron emission tomography (PET) imaging.

To examine the pathways modulated in the PPN area during PPN DBS, a subject-specific computational model was developed. In this study, the models were used to (1) investigate the effects of using tissue conductance anisotropy within the brainstem based on diffusion-weighted imaging, and (2) perform model parameter sweeps to determine PPN DBS model sensitivity. The models were evaluated with varying axon diameter,

conductivity values, and DBS lead location, and then compared against behavioral and PET imaging results.

4.3 Methods

4.3.1 Subject

Two female rhesus macaque monkeys (macaca mulatta, Monkey L and Monkey P) were used in this study. All procedures were approved by the Institutional Animal Care and Use Committee of the University of Minnesota and complied with United States Public Health Service policy on the humane care and use of laboratory animals. The animals were housed individually with environmental enrichment, provided with water ad libitum, and given a range of food options including fresh fruit and vegetables. All efforts were made to provide good care and alleviate any discomfort for the animals during the study.

Pre-operative 7T MRI was acquired at the Center for Magnetic Resonance Research (CMRR) at the University of Minnesota using a passively shielded 7T magnet (Magnex Scientific) for both animals. During the imaging sessions, the animals were anesthetized with isoflurane (2.5%) and monitored for depth of anesthesia. Susceptibility-weighted imaging was acquired with a 3D flow-compensated gradient echo sequence at 0.4 mm isotropic resolution using a field of view (FOV) of 128 × 96 × 48 mm3 . Diffusion-weighted images (b-value = 1500 s/mm2) were acquired with diffusion gradients applied along 110 uniformly distributed directions using a 128 × 84 × 99 mm3 FOV (1 mm isotropic resolution). The 3D tensors were calculated as ellipsoidal functions, to identify the orientation of maximum value [225], [226].

In Monkey L, a cranial chamber was mounted on the head to facilitate implantation of the DBS lead, as described previously [119]. The high-field imaging, along with results from electrophysiological microelectrode mapping of the PPN area, were superimposed in Monkey Cicerone [218] to define a trajectory for unilateral implantation of a scaled-down version of a human DBS lead (2F diameter, 8 annular electrode contacts: 0.5 mm height, 0.25 mm spacing) (NuMed, Hopkinton, NY) in the region of the PPN (right hemisphere).

Following lead implantation, a post-operative CT scan was performed under Ketamine and Dexdomitor anesthesia to visualize the implantation trajectory and depth in Monkey Cicerone. The preoperative SWI was co-registered with the postoperative CT to determine the DBS lead location relative to nuclei and fiber tracts within the brainstem. After instrumentation with the chamber and the DBS lead, the subject was rendered parkinsonian with systemic injections of 1-methyl-4-phenyl-1,2,3,6-tetrahydropyridine (MPTP).

At the conclusion of the study, both animals were deeply anesthetized with sodium pentobarbital and perfused with a fixative solution containing 4% paraformaldehyde, consistent with the recommendations of the Panel of Euthanasia of the American Veterinary Medical Association. After fixation, the brain was removed, blocked, and cryoprotected in 15% sucrose in phosphate buffered solution. Coronal sections (50µm) were cut using a freezing microtome and labeled for Nissl. In the case of Monkey L, the DBS lead trajectory was again reconstructed from these histological images using Mimics (Materialise, Leuven, Belgium), which confirmed the in vivo estimation of the DBS lead trajectory that had been generated from co-registration of the pre-implant SWI with the post-implant CT.

4.3.2 Axonal Model Morphologies

Several imaging-based tools were used to reconstruct the three-dimensional morphologies of the PPN area for use in the subject-specific finite element model and multi-compartment neuron model simulations (Figure 19a,b). The SWI volume was aligned in anterior commissure to posterior commissure (AC-PC) space with Analyze (AnalyzeDirect, Overland Park, KS), and then resliced to generate images that matched atlas plates from a rhesus macaque brain atlas [118]. A nonlinear affine atlas registration algorithm based on a moving least squares fit applied to each image voxel was used to identify the borders of the PPN, CTG, and ON. The algorithm involved the selection of analogous control points placed on each MR image and each corresponding atlas plate. Contours were traced from these warped atlas reconstructions in Rhinoceros (McNeel,

Seattle, WA) and lofted into 3D surfaces using a nonuniform rational B-spline modeling approach. Results from the warping algorithm were aligned to the DWI using FLIRT, which provided anatomical context to guide the placement of seed points for probabilistic diffusion tractography calculations in FSL [193]. To identify the SCP tract, seed points were placed in the cerebellar outflow tract caudal to the decussation, with waypoints defined at the decussation of SCP and the entire contralateral thalamus. Manual thresholding of the output of probtrackx was performed in Amira (FEI, Hillsboro, OR) to produce the final tract geometry.

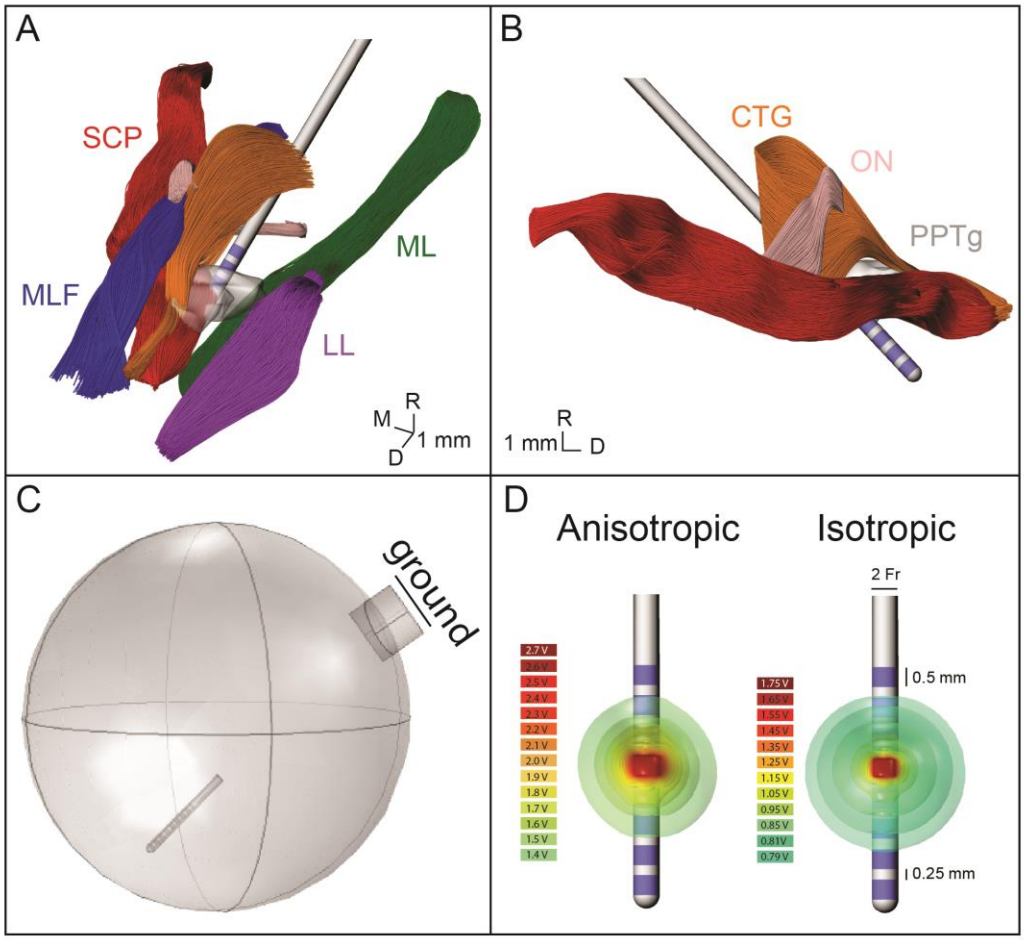

Figure 19. Model geometry and FEM.
(A) The geometry of the fiber pathways in the PPN area in relation to the DBS lead location. CTG, central tegmental tract – orange; ON, oculomotor nerve – pink; SCP, superior cerebellar peduncle – red; MLF, medial longitudinal fasciculus – blue; ML, medial lemniscus – green; LL, lateral lemniscus – purple; PPN, pedunculopontine tegmental nucleus – gray. (B) Sagittal view of the geometry of the modeled fiber pathways. (C) The FEM geometry, showing the lead location and grounded chamber. (D) Electric potential isosurfaces for the anisotropic and isotropic model.

4.3.3 Finite Element Models (FEM)

A finite element model of the DBS lead and surrounding neural tissue was created in COMSOL (Figure 19c). The variable resolution tetrahedral mesh was constructed with a maximum element size of 0.2 mm for the electrodes and 1.6 mm for the lead, encapsulation layer, and neural tissue. The final mesh consisted of 447280 elements with a finer resolution near the electrode-tissue interface. A point current source was modeled at the geometric center of each electrode, and the entire lead was surrounded by a 250µm encapsulation layer with a conductivity of 0.18 S/m. A 20 mm radius sphere around the electrode represented the neural tissue. A cylinder was placed on the edge of the sphere to represent the cranial chamber, and the chamber outer surface was assigned as ground (Figure 19c). For the isotropic FEM, conductivity of the neural tissue was homogeneous, 0.3 S/m. For the anisotropic FEM, the neural tissue conductivity was calculated from the 6-direction DTI tensors, based on an estimated linear relationship between the conductivity (σ) and diffusion tensor eigenvalues [227].

$$\sigma = s * D$$

where s was set to 0.844 and D represents the diffusion tensor eigenvalues. These conductivity matrices (Figure 20a,b) were imported into COMSOL and interpolated onto the mesh using the nearest neighbors function. Voltage distribution during monopolar stimulation through each electrode were solved for using anisotropic and isotropic conductivity models with COMSOL (Figure 19d) [228]. The extracellular voltage predicted from the FEM solution was then interpolated at each nodal compartment along each multi-compartment axon model.

4.3.4 Biophysical Modeling of DBS in the PPN Area

SCP, ON, and CTG were each randomly populated with multi-compartment cable models of 1000 myelinated axons, ranging in diameter from 2 to 8.7µm [107], [109], [122], [229]. The axonal models included nodes of Ranvier, paranodal, and intermodal segments as well as a myelin sheath [123]. Nodal compartments were given biophysical mechanisms related to a nonlinear fast Na+ channel, persistent sodium channel, slow K+

channel, and a leakage current. The paranodal compartments were instantiated with a slow K+ current. Both intermodal and myelin compartments had only passive mechanisms, including a membrane capacitance (Cm = 2 μF/cm^2) and axoplasmic resistivity (70 Ω-cm). Stimulus thresholds for evoking action potentials within the modeled axons were estimated in the NEURON v7.3 programming environment [124]. Stimulus perturbations were inserted using the NEURON mechanism, extracellular, for each axonal compartment. Stimulus pulses (90μs pulse width) were delivered at a rate of 20 Hz. Activation was defined by the lowest amplitude to elicit one or more action potentials within 1–3 ms following each stimulus pulse for at least 8 of 10 stimulus pulses.

4.3.5 Motor Side-Effects of DBS in the PPN Area

A monopolar review was conducted to determine the electrical stimulation amplitude thresholds for eliciting an overt motor side effect, which for this lead implantation was found to be a right eyelid flutter. In this case, stimulation was delivered through an externalized current-driven pulse generator (Precision, Boston Scientific) with a cathode applied individually to each contact and a return set to the cranial chamber. The stimuli were delivered as a 20 Hz train of 90μs pulses in 0.1 mA increments until the eyelid flutter was observed visually by the investigators, as shown in Table 5.

Contact	Stimulation frequency (Hz)	Threshold (mA)	Side effect
7	20	1.0	R eyelid flutter
6	20	1.1	R eyelid flutter
5	20	1.4	R eyelid flutter
4	20	1.4	R eyelid flutter

Table 5. Motor side-effect thresholds.

4.3.6 PET Analysis

Approximately 1 year after implantation of the DBS lead in Monkey L, PET/CT was collected using a Siemens Biograph 64 slice scanner on three different days within an 8-day period. A full 24 h before each scan, the subject was withheld from any stimulation or medication. The subject was fasted beginning at 1700 the night prior to the scan [230], with fasting blood glucose verified the morning of the scan. Thereafter, the proximal end

of the DBS lead was connected to the external pulse generator and a single 8 mCi dose of 18- FDG was administered intramuscularly. As listed in Table 6, immediately following this injection either 20 Hz PPN-DBS was applied at one of the two contacts of the DBS lead or no DBS was applied (baseline scan). The subject sat still in a quiet, familiar environment without stimuli while this treatment was administered. After 45 min, general anesthesia was induced using ketamine (10 mg/kg) and diazepam (0.5 mg/kg) [231], [232], and the subject was moved to the scanner for imaging. Reconstruction yielded a voxel size of 1.018 × 1.018 × 2 mm. The subject was then released to an isolation room until radioactivity was undetectable.

The PET images were analyzed with methods similar to those described previously [232], [233]. Each non-contrast CT scan was transformed by rigid, manual co-registration [234] to align with a standard MRI template, INIA19 Macaca mulatta [235], with the resultant transformation values individually applied to the PET image from the corresponding data acquisition session to align them to the normalized space. Finally, a preoperative MRI, taken before the cephalic hardware and DBS lead had been placed, was aligned with the INIA19 MRI to verify fit. The 1210-MRIderived-VOIs of the INIA19 template, were used within PMOD software (PMOD Technologies, Zurich, Switzerland) to compile statistical measures. Mean voxel value, standard deviation, and number of voxels were collected as standard uptake values (SUV) [230]. All scans were scaled so that the left occipital white matter uptake was equivalent. Volumes of interest were then consolidated to yield larger brain structures, decreasing the resolution from 1210 volumes of interest into a manageable grouping for analysis. The scaled images had a two tailed t-test performed at each of the VOIs, with a noncorrected p-value (alpha = 0.05). All brain regions with a positive T score, corresponding to a relevant increase in brain activity, and $p < 0.05$ were analyzed further. These brain region SUVs are reported below along with respective T scores and p-values. Due to the use of a single subject, no CT transformation based image attenuation correction was performed on the PET scan results.

Day	Condition	Parameters
1: Day 0	Baseline, DBS OFF	No DBS
2: Day 2	Condition 1, DBS ON	Contact 7 at 0.9 mA, 20 Hz
3: Day 7	Condition 2, DBS ON	Contact 4 at 1.2 mA, 20 Hz

Table 6. DBS Conditions during each PET scan.

4.4 Results

Accurate prediction of therapeutic outcomes by computational neuron models of DBS targeting the MLR of the brainstem will have strong clinical value for freezing of gait in Parkinson's disease patients with these implants [186]. Two major challenges remain in rendering these computational models more predictive in power: (1) making them subject specific, and (2) calibrating the model parameters. This work provides a framework to address both challenges using a combination of structural imaging at high magnetic fields, stimulus-evoked behavior using a monopolar review, and functional imaging.

4.4.1 Conductivity Anisotropy

A subject-specific model was created for Monkey L, but the conductivity, fractional anisotropy, diffusion tensors, and conductivity distributions were analyzed for both Monkeys L and P. Fractional anisotropy measured the difference between the three eigenvalues of the diffusion tensor [236]. If the diffusion was isotropic (all three eigenvalues are equal), this value became 0. If a large number was calculated, there was high diffusion anisotropy. These values were scaled between 0 (isotropic) and 1 (anisotropic) and displayed as black and white, respectively (Figure 20c). In the brainstem region of Monkey L and Monkey P, the fractional anisotropy was found to be highly variable, with values ranging from less than 0.1–0.7. Since the voxel size of the DTI was 1 mm isotropic, each voxel could be composed of multiple fiber tracts, explaining this variability. The highest fractional anisotropy values (~0.5–0.7 in Monkey L, ~0.3–0.7 in Monkey P), appeared to correspond to areas of the superior cerebellar peduncle (caudal of the decussation) as well as the medial lemniscus, two of the largest pathways in the brainstem. However, the fractional anisotropy values for the selected slices in Figure 20c at the decussation of SCP were small (Monkey L: 0.295, 0.224,

Monkey P: 0.181, 0.278, 0.268) and did not vary much from the mean of the surrounding voxels (Monkey L: 0.2867 ± 0.0752, Monkey P: 0.2575 ± 0.0504).

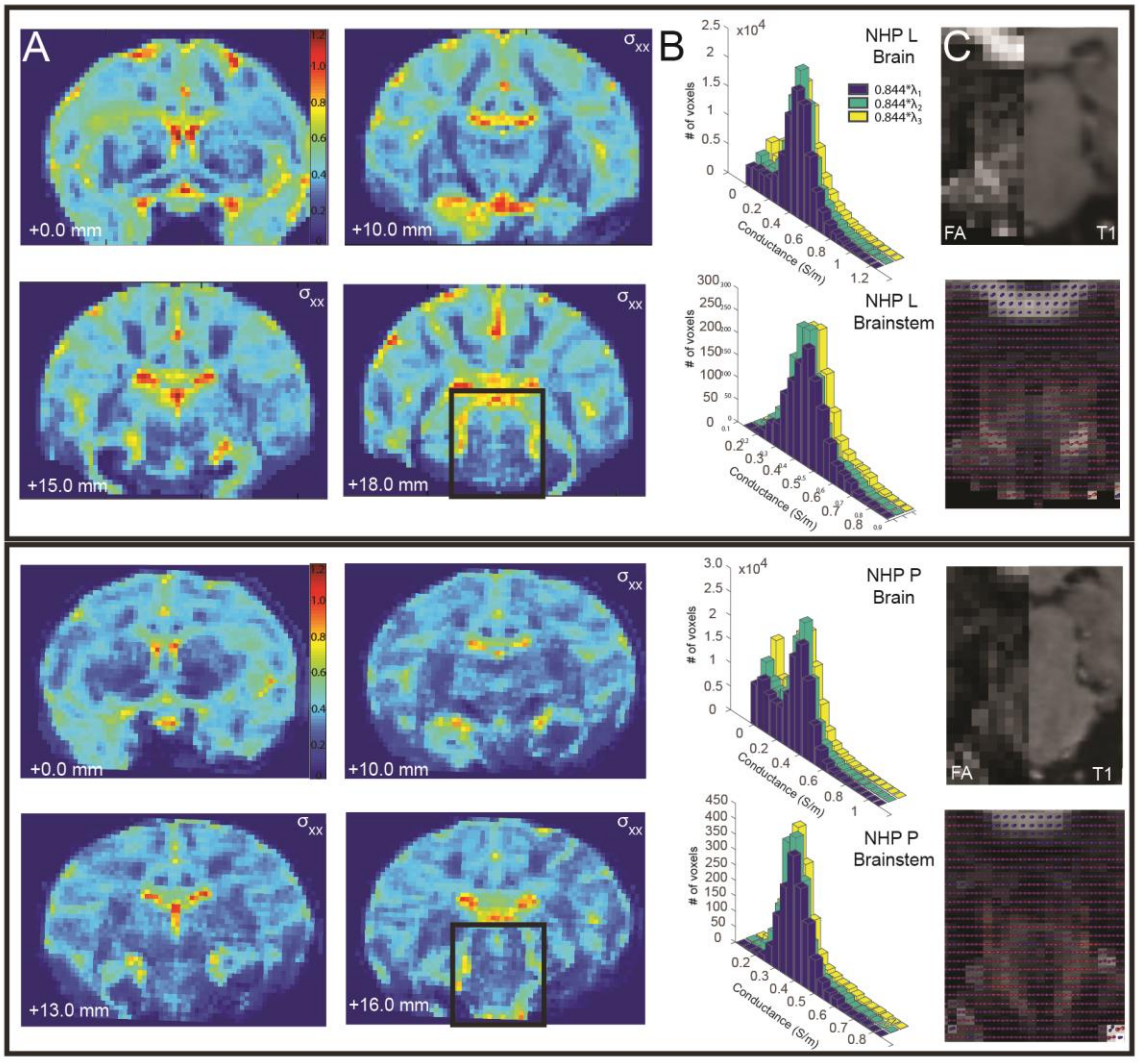

Figure 20. Comparison of conductivity and diffusion tensors between Monkey L (top) and Monkey P (bottom).
(A) The calculated conductivity, σ_{xx}, is shown for select coronal slices. (B) The distribution of conductivity values calculated from the primary, secondary, and tertiary eigenvalues for the entire brain (top) and the segmented brainstem (bottom. (C) The fractional anisotropy for a select brainstem slice (left), compared to a corresponding T1 slice (right). The diffusion tensors are plotted as spherical functions and overlaid on the fractional anisotropy. The orientations (dorsal-caudal, anterior-posterior, medial-lateral) are represented as RGB color components (i.e., R, G, and B, respectively).

All six parameters of the diffusion tensor are visualized as spherical functions in Figure 20c. In both Monkey L and Monkey P, the greatest difference in the overall tensor direction in the brainstem was seen in the area of the ML, where the tensors were primarily dorsal-caudal and were oriented at a 45 degree angle from the surrounding voxels. Additionally, the principal direction (V1) at the decussation of the SCP was oriented medial-lateral, with a 90◦ difference compared to the neighboring voxels. When comparing neighboring voxels elsewhere in the brainstem, many midline voxels displayed at least a 45◦ difference in the longest axis. While some variability between animals was expected, the overall anisotropy in the brainstem was comparable.

Given that the brainstem was composed of a heterogeneous set of nuclei and fiber tracts, we hypothesized that an FEM of the brainstem with anisotropic conductivity would exhibit strong asymmetries in comparison to an otherwise equivalent isotropic model. The conductivity values, σ_{xx}, derived from the subject-specific imaging are shown in Figure 20a for several coronal sections throughout the brain. Histograms of the conductivity values calculated from the primary, secondary and tertiary eigenvalues were given for the entire brain, including ventricles, and for the brainstem region around the DBS lead (Figure 20b). This region included the pons and part of the midbrain, demarcated as posterior of the substantia nigra. The average calculated conductivity along the main axes in the brainstem was between 0.3235 and 0.4018, just above 0.3 S/m, the value used for the isotropic models.

When conductivity anisotropy was incorporated into the models, the spread of current in the tissue was altered. As seen in Figure 19d, the isosurfaces of the electric potential in the isotropic model were spherical, while the isosurfaces in the anisotropic model were non-spherical. This is consistent with previous modeling studies that incorporated anisotropy [237]. Model predictions for activation threshold were much lower for anisotropic models than for the isotropic model. For example, the threshold for activating 5% of CTG axons using contact 7 was 0.5 mA for the anisotropic model and 1.1 mA for the isotropic model.

The conductivity scaling factor (s) has been previously reported as the range of s = 0.844 ± 0.0545 S·s/mm3 [227] with varying scaling factors used in other modeling studies [238], [239]. To investigate model sensitivity to the conductivity scaling factor within the reported range, activation threshold curves were generated using three values for s (0.79, 0.844, and 0.89). These results are shown in the second column for the ON (Figure 21), SCP (Figure 22), and CTG (Figure 23) tracts assuming an 8µm diameter axonal fiber for ON and a 2µm diameter for CTG and SCP. Varying the scaling factor ±6.5% resulted in only a minor shift (0.0981 mA) in the threshold for 5% activation of ON fibers using contact 7.

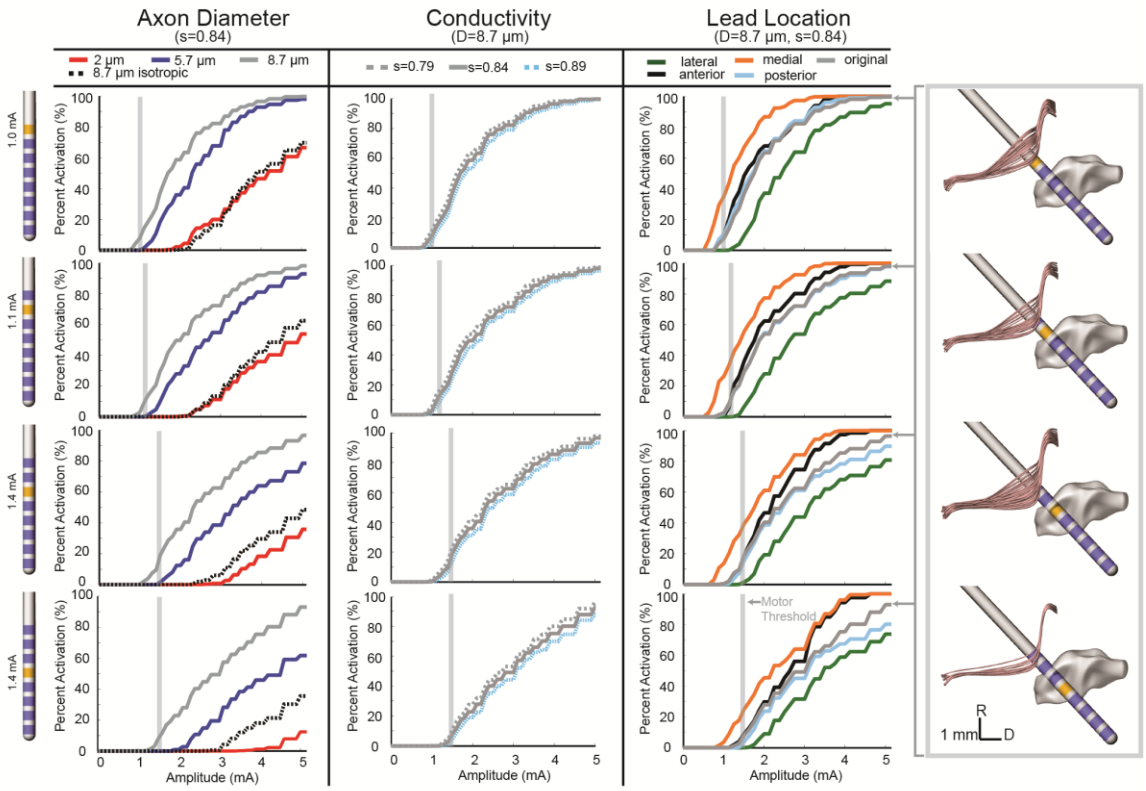

Figure 21. Model-predicted activation of the ON fiber tract.
Percent activation is plotted for each stimulation amplitude. Each column shows the variability of model predictions when changing axon diameter, conductivity scaling factor (s), and lead location. (Right) The axons activated at the motor threshold current for each contact are plotted.

4.4.2 Model Parameter Sweep

In addition to investigating model sensitivity to tissue conductivity, other model parameters known to impact the calculation of activation thresholds such as axon

diameter [240] and precise lead location were investigated as well. Previous models of axons in the brainstem region (SCP, ML, LL) were modeled with a diameter of 2µm [186]. While this is a conservative estimation for SCP and CTG axonal diameters, we also examined the effects on activation thresholds when using 5.7 and 8.7µm axon diameter, which may be more representative of actual axon diameters within the SCP [18] and CTG tracts. The ON tract was also modeled with 2, 5.7, and 8.7µm axon diameter with the latter thought to be the most realistic axon diameter. Atomic force microscopy has shown human ON fibers with much larger diameter fibers, between 10 and 15µm [241], which presumably would be slightly smaller in the rhesus macaque. Consistent with the principles of cable models of myelinated axons, the axonal diameter had a large effect on the resultant activation thresholds for all three fiber tracts (Figure 21-Figure 23).

Model sensitivity to the precise position of the DBS lead within the brainstem was investigated by shifting the lead in four directions. Using the same implantation angle as defined by the SWI/CT co-registration process and histological reconstructions from Monkey L, the DBS lead was shifted 0.5 mm anterior, poster, medial, and lateral of the original lead placement (chamber reference). Moving the lead medially increased ON activation, while moving the lead laterally decreased ON activation. At the threshold for contact 7 (1 mA), the model predicted a 27.5% increase in ON activation for a medial lead location. Overall, anterior and posterior deviation in lead location did not alter the model results for amplitudes near the threshold. Predicted activation from stimulation through contact 5 at 1.4 mA only decreased by 0.7% when the lead was moved in the anterior direction (Figure 21).

For contacts 5, 6, and 7, SCP activation increased when the lead position was shifted medial and posterior, while an anterior and lateral lead position decreased activation. SCP activation at 0.9 mA through contact 7 increased the activation by 2.1% (from 0 to 2.1%) when moving the lead posterior. Contact 4 was embedded within SCP, so lead location had minimal effect on SCP activation at lower amplitudes (below 2 mA). However, for amplitudes above 2 mA, the anterior and lateral lead placements decreased activation and

the medial lead placement increased activation. For 0.9 mA stimulation through contact 4, change in SCP activation was negligible (~0.1%) (Figure 22).

Due to the anatomy of the CTG, the effect of lead location was different for each active contact. In the posterior direction, there was minimal change in activation for contacts 6 and 7. The same was true for contact 4, at stimulation amplitudes below 1.6 mA. Contact 5 stimulation produced lower activation with a posterior lead placement until stimulation amplitude increased beyond 2 mA, which resulted in a large increase in activation that exceeded the original lead placement results. For all contacts, lateral shift decreased activation and medial shift increased activation, but the magnitude of these changes in activation differed for each contact. For the CTG, moving the lead 0.5 mm medially increased tract activation by 8% when stimulating through Contact 7 at 0.9 mA and 2.6% when stimulating through Contact 4 (Figure 23).

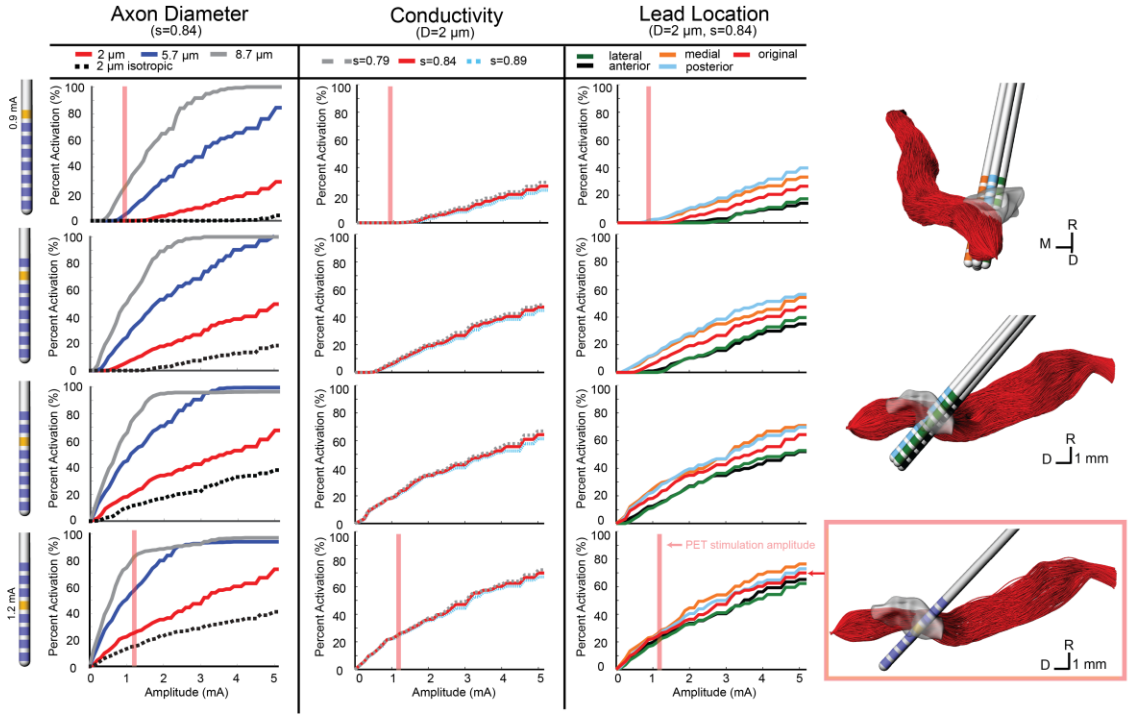

Figure 22. Model-predicted activation of the SCP fiber tract.
Percent activation is plotted for each stimulation amplitude. Each column shows the variability of model predictions when changing axon diameter, conductivity scaling factor (s), and lead location. (Right) The 0.5 mm lead displacement is shown in the context of the SCP axons. The axons activated at the PET stimulation amplitude for contact 4 (configuration 2) is shown.

4.4.3 Comparison of ON Model Simulations to Stimulus-Induced Eyelid Flutter

A monopolar review was conducted across all 8 contacts by applying a 20 Hz train of 90μs pulses in increasing amplitude at intervals of 0.1 mA until a motor side effect was observed or the amplitude of stimulation reached 3.5 mA. For the proximal four electrodes (contacts 4–7), a right eyelid flutter was observed at amplitudes at or above 1 mA (Table 5) with more proximal contacts requiring higher stimulation amplitudes. At 20 Hz stimulation, the therapeutic PPN-DBS stimulation frequency, stimulation resulted in an eyelid flutter, while stimulation at higher frequencies (e.g., 130 Hz) resulted in the eyelid remaining elevated. No other overt motor signs were observed at any of the stimulation amplitudes tested for other contacts.

The ON is known to project to the levator palpabrae superioris muscle of the eye, which is responsible for elevation of the upper eyelid [242]. Multi-compartment axon models were developed for the ON to identify model parameter settings that resulted in the most consistent activation values across the empirical motor threshold amplitude values as defined in Table 5. We assumed that the neuron models should predict an activation of 5–15% based on previous models of the corticospinal tract of internal capsule [223] at the experimental motor threshold. Using the ON computational model (diameter = 8.7μm, s = 0.844, original lead location), the percentage of activated axons at motor thresholds was calculated (Table 7). For each behavioral threshold, the percent error was calculated as the difference between the experimental threshold and the model-predicted stimulation amplitude necessary to activate 5% of the axons. There was no error in the model predictions for contact 5, 6, and 7. The percent error for contact 4 was 6.67%.

The neuron modeling results from the anisotropic model resulted in much lower activation thresholds than were predicted from the isotropic model. Moreover, the anisotropic models, in comparison to the isotropic models, resulted in activation thresholds that were more consistent with the thresholds for inducing eyelid flutter (Figure 21). For the isotropic models, there was 0% activation of ON at the threshold amplitude for all contacts. Using contact 5, a 5% activation of ON fibers was achieved at

1.25 mA for the anisotropic model, while the isotropic model required 3.4 mA to reach 5% activation. Similarly for contact 6, 1.1 mA activated 8.7% of the axons in the anisotropic model and 2.7 mA was required to activate 8.7% of the axons in the isotropic model. There were equivalent results for the SCP, where the anisotropic model predicted 26% of SCP axons activated at 1.2 mA through contact 4, while the isotropic model predicted 26% of SCP axons activated at 2.5 mA.

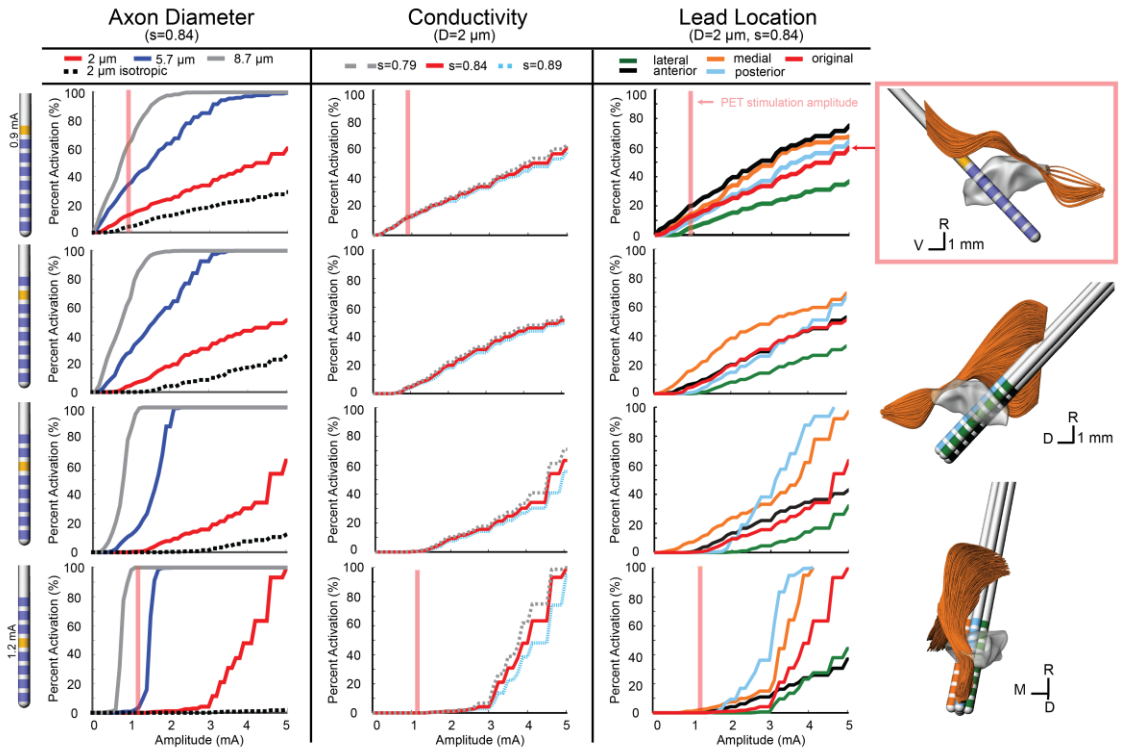

Figure 23. Model-predicted activation of the CTG fiber tract.
Percent activation is plotted for each stimulation amplitude. Each column shows the variability of model predictions when changing axon diameter, conductivity scaling factor (s), and lead location. (Right) The 0.5 mm lead displacement is shown in the context of the CTG axons. The axons activated at the PET stimulation amplitude for contact 7 (configuration 1) is shown.

Behavioral thresholds	% Activated at motor threshold	% Error
C7 (1.0 mA)	7.7	0
C6 (1.1 mA)	8.7	0
C5 (1.4 mA)	9.7	0
C4 (1.4 mA)	2.9	6.67

Table 7. Comparison of ON model simulations to behavior thresholds.

4.4.4 Comparison of Model Simulations to PET Imaging

Two FDG-PET scans, in the context of DBS, were conducted to examine the effects of DBS in the PPN area, after 0.9 mA stimulation through Contact 7 (configuration 1) and 1.2 mA stimulation through Contact 4 (configuration 2) (Table 8, Table 9). These were compared to a baseline scan with no stimulation. A sampling of the resultant FDG standard uptake values (FDG-SUV) are shown in Figure 24. For the first stimulation configuration, the ventral posteromedial nucleus of thalamus (VPM), which is innervated by CTG [243], showed an increased FDG-SUV ($p = 0.023$). Further, descending projections of CTG project to the inferior olivary nuclei [243], which also showed an increased FDG-SUV in configuration 1 ($p = 0.033$). This corresponded to an activation of 12.2% of CTG fibers (Table 7). For configuration 2, the models predicted no activation of CTG; the PET measured a significant increase in FDG-SUV in the VPM ($p = 0.041$), but no significant increase in FDG-SUV in the inferior olivary complex ($p > 0.05$).

Similarly, regions that are innervated by projections from the PPN showed an increased FDG-SUV, including the centromedian nucleus of thalamus ($p = 0.037$) during configuration 1. Configuration 2 showed increased FDG-SUV in regions innervated by fiber pathways near PPN, including the rostral interstitial nucleus of the MLF and the interstitial nucleus of Cajal, which are innervated by MLF. Increased FDG-SUV in downstream targets of the PPN was also observed in configuration 2, including the GP, basal amygdala, peripeduncular nucleus, centromedian nucleus, and the STN. The PET results also showed an increase in FDG-SUV in the red nucleus for configuration 2. This was supported by the model predicted activation of the SCP tract for configuration 2, 25.10% (Table 10).

Region	*P Value*	*T Score*
CEREBELLUM		
(R) Gracile Lobule	0.044152	14.39561
(R) Simple Lobule	0.030392	20.93132
(R) Inferior semilunar lobule	0.036188	17.57284
THALAMUS		
(R) Centromedian Nucleus	0.036749	17.30426
(R) Ventral Posteromedial Nucleus (VPM)	0.022568	28.1971
BRAINSTEM NUCLEI		
(R) Interstitial nucleus of the vestibular nerve	0.019187	33.16989
(R) Deep mesencephalic Nucleus	0.031026	20.50234
(R) Inferior Olivary Complex	0.032988	19.28151
(R) Lateral Vestibular Nucleus	0.041787	15.21301
(R) Abducens Nucleus	0.03823	16.63219
(R) Spinal Trigeminal Nucleus – Caudal Part	0.04019	15.81927
(R) Nucleus of the Bulbar Accessory Nerve	0.041015	15.50001
GYRI		
(R) Lingual gyrus	0.020319	31.32051
(L) Lingual Gyrus	0.047783	13.29825
(L) Inferior occipital Gyrus	0.035827	17.75039

Table 8. PET Configuration 1.

Region	*P Value*	*T Score*
CEREBELLUM		
(R) Lobule III	0.021944	28.99922
(L) Lobule III	0.027236	23.36013
(R) Flocculus	0.04999	12.70883
THALAMUS		
(R) Metathalamus	0.017863	35.62996
(R) Posterior Intralaminar Group	0.020822	30.56362
(L) Oral Pulvinar Nucleus	0.025265	25.18435

(R) Inferior Pulvinar Nucleus	0.029854	21.30901
(L) Ventral Posteromedial Nucleus – Parvicellular Part	0.04117	15.44166
BRAINSTEM NUCLEI		
(R) Inferior Colliculus	0.015676	40.60312
(L) Gigantocellular nuclei	0.027296	23.30846
(L) Rostral Interstitial Nucleus of the Medial Longitudinal Fasciculus	0.029331	21.68953
(R) Peripeduncular Nucleus	0.034083	18.6606
(R) Rostral Interstitial Nucleus of the Medial Longitudinal Fasciciulus	0.037915	16.77087
(L) Trochlear Nucleus	0.040337	15.76126
(R) Red Nucleus – Parvocellular Part	0.040367	15.74982
(L) Brachium of the Superior Colliculus	0.0446	14.25069
(L) Central Gray of the Midbrain	0.045313	14.02564
(L) Reticulotegmental Nucleus	0.046358	13.7083
(L) Interstitial Nucleus of Cajal	0.048904	12.99217
(L) Red Nucleus – Magnocellular Part	0.048722	13.04081
(R) Retrorubral Field	0.049879	12.73705
BASAL GANGLIA		
(R) Globus Pallidus, Internal (GPi)	0.016212	39.26104
(R) Globus Pallidus, External (GPe)	0.025203	25.24599
(R) Nucleus Accumbens	0.027752	22.92526
(L) Nucleus Accumbens	0.033671	18.88927
(L) Subthalamic Nucleus	0.045838	13.86446
GYRI		
(L) Medial Orbital Gyrus	0.025311	25.13825
(R) Posterior Parahippocampal Gyrus	0.038926	16.3343
(L) Straight Gyrus	0.043415	14.6409
(L) Isthmus of the Cingulate Gyrus	0.047395	13.40732
OTHER		
(R) Amygdala	0.018961	33.56495

(R) Basal Forebrain Nucleus	0.025798	24.66311
(L) Field H	0.029511	21.55704
(L) Field H2	0.041625	15.27233
(R) Prepiriform cortex	0.030997	20.52183
(R) Olfactory Tubercle	0.033287	19.10783
(L) Olfactory Tubercle	0.049761	12.76748
(R) Hippocampus	0.034665	18.34666
(R) Substantia Innominata	0.03942	16.12897
(R) Presubiculum	0.042929	14.80716
(L) Olfactory Bulb	0.044335	14.33593
(R) Claustrum	0.047654	13.33429
(R) Mammillotegmental Fasciculus	0.049034	12.99217

Table 9. PET Configuration 2.

PET DBS Settings	SCP % Activated	CTG % Activated
C7 (0.9 mA)	0	12.2
	-	-
	-	-
C4 (1.2 mA)	25.10	0

Table 10. Model comparison to behavior.

4.5 Discussion

Subject-specific computational models are an important tool to better understand the mechanisms of DBS in the brainstem and guide future DBS therapies [120], [154], [186], [223], [237], [244]. In order for these models to be clinically relevant they must provide accurate predictions. While other methods of validation have been applied to computational models of DBS, no models of the brainstem have yet been rendered subject specific. In this study, we evaluated the sensitivity of a subject-specific model of PPN-DBS in an NHP to different model parameters (tissue conductance anisotropy, axonal diameter, and DBS lead location) and compared the results to behavioral and functional imaging measures to determine the most accurate tissue conductance model.

Our previous computational models assumed the DBS lead was surrounded by homogeneous, isotropic tissue with a conductivity of 0.3 S/m [186]. Based on the fractional anisotropy results from Monkey L and Monkey P in the brainstem, the mean of

the image-based conductivity distribution did deviate from this isotropic conductivity assumption, but was well within an order of magnitude. Since the conductivity scaling factor did not greatly affect the model predictions, the spatial variability of the conductivity (i.e., the distribution of conductivities within the brainstem) proved to have a large effect on the potential distribution around the DBS lead. This high anisotropy near the lead resulted in lower stimulation amplitudes required to activate nearby axons despite the slightly higher average conductivity in the brainstem. Based on these results, it seems that anisotropy, in conjunction with the average conductivity, plays a role in the ability to activate axons.

Several other computational models of DBS have incorporated anisotropy of tissue conductivity, including models of STN DBS, which assigned typical conductivity values based on the literature [245], [246]. Other studies have converted fractional anisotropy measures from subject DTI to conductivity, including models of DBS in the STN region and in the thalamus [122], [237]. Similar to our models, regions with high anisotropy showed greater variability in the voltage isosurfaces and in the activated volume of tissue. However, these studies showed, contrary to our results, that the addition of anisotropy to the model decreased the percentage of axons activated. This difference may relate to axonal fiber orientations relative to the stimulated electrode(s) as well to assumptions of the neuron model parameters.

The PPN area, similar to other typical DBS target regions, is highly anisotropic. Indeed, the PPN is surrounded by the spinothalamic tract, CTG, ML, LL, and the MLF. The fibers of the SCP are intertwined with the cells of the PPN, which introduces challenges when attempting to stimulate one pathway over another. The present study showed that the inclusion of anisotropic conductivity is highly important for computational model predictions. This finding suggests that efforts to increase the resolution of fractional anisotropy imaging within the brainstem—through high-field, high angular resolution diffusion imaging [175], customized head coils [187], and advanced computational reconstruction algorithms [247] as used in this study—could have significant merit [159], [161], [170], [174], [176], [179].

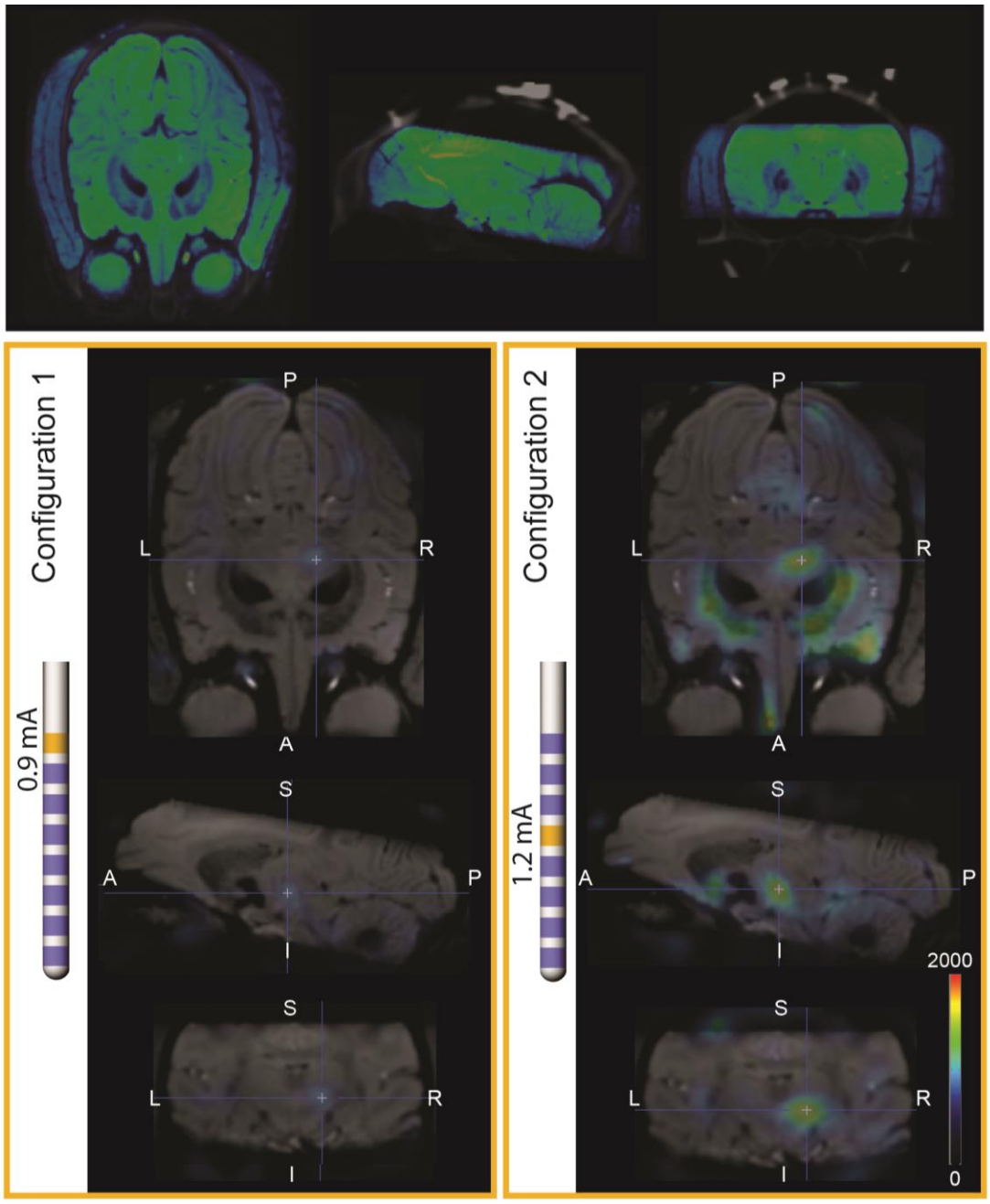

Figure 24. PET imaging during PPN-DBS.
(Top) Co-registration of SWI and baseline PET/CT images. The SWI is shown in blue-green cold scale for differentiation from the gray CT. (Left) FDG-SUV during PET configuration 1 (0.9 mA stimulation through contact 7), normalized to OFF-DBS. The PET results are overlaid on SWI of Monkey L. (Right) FDG-SUV during PET configuration 2 (1.2 mA stimulation through contact 4), normalized to OFF-DBS.

The clinical value of computational models lies in their legitimacy, making validation extremely important. Previous studies have confirmed the validity of their model parameters based upon correlations between EMG thresholds and activation of the corticospinal tract of internal capsule (during STN-DBS) [223], [239], between paresthesia thresholds and activation of the somatosensory representation of thalamus (ventral intermediate nucleus of thalamus) [248], and between conjugate eye deviation and ON activation (during STN-DBS) [239]. Here we extend this approach to the brainstem in the context of DBS targeting the PPN area. The results showed much better predictions of the activation of the ON axons at stimulation amplitudes necessary to induce eyelid flutter for the anisotropic models. Without being able to measure the magnitude of the eyelid twitch or obtain verbal feedback on the strength of the side effect, this is a positive result. Additional modifications to the model equations, more precise anatomical geometry, and higher resolution DTI could provide more accurate results. The assumption that the conductivity is linearly related to the diffusion tensor eigenvalues may not hold for high resolution (1 mm voxels) DTI within the brainstem and could also be a source of error in the models.

In this study, PET imaging was used as a gross measure of the activation in the area during stimulation to compare the effects of stimulation through different contacts to baseline. PET is a valuable tool that has been used to examine the effects of DBS [249], [250]. The use of PET in the context of PPN-DBS provided a novel approach to further evaluate the predictive capabilities of the computational neuron models. While the results were consistent, there are several limitations that should be noted. In addition to having only one subject, there was only one scan taken of each configuration (OFF DBS, C4 stimulation, C7 stimulation). Additional small spatial errors could also have been introduced when aligning the INIA19 atlas to the PET/CT. Furthermore, the PET analysis reported here did not account for the precise time from injection to time of scan. This will be incorporated in future studies for more accurate results.

Future studies will also need a larger sample size and expand the model validation methods. Through studies in NHPs, the addition of electrophysiology would provide

more insight into the effects of stimulation. The electrophysiological activation thresholds could be compared to the model predictions by recording single-unit spike activity at multiple sites within upstream and downstream targets of fiber pathways coursing near the PPN.

As DBS techniques continue to advance, new targets are being explored and new lead designs are being developed. There is a growing need for validated computational models to better understand the therapeutic results and titrate stimulation parameters in human patients implanted with DBS systems. This study is the first case of incorporating anisotropic conductivity into subject-specific computational models of DBS in the brainstem. Moreover, the study emphasizes how coupling behavioral metrics and functional imaging data in computational modeling studies can be critical for enhancing the predictive power of the models.

4.6 Acknowledgements

We thank the Center for Magnetic Resonance Research (CMRR) for providing the imaging resources, specifically Bud Grossman of the University of Minnesota Medical School for the use of PMOD. We also thank the Minnesota Supercomputing Institute for providing the computational resources to complete this study. This work was supported by grants from the National Institutes of Health (R01 NS081118, R01 NS085188, P41 EB015894, P30 NS076408, Human Connectome Project, U54 MH091657), the Michael J. Fox Foundation and the National Science Foundation (IGERT DGE 1069104 to LZ and GRFP 00006595 to BT).

5 Conclusions and Future Directions

Gait and balance difficulties are debilitating symptoms of Parkinson's disease, causing frequent falls, injuries, and hospitalization. These symptoms are sometimes not adequately addressed with either medication or traditional targets of DBS, including the STN and GP. DBS in the MLR may help these symptoms, but better understanding of stimulation in the brainstem is necessary. This thesis developed tools that were necessary for the study of DBS in the brainstem, including imaging tools to better visualize structures in the brainstem and accurate subject-specific computational models of PPN DBS to better understand the effects of stimulation both prospectively (Appendix I) and retrospectively (Appendix IV).

5.1 Brainstem Imaging

Improved visualization of brainstem structures is critical for both targeting accuracy and accurate subject-specific computational models. Current imaging sequences, especially those used in the clinic, show minimal differences in contrast in the brainstem, leading to challenges in the planning and verification of accurate DBS lead trajectories. This thesis identified the importance of using high field 7T imaging sequences, specifically SWI, to visualize fiber tracts in the brainstem. Unfortunately, most clinics only have access to 1.5T or 3T T1-W or T2-W, necessitating the use of other imaging tools to identify nuclei and fiber tracts in the brainstem. Better visualization of structures during DBS lead trajectory planning through the use of nonlinear warping algorithms or diffusion-weighted tractography allow for more consistent targeting and the ability to verify targeting with pre- or post-operative imaging.

While these imaging tools are extremely helpful, there is still room for improvement. For example, the nonlinear warping algorithm performed best when high resolution images were used. High field MRI, especially SWI, worked well because many internal structures, most notably fiber tracts, were visible through differences in contrast, such as differences between the PPN area and SCP, with the latter being more hypointense. This improved the 2D nonlinear warping algorithm because internal points of reference could be placed. The algorithm used these seed points to morph atlas slices to MRI slices and

render subject-specific geometry slices that were subsequently lofted into 3D structures. With lower resolution imaging and standard T1 and T2 clinical datasets this method produced less reliable results and was tedious due to the lack of contrast (Appendix IV). In the future, development of a software tool that allows for 3D warping of a brain atlas may be a quicker, more accurate approach in these cases. Brain structure volumes (.stl files) would be created from a standard brain atlas and be deformable in 3D. This deformation could take place in a virtual reality environment or on a desktop computer to match the atlas to the MRI volume. In 3D, warping would be based on the brain border and ventricles as well as easily identifiable internal structures. This tool would greatly benefit future clinical studies where DBS lead trajectory planning and computational modeling is necessary.

Structural imaging may never be able to truly demarcate the borders of PPN due to the interdigitation of PPN with SCP fibers and the fact that PPN is composed of multiple cell regions. For this reason, functional imaging, in conjunction with structural imaging, may be a useful tool to study the PPN area. This noninvasive tool allows for whole brain investigation of different gait conditions and the associated connections and brain network changes in both healthy and PD subjects. Movement artifacts during fMRI can be challenging with actual gait, but techniques such as imagined gait have been used successfully in previous studies [3], [251]. Advances to reduce voxel sizes and the use of higher field magnets to reduce the signal-to-noise ratio may be important for studying the brainstem area. Additional studies using PET with radioactive ligands specific to cholinergic, GABAergic, and glutamatergic synapses may be useful to understand the mechanisms of DBS in the brainstem and other interconnected structures. These studies could help elucidate differences between subjects who respond to treatment and those who do not, and guide the validation of computational modeling predictions.

5.2 Computational Models

Subject-specific computational models are an invaluable tool in identifying mechanisms of therapeutic or side effect inducing stimulation parameters. One of the most important parameters for the computational models was accuracy of the 3D geometry, as inaccurate

representations and locations of the nuclei and fiber tracts caused incorrect predictions. In addition to subject-specific geometry, the studies in this thesis showed that the inclusion of anisotropic neural tissue conductivity in the models was pertinent. However, even with the inclusion of anisotropic neural tissue conductivity, the models did not perfectly predict the behavioral effect. This may be due to the linear assumptions of the Tuch transformation between diffusion tensor eigenvalues and conductivity [227] or variability in diffusion weighted imaging sequence parameters. Additional modifications should be made to these models in the future to better reflect the conditions in vivo.

One modification would be to develop additional models of surrounding nuclei, as to represent the entire mesencephalic locomotor region. Studies have shown that stimulation in the cuneiform nucleus may provide the best therapy [74], and therefore its inclusion may be critical to the models. Additionally, imagined gait during microelectrode recordings in humans has revealed an increase in firing of the subcuneiform nucleus neurons [252]. Morphological and biophysical properties of the cuneiform and subcuneiform cells would need to be obtained prior to building accurate NEURON models. Some parameters from studies in cats, rats, and lampreys may be adapted for the development of NHP or human NEURON models. Two cell types could be modeled, as the cuneiform nucleus in cats is known to be composed of both GABAergic neurons and non-cholinergic neurons containing nitric oxide synthase –NADPH-diaphorase [253]. Camera lucida drawings of the two cell types in cats are available and would be used to develop the morphology of the cells [254]. Electrophysiologically, both cell types are characterized by a low-threshold L-type Ca^{2+} spike, according to studies done in lampreys [255], [256], and spontaneously fire at an average rate of 11 Hz in anesthetized rats [257]. Incorporating these parameters into the models could help determine whether the therapeutic region of activation is really in the cuneiform or PPN. Additionally, as more is discovered experimentally about the properties of PPN synapses, these could be incorporated into the model, similar to previous studies [107].

Another important aspect to consider in these models is the implication of PPN cell degeneration in advanced PD. This degeneration has even been shown to differ

depending not only on the level of dopaminergic degeneration [258] or the severity of the disease [2], but also on symptomology. For example, PD patients with balance deficits or falls have been shown to have significantly more degeneration of cholinergic PPN neurons than those without these symptoms [3]. Important for the NHP models, older MPTP-treated macaques have also been shown to have less cholinergic PPN cells than younger MPTP-treated macaques [3]. While reducing the number of cholinergic neurons in the models is trivial, the models also need to incorporate a measure of the axonal output before and after degeneration. These models would then be useful in predicting stimulation settings and lead placements that could maintain a tonic level of ACh in distal structures necessary for synapse function during progressive degeneration.

5.3 Towards preclinical and clinical trials

The computational models described in this thesis are useful for both preclinical and clinical trials of DBS. These trials are important for the validation of the PPN cell models and the degree to which the models can predict therapeutic stimulation settings. In order to distinguish these therapeutic regions, it is important to identify the key gait measurements necessary to differentiate the different aspects of gait. This will be needed to assess the resultant changes associated with stimulation.

5.3.1 Gait Data Collection

To demonstrate proof-of-concept, the computational models were used to guide implantation trajectory and stimulation settings in one NHP. After implantation, gait kinematics for Monkey L (Appendix I) were collected during three states: normal, parkinsonian, and PPN DBS to evaluate the therapeutic effects of PPN DBS. While the experiment revealed noticeable difference in observable and quantifiable gait measures between the normal and parkinsonian states, gait analysis of PPN DBS in the NHP revealed no therapeutic benefits for gait. There are many possible causes for this outcome, including the inability of current data collection and analysis methods to quantify the subtle and complex changes in gait. In this case, freezing of gait was not observed; however, the treadmill may have served as a cue similar to visual and auditory cues used in physical therapy treatments for freezing of gait [259]. Future experimental

studies of PPN DBS in the NHP will need to incorporate a better method for the evaluation of PD gait and the effects of DBS therapy. Based on the outcomes from the treadmill study, a habitrail enclosure is now being built to facilitate voluntary movement instead of cued movement. This plastic enclosure will feature a tunnel with two retrieval areas on each end. Food will be manually placed in one end of the enclosure to entice movement in one direction, and then placed in the opposite end to monitor turning and moving in the other direction. Motion capture cameras will surround the tunnel to collect joint positions over time for analysis of gait parameters, and force plates will be used to capture information such as changes in anticipatory postural adjustments. Tasks to measure postural control utilize a force plate to measure sway while standing, comparing eyes closed to eyes open. This may be adapted for use in the NHP model by measuring sway on a force plate with the lights on and off.

5.3.2 Changes to DBS Lead and Implantation Angle

As previously mentioned, another reason for lack of therapeutic benefit to gait in PPN DBS may be the lack of selective stimulation to the therapeutic region while avoiding side effect regions. While bipolar stimulation through the traditional four contact DBS lead can restrict the stimulation region, a segmented electrode may be necessary due to the small size of the brainstem structures. Ideally this segmented electrode would also have a smaller diameter in order to lessen tissue damage. While it has been shown computationally that the segmented electrode may provide more selective stimulation for PPN [186], additional detailed analysis is needed.

Future studies may also experiment with different lead implant angles to achieve better placement and thus more therapeutic stimulation. An implantation trajectory similar to the trajectory used in auditory midbrain implants may improve lead location accuracy as well as reduce surgery complications. The current implantation trajectory implants the lead through a burr hole in the top of the head. The lead traverses lateral of the lateral ventricles all the way down to the brainstem, intersecting structures such as the ventral lateral thalamic nucleus, centromedian thalamic nucleus, red nucleus, or substantia nigra, depending on the trajectory. This could potentially cause damage to these areas, some of

which contain axonal outputs of PPN, possibly negating some of the therapeutic effects of stimulation. This long trajectory also increases the risk of intracranial hematoma [260]. The auditory midbrain implants use a lateral suboccipital approach while the patient is in a semi-seated position, performing a craniotomy on the lower back of the head and allowing the cerebellum to retract until the inferior colliculus is visible [261]. This would be a shorter lead trajectory, possibly allowing for less error. This method is not without its challenges. Since the PPN is caudal of the inferior colliculus, the lead would still have to traverse through the inferior colliculus and cuneiform nucleus to reach PPN. Complications from this trajectory may include auditory side effects, while the trajectory through the cuneiform nucleus may be beneficial.

5.3.3 Understanding the Mechanisms of Gait and Balance

Ultimately, in order to improve DBS therapy for gait and balance there is a need to better understand the function of the cell types within MLR in relation to locomotion and Parkinson's disease symptoms. New tools such as optogenetics could be crucial to this discovery. Currently, cholinergic brainstem neurons can be studied in mice that express Channelrhodopsin-2 (ChR2) conjugated to yellow fluorescent protein (YFP) under the choline acetyltransferase (ChAT) promoter. Studies have been completed to establish the role of cholinergic brainstem neurons in REM sleep [262]. Additionally, optogenetics has been used to study the role of glutamatergic neurons in central pattern generators, finding that glutamatergic neurons in the caudal hindbrain of mice were responsible for initiating and maintaining gait rhythm [263]. The vesicular glutamate transporter 2-ChR2-YFP was used in mice to express ChR2 in glutamatergic neurons in both the hindbrain and the spinal cord. The study found that activation of glutamatergic reticulospinal neurons in the hindbrain was sufficient to activate the spinal locomotor network.

Another study used optogenetics to dissect locomotor functions of the glutamatergic, GABAergic, and cholinergic neurons in the MLR in mice [264]. Glutamatergic and GABAergic neurons were transduced with a Cre-inducible virus expressing ChR2-YFP into vGLUT2-Cre or vGAT-Cre mice, while cholinergic neurons were labeled in transgenic mice expressing ChR2-YFP under the ChAT promotor. Different cell types

were optically stimulated during locomotion to determine their effects. Stimulation of glutamatergic neurons was found to be necessary for locomotion, eliciting running at short latencies, while stimulation of GABAergic neurons caused deceleration. Cholinergic neurons were found to modulate locomotion, increasing speed during running, but were not able to initiate gait when the mouse was stopped. Due to the differences in connectivity between the PPN and the basal ganglia in different animals [151], additional studies in other animals may be necessary to elucidate the effects of stimulating different cell types in PPN in humans. This would help to discern the role each cell type plays in the control of posture as well as gait. Stimulation of separate cell types could be followed by stimulation of all cell types to tease out what happens during DBS when all cell types are being stimulated simultaneously.

5.3.4 Other Targets for Gait and Balance

These mechanistic studies may reveal the need to investigate the therapeutic effects of stimulation in other regions, including upstream structures connected to PPN. This includes the centromedian nucleus of thalamus, which may be an easier target for DBS. One study showed that, in a few PD patients, DBS in the centromedian-parafascicular nucleus complex improved freezing based on UPDRS scores [265]. Additional studies are needed to better understand the pathways that are being activated, as this region is also being targeted for Tourette's syndrome, epilepsy, and minimally conscious state after traumatic brain injury [266]–[269]. Other upstream targets include the STN and GPi. A handful of small clinical trials have evaluated the effects of STN and GPi DBS on gait in PD patients and found that in some cases therapeutic effects can be elicited for gait parameters and standing postural control. It should be noted, however, that these effects seem to decrease with time [87], [270]. These studies suggest that STN and GPi stimulation may be most therapeutic for gait and standing postural control problems, while PPN stimulation may be most therapeutic for dynamic postural control problems [14]. STN DBS seemed more likely to aggravate dynamic postural control, while GPi DBS had negligible effects. Descending targets of PPN may also be experimentally tested in animal models for their effects on gait, including the reticulo-spinal pathway. In the

end, combined stimulation between another target and PPN may be necessary for a significant and consistent therapeutic effect.

5.3.5 Improving Clinical Trials

Based on the literature, it is difficult to ascertain the optimal DBS therapy strategy for treatment of gait and balance symptoms of PD. This thesis provides important tools to strategically target the brainstem and better understand the mechanisms of DBS in the brainstem. The imaging tools and computational models described in this thesis could be utilized in pre-operative planning to aid in the electrode placement and post-operative analysis to choose stimulation settings, improving the chances of obtaining a therapeutic response [224], [244]. Appendix IV describes a post-operative clinical application of the models. With the acquisition of pre-operative MRI for anatomy and post-operative MRI for lead location, subject-specific models were created to determine what nuclei or pathways were being activated during therapeutic stimulation. Therefore, these models could be very useful in clinical trials of DBS going forward. Not only as a pre-operative approach to guide DBS lead trajectory and stimulation settings, but to post-operatively evaluate and understand the effects of both therapeutic and side effect inducing stimulation. When evaluating new targets of DBS such as PPN it may be beneficial to run a smaller clinical trial initially, using the models for both pre-operative planning and post-operative analysis to study the effects of stimulation in depth before running a large pivotal trial.

In addition to the incorporation of computational modeling, there are many other factors that could improve clinical trials and create more impactful studies. When targeting the PPN, the best strategy would be to begin with the collection of high resolution MRI and DWI. This would assist in trajectory planning to avoid stimulating side-effect producing fiber tracts lateral and medial of PPN. In addition to avoiding side effects, the lead must be placed within the MLR to optimize therapy. The correct placement for therapy is unknown since studies to date that have reported therapy lacked reports of specific lead placement. However, the optimal location may be postulated based upon the knowledge of the roles each cell type within PPN plays with regards to gait. Based on decerebrate cat

and optogenetic mice studies, it may be necessary to target the PPNd in order to activate glutamatergic neurons. Stimulation in this area could also target a portion of the remaining cholinergic neurons as well. The glutamatergic neurons may be the most promising target as they are shown in both cats and mice to be involved in the initiation of gait, necessary to provide therapy for freezing of gait. Cholinergic neurons, while able to modulate locomotion, are not able to initiate gait [264].

Collection of high resolution structural imaging would also help with the development of subject-specific computational models. Most importantly, post-implant reporting of lead location should be as accurate as possible to determine the sites of stimulation. To determine the optimal site, additional methods of measuring therapy beyond the traditional UPDRS scores must be used. These tests do not seem to be able to capture the complexities of gait modulation. A trial would ideally be done in patients who were already implanted in STN or GPi and developed gait symptoms resistant to levodopa and stimulation. This study, which in combination with the computational models developed in this thesis, would allow for a comparison between the effects of STN or GPi stimulation, PPN stimulation, and combined stimulation on gait and balance symptoms.

Overall, there is much still to be explored within the world of parkinsonian gait and balance symptoms and PPN DBS. It seems there may be no one size fits all clinical trial for DBS as some patients inevitably do well while others inexplicably do not. However, the use of these imaging and computational tools along with strict patient criteria, accurate reporting of lead locations and detailed kinematic analysis is needed to truly tease out the therapeutic region for treating parkinsonian gait and postural control.

References

[1] H. Braak, E. Ghebremedhin, U. Rub, H. Bratzke, and K. Del Tredici, "Stages in the development of Parkinson's disease-related pathology," *Cell Tissue Res*, vol. 318, no. 1, pp. 121–34, Oct. 2004.

[2] J. O. Rinne, S. Y. Ma, M. S. Lee, Y. Collan, and M. Röyttä, "Loss of cholinergic neurons in the pedunculopontine nucleus in Parkinson's disease is related to disability of the patients," *Park. Relat Disord*, vol. 14, no. 7, pp. 553–557, 2008.

[3] C. Karachi, D. Grabli, F. A. Bernard, D. Tandé, N. Wattiez, H. Belaid, E. Bardinet, A. Prigent, H.-P. Nothacker, S. Hunot, A. Hartmann, S. Lehéricy, E. C. Hirsch, and C. François, "Cholinergic mesencephalic neurons are involved in gait and postural disorders in Parkinson disease," *J. Clin. Invest.*, vol. 120, no. 8, pp. 2745–2754, 2010.

[4] P. A. Pahapill and A. M. Lozano, "The pedunculopontine nucleus and Parkinson's disease," *Brain*, vol. 123, no. 9, pp. 1767–83, Sep. 2000.

[5] M. L. T. M. Müller, R. L. Albin, V. Kotagal, R. A. Koeppe, P. J. H. Scott, K. A. Frey, and N. I. Bohnen, "Thalamic cholinergic innervation and postural sensory integration function in Parkinson's disease," *Brain*, vol. 136, no. 11, pp. 3282–3289, Nov. 2013.

[6] M. Rizzone, M. Ferrarin, A. Pedotti, B. Bergamasco, E. Bosticco, M. Lanotte, P. Perozzo, A. Tavella, E. Torre, M. Recalcati, A. Melcarne, and L. Lopiano, "High-frequency electrical stimulation of the subthalamic nucleus in Parkinson's disease: kinetic and kinematic gait analysis," *Neurol Sci*, vol. 23 Suppl 2, pp. S103–4, Sep. 2002.

[7] M. Ferrarin, L. Lopiano, M. Rizzone, M. Lanotte, B. Bergamasco, M. Recalcati, and A. Pedotti, "Quantitative analysis of gait in Parkinson's disease: a pilot study on the effects of bilateral sub-thalamic stimulation," *Gait Posture*, vol. 16, no. 2, pp. 135–48, 2002.

[8] M. Faist, J. Xie, D. Kurz, W. Berger, C. Maurer, P. Pollak, and C. H. Lucking, "Effect of bilateral subthalamic nucleus stimulation on gait in Parkinson's disease," *Brain*, vol. 124, no. Pt 8, pp. 1590–600, Aug. 2001.

[9] N. Allert, J. Volkmann, S. Dotse, H. Hefter, V. Sturm, and H. J. Freund, "Effects of bilateral pallidal or subthalamic stimulation on gait in advanced Parkinson's disease," *Mov. Disord.*, vol. 16, no. 6, pp. 1076–85, 2001.

[10] J. Xie, P. Krack, A. L. Benabid, and P. Pollak, "Effect of bilateral subthalamic nucleus stimulation on parkinsonian gait," *J. Neurol.*, vol. 248, no. 12, pp. 1068–72, 2001.

[11] M. Pötter-Nerger and J. Volkmann, "Deep brain stimulation for gait and postural symptoms in Parkinson's disease," *Mov. Disord.*, vol. 28, no. 11, pp. 1609–1615, Sep. 2013.

[12] B. F. L. van Nuenen, R. A. J. Esselink, M. Munneke, J. D. Speelman, T. van Laar, and B. R. Bloem, "Postoperative gait deterioration after bilateral subthalamic nucleus stimulation in Parkinson's disease," *Mov. Disord. Off. J. Mov. Disord. Soc.*, vol. 23, no. 16, pp. 2404–2406, Dec. 2008.

[13] C. Moreau, L. Defebvre, A. Destée, S. Bleuse, F. Clement, J. L. Blatt, P. Krystkowiak, and D. Devos, "STN-DBS frequency effects on freezing of gait in advanced Parkinson disease," *Neurology*, vol. 71, no. 2, pp. 80–84, Jul. 2008.
[14] A. Collomb-Clerc and M.-L. Welter, "Effects of deep brain stimulation on balance and gait in patients with Parkinson's disease: A systematic neurophysiological review," *Neurophysiol. Clin. Clin. Neurophysiol.*, vol. 45, no. 4–5, pp. 371–388, Nov. 2015.
[15] M.-P. Fournier-Gosselin, N. Lipsman, J. A. Saint-Cyr, C. Hamani, and A. M. Lozano, "Regional anatomy of the pedunculopontine nucleus: Relevance for deep brain stimulation," *Mov. Disord.*, vol. 28, no. 10, pp. 1330–1336, 2013.
[16] G. X. Huang Paxinos, *Atlas of the Human Brainstem*. San Diego: Academic Press, 1995.
[17] G. Paxinos and C. Watson, *The Rat Brain in Stereotaxic Coordinates*. Academic Press, 1998.
[18] L. N. Hazrati and A. Parent, "Projection from the deep cerebellar nuclei to the pedunculopontine nucleus in the squirrel monkey," *Brain Res*, vol. 585, no. 1–2, pp. 267–71, Jul. 1992.
[19] A. Machado and K. B. Baker, "Upside Down Crossed Cerebellar Diaschisis: Proposing Chronic Stimulation of the Dentatothalamocortical Pathway for Post-Stroke Motor Recovery," *Front. Integr. Neurosci.*, vol. 6, May 2012.
[20] C. Rubio, V. Custodio, F. Juárez, and C. Paz, "Stimulation of the superior cerebellar peduncle during the development of amygdaloid kindling in rats," *Brain Res*, vol. 1010, no. 1–2, pp. 151–155, 2004.
[21] P. W. Nathan and M. C. Smith, "The rubrospinal and central tegmental tracts in man," *Brain*, vol. 105, no. 0006–8950 (Print), pp. 223–69, 1982.
[22] W. J. C. Verhaart, "The central tegmental tract," *J. Comp. Neurol.*, vol. 90, no. 2, pp. 173–192, Apr. 1949.
[23] J. Bebin, "The central tegmental bundle. An anatomical and experimental study in the monkey," *J. Comp. Neurol.*, vol. 105, no. 2, pp. 287–332, Sep. 1956.
[24] J. A. Simpson and W. Fitch, *Applied Neurophysiology: With Particular Reference to Anaesthesia*. Butterworth-Heinemann, 2013.
[25] D. Purves, G. J. Augustine, D. Fitzpatrick, L. C. Katz, A.-S. LaMantia, J. O. McNamara, and S. M. Williams, "The Major Afferent Pathway for Mechanosensory Information: The Dorsal Column-Medial Lemniscus System," 2001.
[26] B. Lavoie and A. Parent, "Pedunculopontine nucleus in the squirrel monkey: distribution of cholinergic and monoaminergic neurons in the mesopontine tegmentum with evidence for the presence of glutamate in cholinergic neurons," *J Comp Neurol*, vol. 344, no. 2, pp. 190–209, Jun. 1994.
[27] B. E. Jones and A. Beaudet, "Distribution of acetylcholine and catecholamine neurons in the cat brainstem: A choline acetyltransferase and tyrosine hydroxylase immunohistochemical study," *J. Comp. Neurol.*, vol. 261, no. 1, pp. 15–32, Jul. 1987.
[28] D. B. Rye, C. B. Saper, H. J. Lee, and B. H. Wainer, "Pedunculopontine tegmental nucleus of the rat: cytoarchitecture, cytochemistry and some extrapyramidal

connections of the mesopontine tegmentum," *J.Comp.Neurol.*, vol. 259, pp. 483–528, 1987.
[29] S. R. Vincent, K. Satoh, D. M. Armstrong, P. Panula, W. Vale, and H. C. Fibiger, "Neuropeptides and nadph-diaphorase activity in the ascending cholinergic reticular system of the rat," *Neuroscience*, vol. 17, no. 1, pp. 167–182, Jan. 1986.
[30] A. Charara and A. Parent, "Brainstem dopaminergic, cholinergic and serotoninergic afferents to the pallidum in the squirrel monkey," *Brain Res*, vol. 640, no. 1–2, pp. 155–70, Mar. 1994.
[31] J. Mena-Segovia, B. R. Micklem, R. G. Nair-Roberts, M. A. Ungless, and J. P. Bolam, "GABAergic neuron distribution in the pedunculopontine nucleus defines functional subterritories," *J. Comp. Neurol.*, vol. 515, no. 4, pp. 397–408, 2009.
[32] M.-M. Mesulam, C. Geula, M. A. Bothwell, and L. B. Hersh, "Human reticular formation: cholinergic neurons of the peduncolopontine and laterodorsal tegmental nuclei and some cytochemical comparisons to forebrain cholinergic neurons," *J.Comp.Neurol.*, vol. 283, pp. 611–633, 1989.
[33] K. F. Manaye, R. Zweig, D. Wu, L. B. Hersh, S. De Lacalle, C. B. Saper, and D. C. German, "Quantification of cholinergic and select non-cholinergic mesopontine neuronal populations in the human brain," *Neuroscience*, vol. 89, no. 3, pp. 759–770, Mar. 1999.
[34] N. I. Bohnen and R. L. Albin, "The cholinergic system and Parkinson disease," *Behav. Brain Res.*, vol. 221, no. 2, pp. 564–573, Aug. 2011.
[35] E. C. Hirsch, A. M. Graybiel, C. Duyckaerts, and F. Javoy-Agid, "Neuronal loss in the pedunculopontine tegmental nucleus in Parkinson disease and in progressive supranuclear palsy," *Proc. Natl. Acad. Sci.*, vol. 84, no. 16, pp. 5976–5980, Aug. 1987.
[36] K. Takakusaki, T. Shiroyama, T. Yamamoto, and S. T. Kitai, "Cholinergic and noncholinergic tegmental pedunculopontine projection neurons in rats revealed by intracellular labeling," *J Comp Neurol*, vol. 371, no. 3, pp. 345–61, 1996.
[37] M. Weinberger, C. Hamani, W. D. Hutchison, E. Moro, A. M. Lozano, and J. O. Dostrovsky, "Pedunculopontine nucleus microelectrode recordings in movement disorder patients," *Exp Brain Res*, vol. 188, no. 2, pp. 165–74, Jun. 2008.
[38] D. Pare, Y. Smith, A. Parent, and M. Steriade, "Projections of brainstem core cholinergic and non-cholinergic neurons of cat to intralaminar and reticular thalamic nuclei," *Neuroscience*, vol. 25, pp. 69–86, 1988.
[39] A. P. Strafella, A. M. Lozano, B. Ballanger, Y.-Y. Poon, A. E. Lang, and E. Moro, "rCBF changes associated with PPN stimulation in a patient with Parkinson's disease: A PET study," *Mov. Disord.*, vol. 23, no. 7, pp. 1051–1054, May 2008.
[40] B. Lavoie and A. Parent, "Pedunculopontine nucleus in the squirrel monkey: projections to the basal ganglia as revealed by anterograde tract-tracing methods," *J Comp Neurol*, vol. 344, no. 2, pp. 210–31, Jun. 1994.
[41] A. Charara, Y. Smith, and A. Parent, "Glutamatergic inputs from the pedunculopontine nucleus to midbrain dopaminergic neurons in primates: Phaseolus vulgaris-leucoagglutinin anterograde labeling combined with postembedding

glutamate and GABA immunohistochemistry," *J Comp Neurol*, vol. 364, no. 2, pp. 254–266, 1996.
[42] B. Lavoie and A. Parent, "Pedunculopontine nucleus in the squirrel monkey: cholinergic and glutamatergic projections to the substantia nigra," *J Comp Neurol*, vol. 344, no. 2, pp. 232–41, Jun. 1994.
[43] K. Nakano, Y. Hasegawa, A. Tokushige, S. Nakagawa, T. Kayahara, and N. Mizuno, "Topographical projections from the thalamus, subthalamic nucleus and pedunculopontine tegmental nucleus to the striatum in the Japanese monkey, Macaca fuscata," *Brain Res*, vol. 537, no. 1–2, pp. 54–68, 1990.
[44] C. Martinez-Gonzalez, J. P. Bolam, and J. Mena-Segovia, "Topographical Organization of the Pedunculopontine Nucleus," *Front. Neuroanat.*, vol. 5, Apr. 2011.
[45] E. Garcia-Rill, R. D. Skinner, H. Miyazato, and Y. Homma, "Pedunculopontine stimulation induces prolonged activation of pontine reticular neurons," *Neuroscience*, vol. 104, no. 2, pp. 455–465, 2001.
[46] K. Takakusaki, T. Habaguchi, J. Ohtinata-Sugimoto, K. Saitoh, and T. Sakamoto, "Basal ganglia efferents to the brainstem centers controlling postural muscle tone and locomotion: a new concept for understanding motor disorders in basal ganglia dysfunction," *Neuroscience*, vol. 119, no. 1, pp. 293–308, 2003.
[47] K. Takakusaki, K. Obara, T. Nozu, and T. Okumura, "Modulatory effects of the GABAergic basal ganglia neurons on the PPN and the muscle tone inhibitory system in cats," *Arch. Ital. Biol.*, vol. 149, no. 4, pp. 385–405, Dec. 2011.
[48] A.-S. Rolland, C. Karachi, M.-P. Muriel, E. C. Hirsch, and C. François, "Internal pallidum and substantia nigra control different parts of the mesopontine reticular formation in primate," *Mov. Disord. Off. J. Mov. Disord. Soc.*, vol. 26, no. 9, pp. 1648–1656, Aug. 2011.
[49] N. Galvez-Jimenez, *Scientific Basis for the Treatment of Parkinson's Disease, Second Edition*. CRC Press, 2013.
[50] E. Shink, M. Sidibe, and Y. Smith, "Efferent connections of the internal globus pallidus in the squirrel monkey: II. Topography and synaptic organization of pallidal efferents to the pedunculopontine nucleus," *J Comp Neurol*, vol. 382, no. 3, pp. 348–63, Jun. 1997.
[51] M. D. Johnson, J. Zhang, D. Ghosh, C. C. McIntyre, and J. L. Vitek, "Neural targets for relieving parkinsonian rigidity and bradykinesia with pallidal deep brain stimulation," *J Neurophysiol*, vol. 108, no. 2, pp. 567–77, Jul. 2012.
[52] H. J. W. Nauta and M. Cole, "Efferent projections of the subthalamic nucleus: an autoradiographic study in monkey and cat," *J.Comp.Neurol.*, vol. 180, pp. 1–16, 1978.
[53] J. A. Childs and K. Gale, "Neurochemical evidence for a nigrotegmental GABAergic projection," *Brain Res*, vol. 258, no. 1, pp. 109–114, 1983.
[54] A. F. Sadikot, A. Parent, and C. Francois, "Efferent connections of the centromedian and parafascicular thalamic nuclei in the squirrel monkey: a PHA-L study of subcortical projections," *J.Comp.Neurol.*, vol. 315, pp. 137–159, 1992.

[55] S. N. Haber, E. Lynd, C. Klein, and H. J. Groenewegen, “Topographic organization of the ventral striatal efferent projections in the rhesus monkey: An anterograde tracing study,” *J Comp Neurol*, vol. 293, no. 2, pp. 282–298, 1990.
[56] A. R. Granata and S. T. Kitai, “Inhibitory substantia nigra inputs to the pedunculopontine neurons,” *ExpBrain Res*, vol. 86, pp. 459–466, 1991.
[57] M. Matsumura, A. Nambu, Y. Yamaji, K. Watanabe, H. Imai, M. Inase, H. Tokuno, and M. Takada, “Organization of somatic motor inputs from the frontal lobe to the pedunculopontine tegmental nucleus in the macaque monkey,” *Neuroscience*, vol. 98, no. 1, pp. 97–110, 2000.
[58] B. R. Aravamuthan, J. A. McNab, K. L. Miller, M. Rushworth, N. Jenkinson, J. F. Stein, and T. Z. Aziz, “Cortical and subcortical connections within the pedunculopontine nucleus of the primate Macaca mulatta determined using probabilistic diffusion tractography,” *J. Clin. Neurosci.*, vol. 16, no. 3, pp. 413–420, 2009.
[59] B. W. Fling, R. G. Cohen, M. Mancini, S. D. Carpenter, D. A. Fair, J. G. Nutt, and F. B. Horak, “Functional Reorganization of the Locomotor Network in Parkinson Patients with Freezing of Gait,” *PLoS ONE*, vol. 9, no. 6, p. e100291, Jun. 2014.
[60] C. Karachi, A. André, E. Bertasi, E. Bardinet, S. Lehéricy, and F. A. Bernard, “Functional Parcellation of the Lateral Mesencephalus,” *J. Neurosci.*, vol. 32, no. 27, pp. 9396–9401, Jul. 2012.
[61] K. A. Muthusamy, B. R. Aravamuthan, M. L. Kringelbach, N. Jenkinson, N. L. Voets, H. Johansen-Berg, J. F. Stein, and T. Z. Aziz, “Connectivity of the human pedunculopontine nucleus region and diffusion tensor imaging in surgical targeting,” *J Neurosurg*, vol. 107, no. 4, pp. 814–820, 2007.
[62] P. M. Schweder, P. C. Hansen, A. L. Green, G. Quaghebeur, J. Stein, and T. Z. Aziz, “Connectivity of the pedunculopontine nucleus in parkinsonian freezing of gait,” *Neuroreport*, vol. 21, no. 14, pp. 914–916, 2010.
[63] E. Garcia-Rill, R. D. Skinner, and J. A. Fitzgerald, “Activity in the mesencephalic locomotor region during locomotion,” *Exp.Neurol.*, vol. 82, pp. 609–622, 1983.
[64] E. Garcia-Rill, C. R. Houser, R. D. Skinner, W. Smith, and D. J. Woodward, “Locomotion-inducing sites in the vicinity of the pedunculopontine nucleus,” *Brain Res Bull*, vol. 18, no. 6, pp. 731–8, Jun. 1987.
[65] E. Garcia-Rill and R. D. Skinner, “Modulation of rhythmic function in the posterior midbrain,” *Neuroscience*, vol. 27, no. 2, pp. 639–654, 1988.
[66] M. Matsumura, K. Watanabe, and C. Ohye, “Single-unit activity in the primate nucleus tegmenti pedunculopontinus related to voluntary arm movement,” *Neurosci Res*, vol. 28, no. 2, pp. 155–165, 1997.
[67] S. Fahn, Elton RL, and U. D. Committee, “Unified Parkinson’s Disease rating scale,” *Recent Dev. Park. Dis.*, vol. 2, pp. 293–304, 1984.
[68] C. Schrader, F. Seehaus, H. Capelle, A. Windhagen, H. Windhagen, and J. Krauss, “Effects of pedunculopontine area and pallidal DBS on gait ignition in Parkinson’s disease,” *Brain Stimulat.*, vol. 6, no. 6, 2013.

[69] P. Plaha and S. S. Gill, “Bilateral deep brain stimulation of the pedunculopontine nucleus for Parkinson’s disease,” *Neuroreport*, vol. 16, no. 17, pp. 1883–7, Nov. 2005.
[70] W. Thevathasan, T. J. Coyne, J. A. Hyam, G. Kerr, N. Jenkinson, T. Z. Aziz, and P. A. Silburn, “Pedunculopontine Nucleus Stimulation Improves Gait Freezing in Parkinson Disease:,” *Neurosurgery*, vol. 69, no. 6, pp. 1248–1254, Dec. 2011.
[71] W. Thevathasan, A. Pogosyan, J. A. Hyam, N. Jenkinson, T. Foltynie, P. Limousin, M. Bogdanovic, L. Zrinzo, A. L. Green, T. Z. Aziz, and P. Brown, *Alpha oscillations in the pedunculopontine nucleus correlate with gait performance in parkinsonism*, 135th ed. 2012.
[72] A. Stefani, A. M. Lozano, A. Peppe, P. Stanzione, S. Galati, D. Tropepi, M. Pierantozzi, L. Brusa, E. Scarnati, and P. Mazzone, “Bilateral deep brain stimulation of the pedunculopontine and subthalamic nuclei in severe Parkinson’s disease,” *Brain*, vol. 130, no. Pt 6, pp. 1596–607, Jun. 2007.
[73] M.-L. Welter, A. Demain, C. Ewenczyk, V. Czernecki, B. Lau, A. El Helou, H. Belaid, J. Yelnik, C. François, E. Bardinet, C. Karachi, and D. Grabli, “PPNa-DBS for gait and balance disorders in Parkinson’s disease: a double-blind, randomised study,” *J. Neurol.*, vol. 262, no. 6, pp. 1515–1525, Jun. 2015.
[74] M. U. Ferraye, B. Debû, V. Fraix, L. Goetz, C. Ardouin, J. Yelnik, C. Henry-Lagrange, E. Seigneuret, B. Piallat, P. Krack, J.-F. Le Bas, A.-L. Benabid, S. Chabardès, and P. Pollak, “Effects of pedunculopontine nucleus area stimulation on gait disorders in Parkinson’s disease,” *Brain*, vol. 133, no. 1, pp. 205–214, Jan. 2010.
[75] E. Moro, C. Hamani, Y.-Y. Poon, T. Al-Khairallah, J. O. Dostrovsky, W. D. Hutchison, and A. M. Lozano, “Unilateral pedunculopontine stimulation improves falls in Parkinson’s disease,” *Brain*, vol. 133, no. 1, pp. 215–24, Jan. 2010.
[76] W. Thevathasan, M. H. Cole, C. L. Graepel, J. A. Hyam, N. Jenkinson, J.-S. Brittain, T. J. Coyne, P. A. Silburn, T. Z. Aziz, G. Kerr, and P. Brown, “A spatiotemporal analysis of gait freezing and the impact of pedunculopontine nucleus stimulation,” *Brain J. Neurol.*, vol. 135, no. Pt 5, pp. 1446–1454, May 2012.
[77] W. Thevathasan, P. A. Silburn, H. Brooker, T. J. Coyne, S. Khan, S. S. Gill, T. Z. Aziz, and P. Brown, “The impact of low-frequency stimulation of the pedunculopontine nucleus region on reaction time in parkinsonism,” *J. Neurol. Neurosurg. Psychiatry*, vol. 81, no. 10, pp. 1099–1104, Oct. 2010.
[78] P. Mazzone, S. Sposato, A. Insola, and E. Scarnati, “The Clinical Effects of Deep Brain Stimulation of the Pedunculopontine Tegmental Nucleus in Movement Disorders May Not Be Related to the Anatomical Target, Leads Location, and Setup of Electrical Stimulation:,” *Neurosurgery*, vol. 73, no. 5, pp. 894–906, Nov. 2013.
[79] R. A. Wilcox, M. H. Cole, D. Wong, T. Coyne, P. Silburn, and G. Kerr, “Pedunculopontine nucleus deep brain stimulation produces sustained improvement in primary progressive freezing of gait,” *J Neurol Neurosurg Psychiatry*, vol. 82, no. 11, pp. 1256–1259, Sep. 2010.
[80] A. Peppe, M. Pierantozzi, C. Chiavalon, F. Marchetti, C. Caltagirone, M. Musicco, P. Stanzione, and A. Stefani, “Deep brain stimulation of the pedunculopontine

tegmentum and subthalamic nucleus: Effects on gait in Parkinson's disease," *Gait Posture*, vol. 32, no. 4, pp. 512–518, Oct. 2010.
[81] P. Mazzone, A. Insola, S. Sposato, and E. Scarnati, "The Deep Brain Stimulation of the Pedunculopontine Tegmental Nucleus," *Neuromodulation Technol. Neural Interface*, vol. 12, no. 3, pp. 191–204, 2009.
[82] S. Khan, S. S. Gill, L. Mooney, P. White, A. Whone, D. J. Brooks, and N. Pavese, "Combined pedunculopontine-subthalamic stimulation in Parkinson disease," *Neurology*, vol. 78, no. 14, pp. 1090–1095, Apr. 2012.
[83] P. Mazzone, A. Lozano, P. Stanzione, S. Galati, E. Scarnati, A. Peppe, and A. Stefani, "Implantation of human pedunculopontine nucleus: a safe and clinically relevant target in Parkinson's disease," *Neuroreport*, vol. 16, no. 17, pp. 1877–81, Nov. 2005.
[84] A. G. Androulidakis, P. Mazzone, V. Litvak, W. Penny, M. Dileone, L. M. Gaynor, S. Tisch, V. Di Lazzaro, and P. Brown, "Oscillatory activity in the pedunculopontine area of patients with Parkinson's disease," *Exp Neurol*, vol. 211, no. 1, pp. 59–66, May 2008.
[85] S. A. Shimamoto, P. S. Larson, J. L. Ostrem, G. A. Glass, R. S. Turner, and P. A. Starr, "Physiological identification of the human pedunculopontine nucleus," *J. Neurol. Neurosurg. Psychiatry*, vol. 81, no. 1, pp. 80–86, Jan. 2010.
[86] S. Breit, R. Bouali-Benazzouz, A. L. Benabid, and A. Benazzouz, "Unilateral lesion of the nigrostriatal pathway induces an increase of neuronal activity of the pedunculopontine nucleus, which is reversed by the lesion of the subthalamic nucleus in the rat," *Eur J Neurosci*, vol. 14, no. 11, pp. 1833–42, Dec. 2001.
[87] A. Fasano, L. M. Romito, A. Daniele, C. Piano, M. Zinno, A. R. Bentivoglio, and A. Albanese, "Motor and cognitive outcome in patients with Parkinson's disease 8 years after subthalamic implants," *Brain*, vol. 133, no. 9, pp. 2664–2676, Sep. 2010.
[88] M. G. Rizzone, A. Fasano, A. Daniele, M. Zibetti, A. Merola, L. Rizzi, C. Piano, C. Piccininni, L. M. Romito, L. Lopiano, and A. Albanese, "Long-term outcome of subthalamic nucleus DBS in Parkinson's disease: From the advanced phase towards the late stage of the disease?," *Parkinsonism Relat. Disord.*, vol. 20, no. 4, pp. 376–381, Apr. 2014.
[89] P. Mazzone, S. Sposato, A. Insola, and E. Scarnati, "The deep brain stimulation of the pedunculopontine tegmental nucleus: towards a new stereotactic neurosurgery," *J Neural Transm Suppl*, vol. 118, no. 10, pp. 1431–1451, 2011.
[90] A. Insola, M. Valeriani, and P. Mazzone, "Targeting the Pedunculopontine Nucleus: A New Neurophysiological Method Based on Somatosensory Evoked Potentials to Calculate the Distance of the Deep Brain Stimulation Lead From the Obex," *Neurosurg*, vol. 71, no. 1, pp. 96–103, 2012.
[91] I. Aviles-Olmos, T. Foltynie, J. Panicker, D. Cowie, P. Limousin, M. Hariz, C. J. Fowler, and L. Zrinzo, "Urinary incontinence following deep brain stimulation of the pedunculopontine nucleus," *Acta Neurochir. (Wien)*, vol. 153, no. 12, pp. 2357–2360, Dec. 2011.
[92] M. Ferraye, P. Gerardin, B. Debu, S. Chabardes, V. Fraix, E. Seigneuret, J. LeBas, A. Benabid, C. Tilikete, and P. Pollak, "Pedunculopontine nucleus stimulation

induces monocular oscillopsia," *J Neurol Neurosurg Psychiatry*, vol. 80, pp. 228–31, 2009.
[93] I. Arnulf, M. Ferraye, V. Fraix, A. L. Benabid, S. Chabardès, L. Goetz, P. Pollak, and B. Debû, "Sleep induced by stimulation in the human pedunculopontine nucleus area," *Ann. Neurol.*, vol. 67, no. 4, pp. 546–549, Apr. 2010.
[94] P. Profice, P. Mazzone, F. Pilato, M. Dileone, A. Insola, F. Ranieri, and V. Di Lazzaro, "Neurophysiological evaluation of the pedunculopontine nucleus in humans," *J Neural Transm Suppl*, vol. 118, no. 10, pp. 1423–1429, Oct. 2011.
[95] F. P. A. Romigi, "Pedunculopontine nucleus stimulation influences REM sleep in Parkinson's disease," *Eur. J. Neurol.*, vol. 15, no. 7, pp. e64 – e65, 2008.
[96] H.-B. Xiang, C. Liu, Q.-Q. Guo, R.-C. Li, and D.-W. Ye, "Deep brain stimulation of the pedunculopontine tegmental nucleus may influence renal function," *Med. Hypotheses*, vol. 77, no. 6, pp. 1135–1138, Dec. 2011.
[97] D. Ye, Q. Guo, J. Feng, C. Liu, H. Yang, F. Gao, W. Zhou, L. Zhou, H. Xiang, and R. Li, "Laterodorsal tegmentum and pedunculopontine tegmental nucleus circuits regulate renal functions: Neuroanatomical evidence in mice models," *J. Huazhong Univ. Sci. Technol. Med. Sci. Hua Zhong Ke Ji Xue Xue Bao Yi Xue Ying Wen Ban Huazhong Keji Daxue Xuebao Yixue Yingdewen Ban*, vol. 32, no. 2, pp. 216–220, Apr. 2012.
[98] D. Nandi, N. Jenkinson, J. Stein, and T. Aziz, "The pedunculopontine nucleus in Parkinson's disease: primate studies," *Br. J. Neurosurg.*, vol. 22 Suppl 1, p. 8, 2008.
[99] L. Zrinzo, L. Zrinzo, L. Massey, J. Thornton, H. Parkes, M. White, T. Yousry, C. Strand, T. Revesz, P. Limousin, M. Hariz, and J. Holton, "Targeting of the pedunculopontine nucleus by an MRI-guided approach: a cadaver study," *J Neural Transm Suppl*, vol. 118, no. 10, pp. 1487–95, 2011.
[100] L. Zrinzo, L. V. Zrinzo, S. Tisch, P. D. Limousin, T. A. Yousry, F. Afshar, and M. I. Hariz, "Stereotactic localization of the human pedunculopontine nucleus: atlas-based coordinates and validation of a magnetic resonance imaging protocol for direct localization," *Brain*, vol. 131, no. Pt 6, pp. 1588–98, Jun. 2008.
[101] P. Winn, "How best to consider the structure and function of the pedunculopontine tegmental nucleus: evidence from animal studies," *J Neurol Sci*, vol. 248, no. 1–2, pp. 234–50, DCOM 2006.
[102] T. Hashimoto, C. M. Elder, M. S. Okun, S. K. Patrick, and J. L. Vitek, "Stimulation of the subthalamic nucleus changes the firing pattern of pallidal neurons," *J Neurosci*, vol. 23, no. 5, pp. 1916–23, Mar. 2003.
[103] M. D. Johnson, J. L. Vitek, and C. C. McIntyre, "Pallidal stimulation that improves parkinsonian motor symptoms also modulates neuronal firing patterns in primary motor cortex in the MPTP-treated monkey," *Exp Neurol*, vol. 219, no. 1, pp. 359–62, Sep. 2009.
[104] P. Mazzone, A. Insola, and A. Lozano, "Peripeduncular and pedunculopontine nuclei: a dispute on a clinically relevant target," *Neuroreport*, vol. 18, pp. 1407–8, 2007.
[105] J. Yelnik, E. Bardinet, D. Dormont, G. Malandain, S. Ourselin, D. Tande, C. Karachi, N. Ayache, P. Cornu, and Y. Agid, "A three-dimensional, histological and

deformable atlas of the human basal ganglia. I. Atlas construction based on immunohistochemical and MRI data," *Neuroimage*, vol. 34, no. 2, pp. 618–38, Jan. 2007.

[106] N. Jenkinson, J. Brittain, S. Hicks, C. Kennard, and T. Aziz, "On the origin of oscillopsia during pedunculopontine stimulation," *Neuroreport*, vol. 15, pp. 2621–4, 2012.

[107] M. D. Johnson and C. C. McIntyre, "Quantifying the neural elements activated and inhibited by globus pallidus deep brain stimulation," *J Neurophysiol*, vol. 100, no. 5, pp. 2549–63, Nov. 2008.

[108] M. D. Johnson, J. Zhang, D. Ghosh, C. C. McIntyre, and J. L. Vitek, "Neural targets for relieving parkinsonian rigidity and bradykinesia with pallidal deep brain stimulation," *J Neurophysiol*, vol. 108, no. 2, pp. 567–77, Jul. 2012.

[109] S. Miocinovic, M. Parent, C. R. Butson, P. J. Hahn, G. S. Russo, J. L. Vitek, and C. C. McIntyre, "Computational analysis of subthalamic nucleus and lenticular fasciculus activation during therapeutic deep brain stimulation," *J Neurophysiol*, vol. 96, no. 3, pp. 1569–80, Sep. 2006.

[110] W. Xu, S. Miocinovic, J. Zhang, K. B. Baker, C. C. McIntyre, and J. L. Vitek, "Dissociation of motor symptoms during deep brain stimulation of the subthalamic nucleus in the region of the internal capsule," *Exp Neurol*, vol. 228, no. 2, pp. 294–7, Apr. 2011.

[111] T. Naidich and H. Duvernoy, *Duvernoy's Atlas of the Human Brain Stem and Cerebellum: High-field MRI: Surface Anatomy, Internal Structure, Vasculatization and 3D Sectional Anatomy*. Wien: Springer, 2009.

[112] R. Nieuwenhuys, J. Voogd, and C. Huijzen, *The Human Central Nervous System*. Berlin: Springer, 2008.

[113] P. Perrini, G. Tiezzi, M. Castagna, and R. Vannozzi, "Three-dimensional microsurgical anatomy of cerebellar peduncles," *Neurosurg. Rev.*, no. 1437–2320 (Electronic), pp. 1–11, Aug. 2012.

[114] J. Kojima, Y. Yamaji, M. Matsumura, A. Nambu, M. Inase, H. Tokuno, M. Takada, and H. Imai, "Excitotoxic lesions of the pedunculopontine tegmental nucleus produce contralateral hemiparkinsonism in the monkey," *Neurosci Lett*, vol. 226, no. 2, pp. 111–4, 1997.

[115] M. Matsumura and J. Kojima, "The role of the pedunculopontine tegmental nucleus in experimental parkinsonism in primates," *Ster. Funct Neurosurg*, vol. 77, pp. 108–15, DCOM 2001.

[116] P. Mazzone, S. Sposato, A. Insola, V. Dilazzaro, and E. Scarnati, "Stereotactic surgery of nucleus tegmenti pedunculopontini," *Br. J. Neurosurg.*, vol. 22, no. s1, pp. S33–S40, 2008.

[117] A. H. Koeppen, K. D. Barron, and M. P. Dentinger, "Olivary hypertrophy," *Neurology*, vol. 30, no. 5, p. 471, May 1980.

[118] G. Paxinos, *The Rhesus Monkey Brain: In Stereotaxic Coordinates*. Elsevier/Academic Press, 2009.

[119] C. M. Elder, T. Hashimoto, J. Zhang, and J. L. Vitek, "Chronic implantation of deep brain stimulation leads in animal models of neurological disorders," *J Neurosci Methods*, vol. 142, no. 1, pp. 11–16, 2005.
[120] M. Keane, S. Deyo, A. Abosch, J. A. Bajwa, and M. D. Johnson, "Improved spatial targeting with directionally segmented deep brain stimulation leads for treating essential tremor," *J Neural Eng*, vol. 9, no. 4, p. 046005, 2012.
[121] H. C. F. Martens, E. Toader, M. M. J. Decré, D. J. Anderson, R. Vetter, D. R. Kipke, K. B. Baker, M. D. Johnson, and J. L. Vitek, "Spatial steering of deep brain stimulation volumes using a novel lead design," *Clin. Neurophysiol.*, vol. 122, no. 3, pp. 558–566, 2011.
[122] C. C. McIntyre, W. M. Grill, D. L. Sherman, and N. V. Thakor, "Cellular effects of deep brain stimulation: model-based analysis of activation and inhibition," *J Neurophysiol*, vol. 91, no. 4, pp. 1457–69, Apr. 2004.
[123] C. C. McIntyre, A. G. Richardson, and W. M. Grill, "Modeling the excitability of mammalian nerve fibers: influence of afterpotentials on the recovery cycle," *J Neurophysiol*, vol. 87, no. 2, pp. 995–1006, Feb. 2002.
[124] M. L. Hines and N. T. Carnevale, "The NEURON simulation environment," *Neural Comput*, vol. 9, no. 6, pp. 1179–209, Aug. 1997.
[125] K. Takakusaki, T. Shiroyama, and S. T. Kitai, "Two types of cholinergic neurons in the rat tegmental pedunculopontine nucleus: electrophysiological and morphological characterization," *Neuroscience*, vol. 79, no. 4, pp. 1089–1109, 1997.
[126] N. Nandi D, Aziz TZ, Stein JF Jenkinson, "Pedunculopontine nucleus: a new target for deep brain stimulation for akinesia," *Neuroreport*, vol. 16, no. 17, pp. 1875–6, Nov. 2005.
[127] J. B. Ranck Jr., "Which elements are excited in electrical stimulation of mammalian central nervous system: a review," *Brain Res*, vol. 98, no. 3, pp. 417–40, Nov. 1975.
[128] W. M. Grill and J. T. Mortimer, "Electrical properties of implant encapsulation tissue," *Ann Biomed Eng*, vol. 22, no. 1, pp. 23–33, Jan. 1994.
[129] C. R. Butson and C. C. McIntyre, "Tissue and electrode capacitance reduce neural activation volumes during deep brain stimulation," *Clin Neurophysiol*, vol. 116, no. 10, pp. 2490–500, Oct. 2005.
[130] E. Forsaa, J. P. Larsen, T. Wentzel-Larsen, K. Herlofson, and G. Alves, "Epidemiology of Parkinson's disease," *Mov. Disord*, vol. 23, no. 10, pp. 1420–27, DCOM 2008.
[131] D. Muslimović, B. Post, J. D. Speelman, B. Schmand, and R. J. de Haan, "Determinants of disability and quality of life in mild to moderate Parkinson disease," *Neurology*, vol. 70, no. 23, pp. 2241–7, Jun. 2008.
[132] R. M. Pickering, Y. A. M. Grimbergen, U. Rigney, A. Ashburn, G. Mazibrada, B. Wood, P. Gray, G. Kerr, and B. R. Bloem, "A meta-analysis of six prospective studies of falling in Parkinson's disease," *Mov. Disord.*, vol. 22, no. 13, pp. 1892–1900, 2007.

[133] S. Rahman, H. Griffin, N. Quinn, and M. Jahanshahi, "Quality of life in Parkinson's disease: the relative importance of the symptoms," *Mov. Disord*, vol. 23, no. 10, pp. 1428–34, DCOM 2008.
[134] E. L. Johnsen, "Gait and postural instability in Parkinson's disease treated with deep brain stimulation of the subthalamic nucleus," *Dan Med Bull*, vol. 58, no. 10, p. B4334, 20111006.
[135] E. L. Johnsen, P. H. Mogensen, N. A. Sunde, and K. Østergaard, "Improved asymmetry of gait in Parkinson's disease with DBS: Gait and postural instability in Parkinson's disease treated with bilateral deep brain stimulation in the subthalamic nucleus," *Mov. Disord.*, vol. 24, no. 4, pp. 588–95, 2009.
[136] R. Kumar, A. M. Lozano, Y. J. Kim, W. D. Hutchison, E. Sime, E. Halket, and A. E. Lang, "Double-blind evaluation of subthalamic nucleus deep brain stimulation in advanced Parkinson's disease," *Neurology*, vol. 51, pp. 850–5, 1998.
[137] W. Liu, K. McIntire, S. H. Kim, J. Zhang, S. Dascalos, K. E. Lyons, and R. Pahwa, "Bilateral subthalamic stimulation improves gait initiation in patients with Parkinson's disease," *Gait Posture*, vol. 23, no. 4, pp. 492–8, 2006.
[138] N. Shivitz, M. M. Koop, J. Fahimi, G. Heit, and H. M. Bronte-Stewart, "Bilateral subthalamic nucleus deep brain stimulation improves certain aspects of postural control in Parkinson's disease, whereas medication does not," *Mov. Disord.*, vol. 21, no. 8, pp. 1088–1097, 2006.
[139] T. Xie, U. J. Kang, and P. Warnke, "Effect of stimulation frequency on immediate freezing of gait in newly activated STN DBS in Parkinson's disease," *J. Neurol. Neurosurg. Psychiatry*, vol. 83, no. 10, pp. 1015–1017, Oct. 2012.
[140] A. M. S. Muniz, J. Nadal, K. E. Lyons, R. Pahwa, and W. Liu, "Long-term evaluation of gait initiation in six Parkinson's disease patients with bilateral subthalamic stimulation," *Gait Posture*, vol. 35, no. 3, pp. 452–7, 2012.
[141] D. Tarsy, D. Apetauerova, P. Ryan, and T. Norregaard, "Adverse effects of subthalamic nucleus DBS in a patient with multiple system atrophy," *Neurology*, vol. 61, no. 2, pp. 247–9, Jul. 2003.
[142] S.-H. Kuo, C. Kenney, and J. Jankovic, "Bilateral pedunculopontine nuclei strokes presenting as freezing of gait," *Mov. Disord.*, vol. 23, no. 4, pp. 616–619, 2008.
[143] S. M. Brudzynski, M. Wu, and G. J. Mogenson, "Modulation of locomotor activity induced by injections of barbachol into the tegmental pedunculopontine nucleus and adjacent areas in the rat," *Brain Res*, vol. 451, pp. 119–25, 1988.
[144] N. Jenkinson, D. Nandi, R. C. Miall, J. F. Stein, and T. Z. Aziz, "Pedunculopontine nucleus stimulation improves akinesia in a Parkinsonian monkey," *Neuroreport*, vol. 15, no. 17, pp. 2621–4, Dec. 2004.
[145] B. R. Aravamuthan, K. A. Muthusamy, J. F. Stein, T. Z. Aziz, and H. Johansen-Berg, "Topography of cortical and subcortical connections of the human pedunculopontine and subthalamic nuclei," *Neuroimage*, vol. 37, no. 3, pp. 694–705, 2007.
[146] M. E. Fernandez-Villalba, A. Fernandez-Barreiro, M.T. Herrero Gomez-Gallego, "Changes in the neuronal activity in the pedunculopontine nucleus in chronic

MPTP-treated primates: an in situ hybridization study of cytochrome oxidase subunit I, choline acetyl transferase and substance P mRNA expression," *J. Neural Transm.*, vol. 114, no. 3, pp. 319–26, 2007.

[147] J. Zhang, Z. I. Wang, K. B. Baker, and J. L. Vitek, "Effect of globus pallidus internus stimulation on neuronal activity in the pedunculopontine tegmental nucleus in the primate model of Parkinson's disease," *Exp Neurol*, vol. 233, no. 1, pp. 575–80, 2012.

[148] K. Jellinger, "The pedunculopontine nucleus in Parkinson's disease, progressive supranuclear palsy and Alzheimer's disease," *J.Neurol.Neurosurg.Psychiatr.*, vol. 51, pp. 540–543, 1988.

[149] B. R. Aravamuthan, D. A. Bergstrom, R. A. French, J. J. Taylor, L. C. Parr-Brownlie, and J. R. Walters, "Altered neuronal activity relationships between the pedunculopontine nucleus and motor cortex in a rodent model of Parkinson's disease," *Exp Neurol*, vol. 213, no. 2, pp. 268–80, Jun. 2008.

[150] N. K. Iwata, R. Hanajima, T. Furubayashi, Y. Terao, H. Uesugi, Y. Shiio, H. Enomoto, H. Mochizuki, I. Kanazawa, and Y. Ugawa, "Facilitatory effect on the motor cortex by electrical stimulation over the cerebellum in humans," *Exp. Brain Res.*, vol. 159, no. 4, pp. 418–424, 2004.

[151] M. Alam, K. Schwabe, and J. K. Krauss, "The pedunculopontine nucleus area: critical evaluation of interspecies differences relevant for its use as a target for deep brain stimulation," *Brain*, vol. 134, no. 1, pp. 11–23, Jan. 2011.

[152] T. Z. Aziz, L. Davies, J. Stein, and S. France, "The role of descending basal ganglia connections to the brain stem in Parkinsonian akinesia," *Br. J. Neurosurg.*, vol. 12, no. 3, pp. 245–49, Jun. 1998.

[153] M. Matsumura, "The pedunculopontine tegmental nucleus and experimental parkinsonism," *J Neurol*, vol. 252, no. 0, pp. iv5–iv12, 2005.

[154] C. R. Butson, S. E. Cooper, J. M. Henderson, and C. C. McIntyre, "Patient-specific analysis of the volume of tissue activated during deep brain stimulation," *Neuroimage*, vol. 34, no. 2, pp. 661–70, Jan. 2007.

[155] T. Foltynie, L. Zrinzo, I. Martinez-Torres, E. Tripoliti, E. Petersen, E. Holl, I. Aviles-Olmos, M. Jahanshahi, M. Hariz, and P. Limousin, "MRI-guided STN DBS in Parkinson's disease without microelectrode recording: efficacy and safety," *J. Neurol. Neurosurg. Psychiatry*, vol. 82, no. 4, pp. 358–363, Apr. 2011.

[156] C. A. Giller, R. B. Dewey, M. I. Ginsburg, D. B. Mendelsohn, and A. M. Berk, "Stereotactic pallidotomy and thalamotomy using individual variations of anatomic landmarks for localization," *Neurosurgery*, vol. 42, no. 1, pp. 56–62; discussion 62–5, Jan. 1998.

[157] J. Alvarez-Linera, "Magnetic Resonance Techniques for the Brainstem," *Semin. Ultrasound CT MRI*, vol. 31, no. 3, pp. 230–245, 2010.

[158] L. M. Nagae-Poetscher, H. Jiang, S. Wakana, X. Golay, P. C. M. van Zijl, and S. Mori, "High-Resolution Diffusion Tensor Imaging of the Brain Stem at 3 T," *Am. J. Neuroradiol.*, vol. 25, no. 8, pp. 1325–1330, Sep. 2004.

[159] E. R. Gizewski, S. Maderwald, J. Linn, B. Dassinger, K. Bochmann, M. Forsting, and M. E. Ladd, "High-resolution anatomy of the human brain stem using 7-T MRI:

improved detection of inner structures and nerves?," *Neuroradiology*, vol. 56, no. 3, pp. 177–186, 2014.
[160] M. Weiss, A. Alkemade, M. C. Keuken, C. Muller-Axt, S. Geyer, R. Turner, and B. U. Forstmann, "Spatial normalization of ultrahigh resolution 7 T magnetic resonance imaging data of the postmortem human subthalamic nucleus: a multistage approach," *Brain Struct Funct*, 2014.
[161] P. Novak, V. Novak, A. Kangarlu, A. M. Abduljalil, D. W. Chakeres, and P. Robitaille, "High Resolution MRI of the Brainstem at 8T," *J. Comput. Assist. Tomogr.*, vol. 25, no. 2, pp. 242–246, 2001.
[162] J. Diedrichsen, S. Maderwald, and K. M., "Imaging the deep cerebellar nuclei: a probabilistic atlas and normalization procedure," *Neuroimaging*, vol. 54, pp. 1786–1794, 2011.
[163] I. Nolte, L. Gerigk, and M. Al-Zghloul, "Visualization of the internal globus pallidus: sequence and orientation for deep brain stimulation using a standard installation procol at 3.0 Tesla," *Acta Nuerochir Wien*, vol. 154, no. 481–494, 2012.
[164] M. Eapen, D. H. Zald, J. C. Gatenby, Z. Ding, and J. C. Gore, "Using High-Resolution MR Imaging at 7T to Evaluate the Anatomy of the Midbrain Dopaminergic System," *Am. J. Neuroradiol.*, vol. 32, no. 4, pp. 688–694, Apr. 2011.
[165] K. Sakaie, M. Takahashi, K. Sagiyama, I. Dimitrov, T. Frohman, G. Remington, E. Frohman, and R. J. Fox, "Injury to a specific neural pathway detected by ultra-high-field MRI," *Neurology*, vol. 82, no. 2, pp. 182–183, Jan. 2014.
[166] N. Tani, O. Joly, H. Iwamuro, L. Uhrig, C. J. Wiggins, C. Poupon, H. Kolster, W. Vanduffel, D. Le Bihan, S. Palfi, and B. Jarraya, "Direct visualization of non-human primate subcortical nuclei with contrast-enhanced high field MRI," *Neuroimage*, vol. 58, no. 1, pp. 60–68, 2011.
[167] J. P. Marques and R. Gruetter, "New Developments and Applications of the MP2RAGE Sequence - Focusing the Contrast and High Spatial Resolution R Mapping," *PLoS One*, vol. 8, no. 7, p. e69294, 2013.
[168] M. C. Keuken, P. L. Bazin, L. Crown, J. Hootsmans, A. Laufer, C. Müller-Axt, R. Sier, E. J. van der Putten, A. Schäfer, R. Turner, and B. U. Forstmann, "Quantifying inter-individual anatomical variability in the subcortex using 7T structural MRI," *Neuroimage*, vol. 94, no. 0, pp. 40–46, 2014.
[169] M. C. Keuken, P. L. Bazin, A. Schafer, J. Neumann, R. Turner, and B. U. Forstmann, "Ultra-High 7T MRI of Structural Age-Related Changes of the Subthalamic Nucleus," *J Neurosci*, vol. 33, no. 11, pp. 4896–4900, 2013.
[170] A. Deistung, A. Schafer, F. Schweser, I. Biederman, D. Gullmar, R. Trampel, R. Turner, and J. R. Reichenbach, "High-resolution MR imaging of the human brainstem in vivo at 7 Tesla," *Front. Hum. Neurosci.*, vol. 7, no. 710, pp. 1–12, 2013.
[171] C. Habas and E. Cabanis, "Anatomical parcellation of the brainstem and cerebellar white matter: a preliminary probabilistic tractography study at 3 T," *Neuroradiology*, vol. 49, no. 10, pp. 849–863, Oct. 2007.

[172] T. Janssens, B. Keil, P. Serano, A. Mareyam, J. A. McNab, L. L. Wald, and W. Vanduffel, “A 22-channel receive array with Helmholtz transmit coil for anesthetized macaque MRI at 3 T,” *NMR Biomed.*, vol. 26, no. 11, pp. 1431–1440, 2013.

[173] E. Ziegler, M. Rouillard, E. Andre, T. S. Coolen J., E. Balteau, C. Phillips, and G. Garraux, “Mapping track density changes in nigrostriatal and extranigral pathways in Parkinson’s disease,” *Neuroimage*, vol. 99, pp. 498–508, 2014.

[174] G. Soria, M. De Notaris, R. Tudela, G. Blasco, J. Puig, A. M. Planas, S. Pedraza, and A. Prats-Galino, “Improved Assessment of Ex Vivo Brainstem Neuroanatomy With High-Resolution MRI and DTI at 7 Tesla,” *Anat. Rec. Adv. Integr. Anat. Evol. Biol.*, vol. 294, no. 6, pp. 1035–1044, 2011.

[175] C. Lenglet, A. Abosch, E. Yacoub, F. De Martino, G. Sapiro, and N. Harel, “Comprehensive in vivo mapping of the human basal ganglia and thalamic connectome in individuals using 7T MRI,” *PLoS One*, vol. 7, no. 1, p. e29153, 2012.

[176] B. Stieltjes, W. E. Kaufmann, P. C. M. van Zijl, K. Fredericksen, G. D. Pearlson, M. Solaiyappan, and S. Mori, “Diffusion tensor imaging and axonal tracking in the human brainstem,” *Neuroimage*, vol. 14, no. 3, pp. 723–735, 2001.

[177] D. S. Yang, J. H. Hong, W. M. Byun, S. Y. Kwak, S. H. Ahn, H. Lee, C. H. Hwang, and S. H. Jang, “Identification of the medial lemniscus in the human brain: Combined study of functional MRI and diffusion tensor tractography,” *Neurosci Lett*, vol. 459, no. 1, pp. 19–24, 2009.

[178] J. A. Sweet, B. L. Walter, K. Gunalan, A. Chaturvedi, C. C. McIntyre, and J. P. Miller, “Fiber tractography of the axonal pathways linking the basal ganglia and cerebellum in Parkinson disease: implications for targeting in deep brain stimulation,” *J Neurosurg*, vol. 120, no. 4, pp. 988–996, 2014.

[179] M. Aggarwal, J. Zhang, O. Pletnikova, B. Crain, J. Troncoso, and S. Mori, “Feasibility of creating a high-resolution 3D diffusion tensor imaging based atlas of the human brainstem: A case study at 11.7T,” *Neuroimage*, vol. 74, no. 0, pp. 117–127, 2013.

[180] A. K. Seehaus, A. Roebroeck, O. Chiry, D.-S. Kim, I. Ronen, H. Bratzke, R. Goebel, and R. A. W. Galuske, “Histological Validation of DW-MRI Tractography in Human Postmortem Tissue,” *Cereb. Cortex*, vol. 23, no. 2, pp. 442–450, Feb. 2013.

[181] Y. Duchin, A. Abosch, E. Yacoub, G. Sapiro, and N. Harel, “Feasibility of Using Ultra-High Field (7 T) MRI for Clinical Surgical Targeting,” *PLoS One*, vol. 7, no. 5, p. e37328, 2012.

[182] A. Abosch, E. Yacoub, K. Ugurbil, and N. Harel, “An Assessment of current brain targets for deep brain stimulation surgery with susceptibility-weighted imaging at 7 tesla,” *Neurosurg*, vol. 67, no. 6, pp. 1745–56, 2010.

[183] J. M. Duarte-Carvajalino, G. Sapiro, N. Harel, and C. Lenglet, “A Framework for Linear and Non-linear Registration of Diffusion-Weighted MRIs using Angular Interpolation,” *Front Neurosci*, vol. 7, no. 41, 2013.

[184] L. Zhan, B. A. Mueller, N. Jahanshad, Y. Jin, C. Lenglet, E. Yacoub, G. Sapiro, K. Ugurbil, N. Harel, A. W. Toga, K. O. Lim, and P. M. Thompson, "Magnetic Resonance Field Strength Effects on Diffusion Measures and Brain Connectivity Networks," *Brain Connect.*, vol. 3, no. 1, pp. 72–86, 2013.
[185] D. L. Polders, A. Leemans, J. Hendrikse, M. J. Donahue, P. R. Luijten, and J. M. Hoogduin, "Signal to noise ratio and uncertainty in diffusion tensor imaging at 1.5, 3.0, and 7.0 Tesla," *JMRI*, vol. 33, no. 6, pp. 1456–1463, 2011.
[186] L. M. Zitella, K. Mohsenian, M. Pahwa, C. Gloeckner, and M. D. Johnson, "Computational modeling of pedunculopontine nucleus deep brain stimulation," *J Neural Eng*, vol. 10, no. 4, p. 045005, 2013.
[187] G. Adriany, N. Harel, E. Yacoub, S. Moeller, G. Ghose, and K. Ugurbil, "A 21 channel Transceiver Array for Non-human Primate Applications at 7 Tesla." 2010.
[188] E. Stejskal and J. Tanner, "Spin Diffusion Measurements: Spin Echoes in the Presence of a Time-Dependent Field Gradient," *J Chem Phys*, vol. 42, pp. 288–92, 1965.
[189] J. L. R. Andersson, S. Skare, and J. Ashburner, "How to correct susceptibility distortions in spin-echo echo-planar images: application to diffusion tensor imaging," *Neuroimage*, vol. 20, no. 2, pp. 870–888, 2003.
[190] S. Schaefer, T. McPhail, and J. Warren, "Image deformation using moving least squares," *ACM Trans Graph*, vol. 25, no. 3, pp. 533–540, 2006.
[191] B. Tiddeman, "A general method for overlap control in image warping," *Comput. Graph.*, vol. 25, no. 1, pp. 59–66, 2001.
[192] C. D. Markovitz, T. T. Tang, D. P. Edge, and H. H. Lim, "Three-dimensional brain reconstruction of in vivo electrode tracks for neuroscience and neural prosthetic applications," *Front. Neural Circuits*, vol. 6, no. 00039, 2012.
[193] C. F. Jenkinson, T. E. Beckmann, M. W. Behrens, M. W. Woolrich, and S. M. Smith, "FSL," *NeuroImage*, vol. 62, pp. 782–90, 2012.
[194] M. W. Woolrich, S. Jbabdi, B. Patenaude, M. Chappell, S. Makni, T. Behrens, C. Beckmann, M. Jenkinson, and S. M. Smith, "Bayesian analysis of neuroimaging data in FSL," *Neuroimage*, vol. 45, no. 1, Supplement 1, pp. S173–S186, 2009.
[195] S. M. Smith, M. Jenkinson, M. W. Woolrich, C. F. Beckmann, T. E. J. Behrens, H. Johansen-Berg, P. R. Bannister, M. De Luca, I. Drobnjak, D. E. Flitney, R. Niazy, J. Saunders, J. Vickers, Y. Zhang, N. De Stefano, J. M. Brady, and P. M. Matthews, "Advances in functional and structural MR image analysis and implementation as FSL," *Neuroimage*, vol. 23, no. S1, pp. 208–19, 2004.
[196] S. M. Smith, "Fast robust automated brain extraction," *Hum Brain Mapp*, vol. 17, no. 3, pp. 143–155, 2002.
[197] M. Jenkinson, P. Bannister, J. M. Brady, and S. M. Smith, "Improved Optimisation for the Robust adn Accurate Linear Registration and Motion Correction of Brain Images," *Neuroimage*, vol. 17, no. 2, pp. 825–841, 2002.
[198] M. Jenkinson and S. M. Smith, "A Global Optimisation Method for Robust Affine Registration of Brain Images," *Med. Image Anal.*, vol. 5, no. 2, pp. 143–156, 2001.
[199] D. N. Greve and B. Fischl, "Accurate and robust brain image alignment using boundary-based registration," *Neuroimage*, vol. 48, no. 1, pp. 63–72, 2009.

[200] C. Hamani, J. M. Schwalb, A. R. Rezai, J. O. Dostrovsky, K. D. Davis, and A. M. Lozano, "Deep brain stimulation for chronic neuropathic pain: Long-term outcome and the incidence of insertional effect," *Pain*, vol. 125, no. 1–2, pp. 188–196, 2006.
[201] T. Lenarz, H. H. Lim, G. Reuter, J. F. Patrick, and M. Lenarz, "The Auditory Midbrain Implant: A New Auditory Prosthesis for Neural Deafness-Concept and Device Description," *Otol. Neurotol.*, vol. 27, no. 6, pp. 838–843, 2006.
[202] H. M. Duvernoy and J. L. Vannson, *Human brainstem vessels*. Springer-Verlag Berlin, 1978.
[203] Y. Hosobuchi, "Dorsal Periaqueductal Grey-Matter Stimulation in Humans," *Pacing Clin Electrophysiol*, vol. 10, no. 1, pp. 213–216, 1987.
[204] H. H. Lim, T. Lenarz, D. J. Anderson, and M. Lenarz, "The auditory midbrain implant: Effects of electrode location," *Hear. Res.*, vol. 242, no. 1–2, pp. 74–85, 2008.
[205] D. J. Mayer, T. L. Wolfle, H. Akil, B. Carder, and J. C. Liebeskind, "Analgesia from Electrical Stimulation in the Brainstem of the Rat," *Science*, vol. 174, no. 4016, pp. 1351–1254, 1971.
[206] D. J. Mayer and J. C. Liebeskind, "Pain reduction by focal electrical stimulation of the brain: an anatomical and behavioral analysis," *Brain Res*, vol. 68, pp. 73–93, 1974.
[207] K. A. Ganser, H. Dickhaus, R. Metzner, and C. R. Wirtz, "A deformable digital brain atlas system according to Talairach and Tournoux," *Med. Image Anal.*, vol. 8, no. 1, pp. 3–22, 2004.
[208] A. F. Sadikot, M. M. Chakravarty, G. Bertrand, V. V. Rymar, F. Al-Subaie, and L. D. Collins, "Creation of computerized 3D MRI-integrated atlases of the human basal ganglia and thalamus," *Front. Syst. Neurosci.*, vol. 5, no. 00071, 2011.
[209] P. St-Jean, A. F. Sadikot, L. Collins, D. Clonda, R. Kasrai, A. C. Evans, and T. M. Peters, "Automated atlas integration and interactive three-dimensional visualization tools for planning and guidance in functional neurosurgery," *IEEE Trans. Med. Imaging*, vol. 17, no. 5, pp. 672–680, 1998.
[210] C. Bohm, T. Greitz, D. Kingsley, B. M. Berggren, and L. Olsson, "Adjustable computerized stereotaxic brain atlas for transmission and emission tomography," *Am. J. Neuroradiol.*, vol. 4, no. 3, pp. 731–3, May 1983.
[211] A. C. Evans, S. Beil, S. Marrett, C. J. Thompson, and A. Hakim, "Anatomical-Functional Correlation Using an Adjustable MRI-Based Region of Interest Atlas with Positron Emission Tomography," *J Cereb Blood Flow Metab*, vol. 8, no. 4, pp. 513–530, 1988.
[212] R. Dann, J. Hoford, S. Kovacic, M. Reivich, and R. Bajcsy, "Three-Dimensional Computerized Brain Atlas for Elastic Matching: Creation and Initial Evaluation," *Proc SPIE*, vol. 0914, pp. 600–608, 1988.
[213] S. Sandor and R. Leahy, "Matching deformable atlas models to preprocessed magnetic resonance brain images," presented at the IEEE International Conference, Austin, TX, 1994, vol. 3, pp. 686–690.

[214] J. Gee, M. Reivich, L. Bilaniuk, D. Z. Hackney R., S. Kovacic, and R. Bajcsy, "Evaluation of multiresolution elastic matching using MRI data," *SPIE*, vol. 1445, pp. 226–234, 1991.
[215] A. Chaturvedi, T. J. Foutz, and C. C. McIntyre, "Current steering to activate targeted neural pathways during deep brain stimulation of the subthalamic region," *Brain Stimulat.*, vol. 5, no. 3, pp. 369–377, 2012.
[216] C. R. Butson and C. C. McIntyre, "Current Steering to Control the Volume of Tissue Activated During Deep Brain Stimulation," *Brain Stimulat.*, vol. 1, no. 1, pp. 7–15, 2008.
[217] H. Wang, J. Zhu, M. Reuter, L. N. Vinke, A. Yendiki, D. A. Boas, B. Fischl, and T. Akkin, "Cross-validation of serial optical coherence scanning and diffusion tensor imaging: A study on neural fiber maps in human medulla oblongata," *Neuroimage*, vol. 100, pp. 395–404, 2014.
[218] S. Miocinovic, J. Zhang, W. Xu, G. S. Russo, J. L. Vitek, and C. C. McIntyre, "Stereotactic neurosurgical planning, recording, and visualization for deep brain stimulation in non-human primates," *J Neurosci Methods*, vol. 162, no. 1–2, pp. 32–41, May 2007.
[219] P. Mazzone, M. Paoloni, M. Mangone, V. Santilli, A. Insola, M. Fini, and E. Scarnati, "Unilateral deep brain stimulation of the pedunculopontine tegmental nucleus in idiopathic Parkinson's disease: Effects on gait initiation and performance," *Gait Posture*, vol. 40, no. 3, 2014.
[220] L. G. Nowak and J. Bullier, "Axons, but not cell bodies, are activated by electrical stimulation in cortical gray matter I. Evidence from chronaxie measurements," *Exp. Brain Res.*, vol. 118, no. 4, pp. 477–488, Feb. 1998.
[221] J. Murata, M. Kitagawa, H. Uesugi, H. Saito, Y. Iwasaki, S. Kikuchi, K. Tashiro, and Y. Sawamura, "Electrical stimulation of the posterior subthalamic area for the treatment of intractable proximal tremor," *J Neurosurg*, vol. 99, no. 4, pp. 708–15, Oct. 2003.
[222] F. Matsuo and E. T. Ajax, "Palatal myoclonus and denervation supersensitivity in the central nervous system," *Ann Neurol*, vol. 5, no. 1, pp. 72–78, 1979.
[223] A. Chaturvedi, C. Butson, S. Lempka, S. Cooper, and C. McIntyre, "Patient-specific models of deep brain stimulation: Influence of field model complexity on neural activation predictions," *Brain Stimulat.*, vol. 3, no. 2, 2010.
[224] C. R. Butson, S. E. Cooper, J. M. Henderson, B. Wolgamuth, and C. C. McIntyre, "Probabilistic analysis of activation volumes generated during deep brain stimulation," *Neuroimage*, vol. 54, no. 3, pp. 2096–104, Feb. 2011.
[225] A. Barmpoutis, M. S. Hwang, D. Howland, J. R. Forder, and B. C. Vemuri, "Regularized positive-definite fourth order tensor field estimation from DW-MRI," *Neuroimage*, vol. 45, no. 1 Suppl, p. 62, 2009.
[226] A. Barmpoutis and B. C. Vemuri, "A unified framework for estimating diffusion tensors of any order with symmetric positive-definite constraints," *Proc. IEEE Int. Symp. Biomed. Imaging Nano Macro*, pp. 1385–1388, 2010.

[227] D. S. Tuch, V. J. Wedeen, A. M. Dale, J. S. George, and J. W. Belliveau, "Conductivity tensor mapping of the human brain using diffusion tensor MRI," *Proc. Natl. Acad. Sci.*, vol. 98, no. 20, Sep. 2001.
[228] C. Schmidt and U. van Rienen, "Modeling the field distribution in deep brain stimulation: the influence of anisotropy of brain tissue," *IEEE Trans. BME*, vol. 59, no. 6, 2012.
[229] M. J. Birdno, A. M. Kuncel, A. D. Dorval, D. A. Turner, R. E. Gross, and W. M. Grill, "Stimulus features underlying reduced tremor suppression with temporally patterned deep brain stimulation," *J Neurophysiol*, vol. 107, no. 1, pp. 364–383, 2011.
[230] G. Garraux, M. A. Bahri, C. Lemaire, C. Degueldre, E. Salmon, and B. Kaschten, "Brain energization in response to deep brain stimulation of subthalamic nuclei in Parkinson's disease," *J. Cereb. Blood Flow Metab.*, vol. 31, no. 7, pp. 1612–1622, 2011.
[231] K. Oguchi, K. Arakawa, S. Nelson, and F. Samson, "The influence of droperidol, diazepam, and physostigmine on ketamine-induced behavior and brain regional glucose utilization in rat," *Anesthesiology*, vol. 57, no. 5, pp. 353–358, 1982.
[232] T. Wyckhuys, L. wyffels, X. Langlois, M. Schmidt, S. Stroobants, and S. Staelens, "The [18F]FDG μPET readout of a brain activation model to evaluate the metabotropic glutamate receptor 2 positive allosteric modulator JNJ-42153605," *J. Pharmacol. Exp. Ther.*, vol. 350, no. 2, pp. 375–386, Aug. 2014.
[233] L. L. B. Ponto, Y. Menda, V. A. Magnotta, T. H. Yamada, N. L. Denburg, and S. K. Schultz, "Frontal hypometabolism in elderly breast cancer survivors determined by [18F] fluorodeoxyglucose (FDG) positron emission tomography (PET): a pilot study," *Int. J. Geriatr. Psychiatry*, 2014.
[234] A. Jena, S. Taneja, R. Goel, P. Renjen, and P. Negi, "Reliability of semiquantitative 18F-FDG PET parameters derived from simultaneous brain PET/MRI: A feasibility study," *Eur. J. Radiol.*, vol. 83, no. 7, pp. 1269–1274, 2014.
[235] T. Rohlfing, C. D. Kroenke, E. V. Sullivan, M. F. Dubach, D. M. Bowden, K. A. Grant, and A. Pfefferbaum, "The INIA19 Template and NeuroMaps Atlas for Primate Brain Image Parcellation and Spatial Normalization," *Front. Neuroinformatics*, vol. 6, p. 27, 2012.
[236] C. Pierpaoli, P. Jezzard, P. J. Basser, A. Barnett, and G. D. Chiro, "Diffusion tensor MR imaging of the human brain," *Radiology*, vol. 201, no. 3, pp. 637–648, 1996.
[237] S. Miocinovic, S. F. Lempka, G. S. Russo, C. B. Maks, C. R. Butson, K. E. Sakaie, J. L. Vitek, and C. C. McIntyre, "Experimental and theoretical characterization of the voltage distribution generated by deep brain stimulation," *Exp Neurol*, vol. 216, no. 1, pp. 166–76, Mar. 2009.
[238] C. C. McIntyre, S. Mori, D. L. Sherman, N. V. Thakor, and J. L. Vitek, "Electric field and stimulating influence generated by deep brain stimulation of the subthalamic nucleus," *Clin Neurophysiol*, vol. 115, no. 3, pp. 589–95, Mar. 2004.

[239] C. R. Butson, C. B. Maks, and C. C. McIntyre, "Sources and effects of electrode impedance during deep brain stimulation," *Clin Neurophysiol*, vol. 117, no. 2, pp. 447–54, Feb. 2006.
[240] F. F. Rattay, "The basic mechanism for the electrical stimulation of the nervous system," *Neuroscience*, vol. 89, no. 2, pp. 335–346, 1999.
[241] M. Melling, D. Karimian-Teherani, M. Behnam, and S. Mostler, "Morphological study of the healthy human oculomotor nerve by atomic force microscopy," *Neuroimage*, vol. 20, no. 2, pp. 795–801, 2003.
[242] J. D. Porter, L. A. Burns, and P. J. May, "Morphological substrate for eyelid movements: Innervation and structure of primate levator palpebrae superioris and orbicularis oculi muscles," *J Comp Neurol*, vol. 287, no. 1, pp. 64–81, 1989.
[243] H. Blumenfeld, *Neuroanatomy through clinical cases*. Sinauer Sunderland, MA, 2002.
[244] J. L. Lujan, A. Chaturvedi, D. A. Malone, A. R. Rezai, A. G. Machado, and C. C. McIntyre, "Axonal pathways linked to therapeutic and nontherapeutic outcomes during psychiatric deep brain stimulation," *Hum. Brain Mapp.*, vol. 33, no. 4, pp. 958–968, 2012.
[245] S. N. Sotiropoulos and P. N. Steinmetz, "Assessing the direct effects of deep brain stimulation using embedded axon models," *J Neural Eng*, vol. 4, no. 2, p. 107, 2007.
[246] M. Åström, L. U. Zrinzo, S. Tisch, E. Tripoliti, M. I. Hariz, and K. Wårdell, "Method for patient-specific finite element modeling and simulation of deep brain stimulation," *Med Biol Eng Comput*, vol. 47, no. 1, pp. 21–28, 2009.
[247] J. M. Duarte-Carvajalino, C. Lenglet, J. Xu, E. Yacoub, K. Ugurbil, S. Moeller, L. Carin, and G. Sapiro, "Estimation of the CSA-ODF using Bayesian compressed sensing of multi-shell HARDI," *Magn. Reson. Med.*, vol. 72, no. 5, pp. 1471–1485, 2014.
[248] A. M. Kuncel, S. E. Cooper, and W. M. Grill, "A method to estimate the spatial extent of activation in thalamic deep brain stimulation," *Clin. Neurophysiol.*, vol. 119, no. 9, pp. 2148–2158, 2008.
[249] B. Haslinger, H. Boecker, C. Buchel, J. Vesper, V. M. Tronnier, R. Pfister, F. Alesch, J. R. Moringlane, J. K. Krauss, B. Conrad, M. Schwaiger, and A. O. Ceballos-Baumann, "Differential modulation of subcortical target and cortex during deep brain stimulation," *Neuroimage*, vol. 18, no. 2, pp. 517–24, Feb. 2003.
[250] H. S. Mayberg, A. M. Lozano, V. Voon, H. E. McNeely, D. Seminowicz, C. Hamani, J. M. Schwalb, and S. H. Kennedy, "Deep brain stimulation for treatment-resistant depression," *Neuron*, vol. 45, no. 5, pp. 651–60, Mar. 2005.
[251] T. L. Tattersall, P. G. Stratton, T. J. Coyne, R. Cook, P. Silberstein, P. A. Silburn, F. Windels, and P. Sah, "Imagined gait modulates neuronal network dynamics in the human pedunculopontine nucleus," *Nat. Neurosci.*, vol. 17, no. 3, pp. 449–454, Mar. 2014.
[252] B. Piallat, S. Chabardès, N. Torres, V. Fraix, L. Goetz, E. Seigneuret, E. Bardinet, M. Ferraye, B. Debu, P. Krack, J. Yelnik, P. Pollak, and A. L. Benabid, "Gait is

associated with an increase in tonic firing of the sub-cuneiform nucleus neurons," *Neuroscience*, vol. 158, no. 4, pp. 1201–1205, 2009.
[253] I. Pose, S. Sampogna, M. H. Chase, and F. R. Morales, "Cuneiform Neurons Activated during Cholinergically Induced Active Sleep in the Cat," *J. Neurosci.*, vol. 20, no. 9, pp. 3319–3327, May 2000.
[254] T. Noda and H. Oka, "Distribution and morphology of tegmental neurons receiving nigral inhibitory inputs in the cat: an intracellular HRP study," *J.Comp.Neurol.*, vol. 244, pp. 254–266, 1986.
[255] S. Grillner, L. Cangiano, G. Y. Hu, R. Thompson, R. Hill, and P. Wallén, "The intrinsic function of a motor system — from ion channels to networks and behavior," *Brain Res*, vol. 886, no. 1–2, pp. 224–236, 2000.
[256] S. Grillner, "The motor infrastructure: from ion channels to neuronal networks," *Nat Rev Neurosci*, vol. 4, no. 7, pp. 573–586, 2003.
[257] A. Haghparast, N. Naderi, A. Khani, R. Lashgari, and F. Motamedi, "Formalin-Induced Differential Activation of Nucleus Cuneiformis Neurons in the Rat: An Electrophysiological Study," *J. Pain*, vol. 11, no. 1, pp. 32–43, 2010.
[258] R. M. Zweig, W. R. Jankel, J. C. Hedreen, R. Mayeux, and D. L. Price, "The pedunculopontine nucleus in Parkinson's disease," *Ann Neurol*, vol. 26, no. 1, pp. 41–46, 1989.
[259] G. Frazzitta, R. Maestri, D. Uccellini, G. Bertotti, and P. Abelli, "Rehabilitation treatment of gait in patients with Parkinson's disease with freezing: A comparison between two physical therapy protocols using visual and auditory cues with or without treadmill training," *Mov. Disord.*, vol. 24, no. 8, pp. 1139–1143, Jun. 2009.
[260] M. L. Welter, J. L. Houeto, A. M. Bonnet, P. B. Bejjani, V. Mesnage, D. Dormont, S. Navarro, P. Cornu, Y. Agid, and B. Pidoux, "Effects of high-frequency stimulation on subthalamic neuronal activity in parkinsonian patients," *Arch Neurol*, vol. 61, no. 1, pp. 89–96, Jan. 2004.
[261] A. Samii, M. Lenarz, O. Majdani, H. H. Lim, M. Samii, and T. Lenarz, "Auditory Midbrain Implant: A Combined Approach for Vestibular Schwannoma Surgery and Device Implantation," *Otol. Neurotol.*, vol. 28, no. 1, pp. 31–38, Jan. 2007.
[262] C. J. Van Dort, D. P. Zachs, J. D. Kenny, S. Zheng, R. R. Goldblum, N. A. Gelwan, D. M. Ramos, M. A. Nolan, K. Wang, F.-J. Weng, Y. Lin, M. A. Wilson, and E. N. Brown, "Optogenetic activation of cholinergic neurons in the PPT or LDT induces REM sleep," *Proc. Natl. Acad. Sci. U. S. A.*, vol. 112, no. 2, pp. 584–589, Jan. 2015.
[263] M. Hägglund, L. Borgius, K. J. Dougherty, and O. Kiehn, "Activation of groups of excitatory neurons in the mammalian spinal cord or hindbrain evokes locomotion," *Nat. Neurosci.*, vol. 13, no. 2, pp. 246–252, Feb. 2010.
[264] T. K. Roseberry, A. M. Lee, A. L. Lalive, L. Wilbrecht, A. Bonci, and A. C. Kreitzer, "Cell-Type-Specific Control of Brainstem Locomotor Circuits by Basal Ganglia," *Cell*, vol. 164, no. 3, pp. 526–537, Jan. 2016.
[265] P. Mazzone, F. Stocchi, S. Galati, A. Insola, M. G. Altibrandi, N. Modugno, D. Tropepi, L. Brusa, and A. Stefani, "Bilateral Implantation of Centromedian-Parafascicularis Complex and GPi: A New Combination of Unconventional Targets

for Deep Brain Stimulation in Severe Parkinson Disease," *Neuromodulation Technol. Neural Interface*, vol. 9, no. 3, pp. 221–228, Jul. 2006.

[266] L. Ackermans, Y. Temel, D. Cath, C. van der Linden, R. Bruggeman, M. Kleijer, P. Nederveen, K. Schruers, H. Colle, M. A. Tijssen, and V. Visser-Vandewalle, "Deep brain stimulation in Tourette's syndrome: two targets?," *Mov Disord*, vol. 21, no. 5, pp. 709–13, May 2006.

[267] M. Velasco, F. Velasco, and A. L. Velasco, "Centromedian-thalamic and hippocampal electrical stimulation for the control of intractable epileptic seizures," *J Clin Neurophysiol*, vol. 18, no. 6, pp. 495–513, Nov. 2001.

[268] N. D. Schiff, J. T. Giacino, K. Kalmar, J. D. Victor, K. Baker, M. Gerber, B. Fritz, B. Eisenberg, T. Biondi, J. O'Connor, E. J. Kobylarz, S. Farris, A. Machado, C. McCagg, F. Plum, J. J. Fins, and A. R. Rezai, "Behavioural improvements with thalamic stimulation after severe traumatic brain injury," *Nature*, vol. 448, no. 7153, pp. 600–3, Aug. 2007.

[269] P. Testini, C. Z. Zhao, M. Stead, P. S. Duffy, B. T. Klassen, and K. H. Lee, "Centromedian-Parafascicular Complex Deep Brain Stimulation for Tourette Syndrome: A Retrospective Study," *Mayo Clin. Proc.*, vol. 91, no. 2, pp. 218–225, Feb. 2016.

[270] Castrioto A, Lozano AM, Poon Y, Lang AE, Fallis M, and Moro E, "Ten-year outcome of subthalamic stimulation in parkinson disease: A blinded evaluation," *Arch. Neurol.*, vol. 68, no. 12, pp. 1550–1556, Dec. 2011.

[271] L. M. Zitella, Y. Xiao, B. A. Teplitzky, D. J. Kastl, Y. Duchin, K. B. Baker, J. L. Vitek, G. Adriany, E. Yacoub, N. Harel, and M. D. Johnson, "In Vivo 7T MRI of the Non-Human Primate Brainstem," *PLOS ONE*, vol. 10, no. 5, p. e0127049, May 2015.

[272] A. Varentsova, S. Zhang, and K. Arfanakis, "Development of a high angular resolution diffusion imaging human brain template," *NeuroImage*, vol. 91, pp. 177–186, May 2014.

[273] Y. Kang and S. T. Kitai, "Electrophysiological properties of pedunculopontine neurons and their postsynaptic responses following stimulation of substantia nigra reticulata," *Brain Res*, vol. 535, pp. 79–95, 1990.

[274] P. S. Larson, P. A. Starr, G. Bates, L. Tansey, R. M. Richardson, and A. J. Martin, "An Optimized System for Interventional MRI Guided Stereotactic Surgery: Preliminary Evaluation of Targeting Accuracy," *Neurosurgery*, vol. 70, no. OPERATIVE, pp. ons95–ons103, Mar. 2012.

[275] J.-J. Lemaire, J. Coste, L. Ouchchane, F. Caire, C. Nuti, P. Derost, V. Cristini, J. Gabrillargues, S. Hemm, F. Durif, and J. Chazal, "Brain mapping in stereotactic surgery: a brief overview from the probabilistic targeting to the patient-based anatomic mapping," *NeuroImage*, vol. 37 Suppl 1, pp. S109–115, 2007.

[276] P. A. Starr, J. L. Vitek, M. DeLong, and R. A. Bakay, "Magnetic resonance imaging-based stereotactic localization of the globus pallidus and subthalamic nucleus," *Neurosurgery*, vol. 44, no. 2, pp. 303–13; discussion 313–4, Feb. 1999.

[277] J. Schlaier, P. Schoedel, M. Lange, J. Winkler, J. Warnat, U. Dorenbeck, and A. Brawanski, "Reliability of atlas-derived coordinates in deep brain stimulation," *Acta Neurochir. (Wien)*, vol. 147, no. 11, pp. 1175–1180; discussion 1180, Nov. 2005.
[278] R. M. Levy, S. Lamb, and J. E. Adams, "Treatment of chronic pain by deep brain stimulation: long term follow-up and review of the literature," *Neurosurgery*, vol. 21, no. 6, pp. 885–893, Dec. 1987.
[279] A. L. Benabid, P. Pollak, C. Gervason, D. Hoffmann, D. M. Gao, M. Hommel, J. E. Perret, and J. de Rougemont, "Long-term suppression of tremor by chronic stimulation of the ventral intermediate thalamic nucleus," *Lancet*, vol. 337, no. 8738, pp. 403–6, Feb. 1991.
[280] N. Lipsman, M. L. Schwartz, Y. Huang, L. Lee, T. Sankar, M. Chapman, K. Hynynen, and A. M. Lozano, "MR-guided focused ultrasound thalamotomy for essential tremor: a proof-of-concept study," *Lancet Neurol.*, vol. 12, no. 5, pp. 462–468, May 2013.
[281] K. Takase, H. Shigeto, T. Kamada, Y. Ohyagi, and J. Kira, "Efficacy of mediodorsal thalamic nucleus stimulation in a rat model of cortical seizure," *Fukuoka Igaku Zasshi Hukuoka Acta Medica*, vol. 100, no. 8, pp. 274–280, Aug. 2009.
[282] R. Fisher, V. Salanova, T. Witt, R. Worth, T. Henry, R. Gross, K. Oommen, I. Osorio, J. Nazzaro, D. Labar, M. Kaplitt, M. Sperling, E. Sandok, J. Neal, A. Handforth, J. Stern, A. DeSalles, S. Chung, A. Shetter, D. Bergen, R. Bakay, J. Henderson, J. French, G. Baltuch, W. Rosenfeld, A. Youkilis, W. Marks, P. Garcia, N. Barbaro, N. Fountain, C. Bazil, R. Goodman, G. McKhann, K. Babu Krishnamurthy, S. Papavassiliou, C. Epstein, J. Pollard, L. Tonder, J. Grebin, R. Coffey, N. Graves, and SANTE Study Group, "Electrical stimulation of the anterior nucleus of thalamus for treatment of refractory epilepsy," *Epilepsia*, vol. 51, no. 5, pp. 899–908, May 2010.
[283] V. Visser-Vandewalle, Y. Temel, P. Boon, F. Vreeling, H. Colle, G. Hoogland, H. J. Groenewegen, and C. van der Linden, "Chronic bilateral thalamic stimulation: a new therapeutic approach in intractable Tourette syndrome. Report of three cases," *J Neurosurg*, vol. 99, no. 6, pp. 1094–100, Dec. 2003.
[284] S. G. Ewing, B. Porr, and J. A. Pratt, "Deep brain stimulation of the mediodorsal thalamic nucleus yields increases in the expression of zif-268 but not c-fos in the frontal cortex," *J. Chem. Neuroanat.*, vol. 52, pp. 20–24, Sep. 2013.
[285] J. Klein, R. Hadar, T. Götz, A. Männer, C. Eberhardt, J. Baldassarri, T. T. Schmidt, A. Kupsch, A. Heinz, R. Morgenstern, M. Schneider, I. Weiner, and C. Winter, "Mapping Brain Regions in Which Deep Brain Stimulation Affects Schizophrenia-Like Behavior in Two Rat Models of Schizophrenia," *Brain Stimulat.*, vol. 6, no. 4, pp. 490–499, Jul. 2013.
[286] J. Talairach and P. Tournoux, *Coplanar Stereotaxic Atlas of the Human Brain*. New York, 1988.
[287] M. Krams, M. F. Rushworth, M. P. Deiber, R. S. Frackowiak, and R. E. Passingham, "The preparation, execution and suppression of copied movements in the human brain," *Exp Brain Res*, vol. 120, no. 3, pp. 386–98, 1998.

[288] S. C. Baker, R. D. Rogers, A. M. Owen, C. D. Frith, R. J. Dolan, R. S. J. Frackowiak, and T. W. Robbins, "Neural systems engaged by planning: a PET study of the Tower of London task," *Neuropsychologia*, vol. 34, no. 6, pp. 515–526, Jun. 1996.

[289] M. Samuel, A. O. Ceballos-Baumann, J. Blin, T. Uema, H. Boecker, R. E. Passingham, and D. J. Brooks, "Evidence for lateral premotor and parietal overactivity in Parkinson's disease during sequential and bimanual movements. A PET study," *Brain*, vol. 120 (Pt 6), pp. 963–76, Jun. 1997.

[290] K. D. Davis, C. L. Kwan, A. P. Crawley, and D. J. Mikulis, "Functional MRI study of thalamic and cortical activations evoked by cutaneous heat, cold, and tactile stimuli," *J. Neurophysiol.*, vol. 80, no. 3, pp. 1533–1546, Sep. 1998.

[291] F. Calamante, J.-D. Tournier, N. D. Kurniawan, Z. Yang, E. Gyengesi, G. J. Galloway, D. C. Reutens, and A. Connelly, "Super-resolution track-density imaging studies of mouse brain: comparison to histology," *NeuroImage*, vol. 59, no. 1, pp. 286–296, Jan. 2012.

[292] F. Calamante, S.-H. Oh, J.-D. Tournier, S.-Y. Park, Y.-D. Son, J.-Y. Chung, J.-G. Chi, G. D. Jackson, C.-W. Park, Y.-B. Kim, A. Connelly, and Z.-H. Cho, "Super-resolution track-density imaging of thalamic substructures: comparison with high-resolution anatomical magnetic resonance imaging at 7.0T," *Hum. Brain Mapp.*, vol. 34, no. 10, pp. 2538–2548, Oct. 2013.

[293] T. Tourdias, M. Saranathan, I. R. Levesque, J. Su, and B. K. Rutt, "Visualization of intra-thalamic nuclei with optimized white-matter-nulled MPRAGE at 7T," *NeuroImage*, vol. 84, pp. 534–545, Jan. 2014.

[294] T. E. Behrens, H. Johansen-Berg, M. W. Woolrich, S. M. Smith, C. A. Wheeler-Kingshott, P. A. Boulby, G. J. Barker, E. L. Sillery, K. Sheehan, O. Ciccarelli, A. J. Thompson, J. M. Brady, and P. M. Matthews, "Non-invasive mapping of connections between human thalamus and cortex using diffusion imaging," *Nat. Neurosci.*, vol. 6, no. 7, pp. 750–7, Jul. 2003.

[295] H. Johansen-Berg, T. E. J. Behrens, E. Sillery, O. Ciccarelli, A. J. Thompson, S. M. Smith, and P. M. Matthews, "Functional-anatomical validation and individual variation of diffusion tractography-based segmentation of the human thalamus," *Cereb. Cortex N. Y. N 1991*, vol. 15, no. 1, pp. 31–39, Jan. 2005.

[296] T. Gringel, W. Schulz-Schaeffer, E. Elolf, A. Frölich, P. Dechent, and G. Helms, "Optimized high-resolution mapping of magnetization transfer (MT) at 3 Tesla for direct visualization of substructures of the human thalamus in clinically feasible measurement time," *J. Magn. Reson. Imaging JMRI*, vol. 29, no. 6, pp. 1285–1292, Jun. 2009.

[297] S. C. L. Deoni, M. J. C. Josseau, B. K. Rutt, and T. M. Peters, "Visualization of thalamic nuclei on high resolution, multi-averaged T1 and T2 maps acquired at 1.5 T," *Hum. Brain Mapp.*, vol. 25, no. 3, pp. 353–359, Jul. 2005.

[298] R. Deriche, J. Calder, and M. Descoteaux, "Optimal real-time Q-ball imaging using regularized Kalman filtering with incremental orientation sets," *Med. Image Anal.*, vol. 13, no. 4, pp. 564–579, Aug. 2009.

[299] M. N. Gallay, D. Jeanmonod, J. Liu, and A. Morel, “Human pallidothalamic and cerebellothalamic tracts: anatomical basis for functional stereotactic neurosurgery,” *Brain Struct. Funct.*, vol. 212, no. 6, pp. 443–463, Aug. 2008.

[300] J. Anthofer, K. Steib, C. Fellner, M. Lange, A. Brawanski, and J. Schlaier, “The variability of atlas-based targets in relation to surrounding major fibre tracts in thalamic deep brain stimulation,” *Acta Neurochir Suppl*, pp. 1–8, May 2014.

[301] E. Zakszewski, N. Adluru, D. P. M. Tromp, N. Kalin, and A. L. Alexander, “A diffusion-tensor-based white matter atlas for rhesus macaques,” *PloS One*, vol. 9, no. 9, p. e107398, 2014.

[302] J. D. Schmahmann and D. N. Pandya, *Fiber pathways of the brain*. Oxford ; New York: Oxford University Press, 2006.

6 Appendix I: Gait analysis in NHP

6.1 Introduction

Deep brain stimulation in the PPN area is posited to improve gait and balance symptoms of Parkinson's disease; however, clinical trials have historically had mixed results. This study aimed to use kinematic gait data to determine the differences in gait kinematics in one NHP during PPN area stimulation. The intention of this study was to utilize the computational models described in this thesis to provide pre-operative guidance for DBS lead implantation and stimulation settings and retrograde analysis of the effects of stimulation. While differences in gait were present in this animal when the normal and PD states were compared, no consistent therapeutic effect was seen during stimulation for reasons documented below. The methods and results of this study are reported here to inform future studies of DBS for gait in the NHP.

6.2 Methods

6.2.1 Subject

One NHP, Monkey L, was implanted unilaterally in the PPN area of the right hemisphere with an 8-contact DBS lead (Figure 25a). Systemic injections of MPTP were administered until severe parkinsonian symptoms were present. Pre-operative high-field 7T MRI was acquired prior to lead implantation. After lead implantation, post-operative CT was performed. The SWI MRI was then co-registered to the CT to visualize the implantation trajectory (See Chapters 3 and 4). At the conclusion of the study, the animal was deeply anesthetized and perfused with a fixative solution. The brain was reconstructed from histological images to obtain the lead location (See Chapter 4).

6.2.2 Computational Models

Two sets of computational models were developed to predict the activation of nuclei within the PPN and surrounding fiber pathways. The first model utilized the lead location in the brainstem determined from high-field imaging. The warping algorithm described in Chapter 3 was used to create the subject-specific geometry of PPN and a few fiber pathways, including the SCP, ML, and LL (Figure 25b). Type I and Type II cells were oriented and placed in the PPN, as described previously in Chapter 2 (Figure 25c-d). The voltage distribution in the tissue was calculated using an FEM model of the 8-contact DBS lead and surrounding isotropic conductivity neural tissue. Percent activation of axons and cells was calculated as the lowest stimulation amplitude between 0 and 8 V (30 Hz, 90 μs pulse width) that elicited one or more action potentials for at least 80% of the stimulus pulses. Detailed methods of the computational models are described in Chapter 2.

A retrospective model was later created that utilized the reconstructed histological images to determine the lead location. Additionally, probabilistic diffusion tractography was used to define the geometry of the fiber pathways (See Chapter 3 and 4). Again, both Type I and Type II PPN cells were included in the model (Figure 25). A FEM model of the 8-

contact lead was developed to accurately model the current-controlled stimulation (20 Hz, 90 µs pulse width) that was applied experimentally (See Chapter 4).

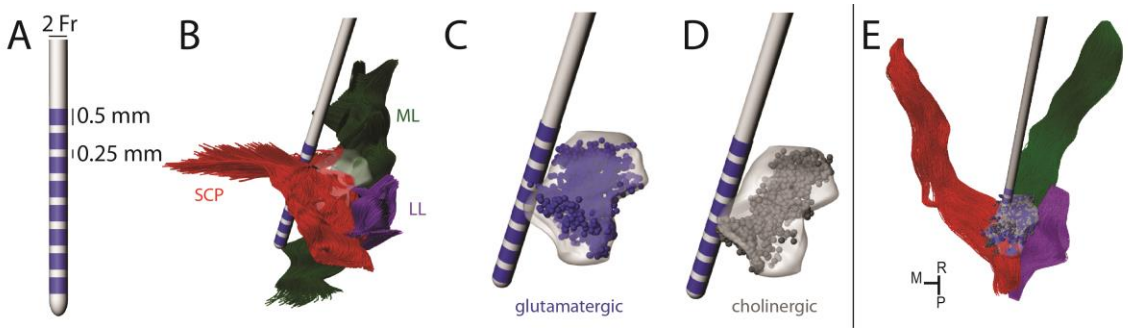

Figure 25. Computational model geometries, based upon imaging and histology.
(A) Spatial dimensions of the 8-contact DBS lead implanted in the NHP. (B) Imaging-based model geometry, including the fiber pathways surrounding PPN (gray), SCP (red), LL (purple), and ML (green). (C) Glutamatergic and (D) Cholinergic modeled PPN cell distribution. (E) Histology-based model geometry.

6.2.3 Data Collection

An enclosed treadmill is surrounded by eight infrared cameras. Twelve reflective markers are placed on the wrist, elbow, shoulder, ankle, knee, and hip joints of an NHP (Figure 26). Joint locations in space and time are constantly monitored through Motion Analysis Cortex software and saved for future analysis. Prior to DBS implantation, normal gait data was collected from Monkey L at varying speeds of 0.6, 0.9, and 1.2 miles/hour. After DBS implantation and MPTP injections, five days of treadmill gait data were collected with the following protocol.

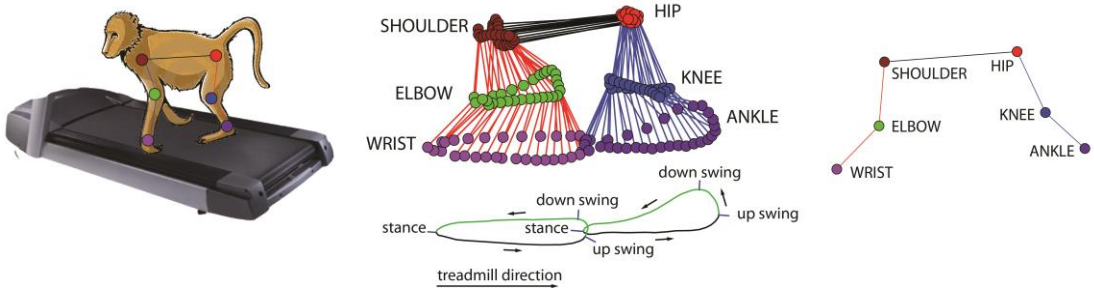

Figure 26. Treadmill data collection
Monkey L walked on treadmill surrounded by motion capture cameras with markers on 12 joints.

No levodopa was given the morning of data collection. Since the Boston Scientific IPG was not implanted, it was attached to the DBS lead and taped to the chamber. All chambers and the IPG were covered with tape to avoid detection by the cameras. Five stimulation settings and three treadmill speeds (0.6, 0.9, and 1.2 miles/hour) were pseudo-randomly tested each day for one minute. There was a five minute resting period between each stimulation setting. Stimulation settings tested (20 Hz, 90 µs pulse width) included DBS OFF, 0.9 mA through Contact 7, 0.9 mA through Contact 6, 1.2 mA through Contact 5, and 1.2 mA through Contact 4. These stimulation settings were

chosen based on the prospective computational models and to be sub-threshold of the visually observed motor side effect thresholds.

6.2.4 Data Analysis

Data files output from each trial included frame number, time point and 3-D coordinates of each point picked up by the cameras. These files were imported into Cortex software for scrubbing and interpolation. The sensitivity of the infrared cameras allowed for errant signals, such as glares, to be detected as points. Therefore the data was scrubbed to correctly identify the proper points as joints in each time frame. A template, an example of normal gait with markers labels, was used as a starting point by applying the Template Rectify command, but manual identification was sometimes necessary when many points were missing. Once the markers were labeled to satisfaction, the points for each joint were interpolated to fill in any time points when the location was not recorded. This is done for all sequences of normal gait (i.e. not standing up, turning around, etc.). These processed normal gait frames were then trimmed and saved for further analysis.

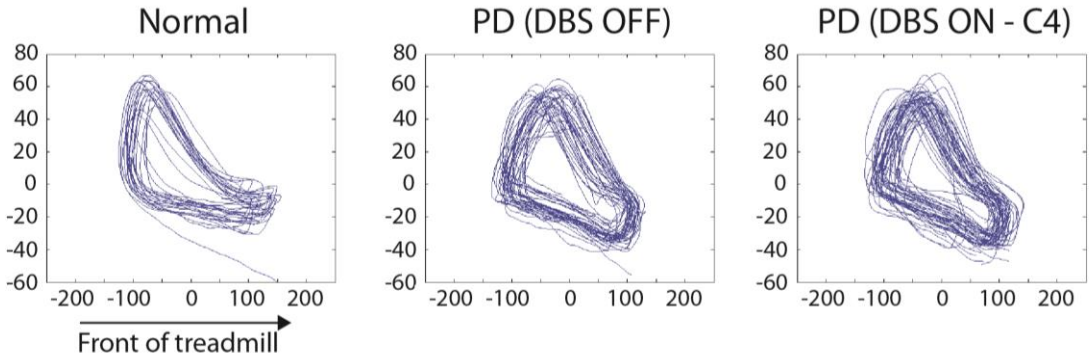

Figure 27. Examples of gait cycles.
Right ankle gait cycles during 0.9 mph treadmill gait in the normal (left), parkinsonian with no DBS (middle), and parkinsonian with monopolar stimulation through contact 4 (right) conditions.

The processed gait frames were then imported in MATLAB to determine the similarities and differences in gait between the normal, parkinsonian, and parkinsonian with DBS states. The X, Y, and Z data was first filtered with a 10^{th} order butterworth band-pass filter which passed frequencies between 0.005 and 0.3 based on a sampling frequency of 100 Hz. First, each gait cycle was identified based on the wrist and ankle joints so that different parameters could be calculated for each cycle (Figure 27). The gait cycle was divided into four different components: the start of the swing phase, the peak height at the end of the up swing, the peak height at the end of the down swing, and the start of the stance phase. The start of the swing phase was calculated as the first point where velocity was zero or close to zero before Z reached a minimum (where Z was the direction of forward motion). The maximum and minimum heights of each joint (Y direction) were calculated and used to define the peak heights at the end of the up swing and at the end of the down swing. These values were the same except for the last gait cycle, where there was only a peak height at the end of the up swing defined. These gait cycle time stamps were then used to calculate a multitude of gait cycle parameters including the stride

length, the stride length during the upswing, the peak velocity during the up swing, the peak velocity during the down swing, the mean velocity during the up and down swing, the time of the up swing and down swing, the stance time, the change in height during the up swing and down swing, and the maximum and minimum joint angles. These parameters were calculated for each joint for the normal, parkinsonian (DBS OFF), and all parkinsonian (DBS ON) cases.

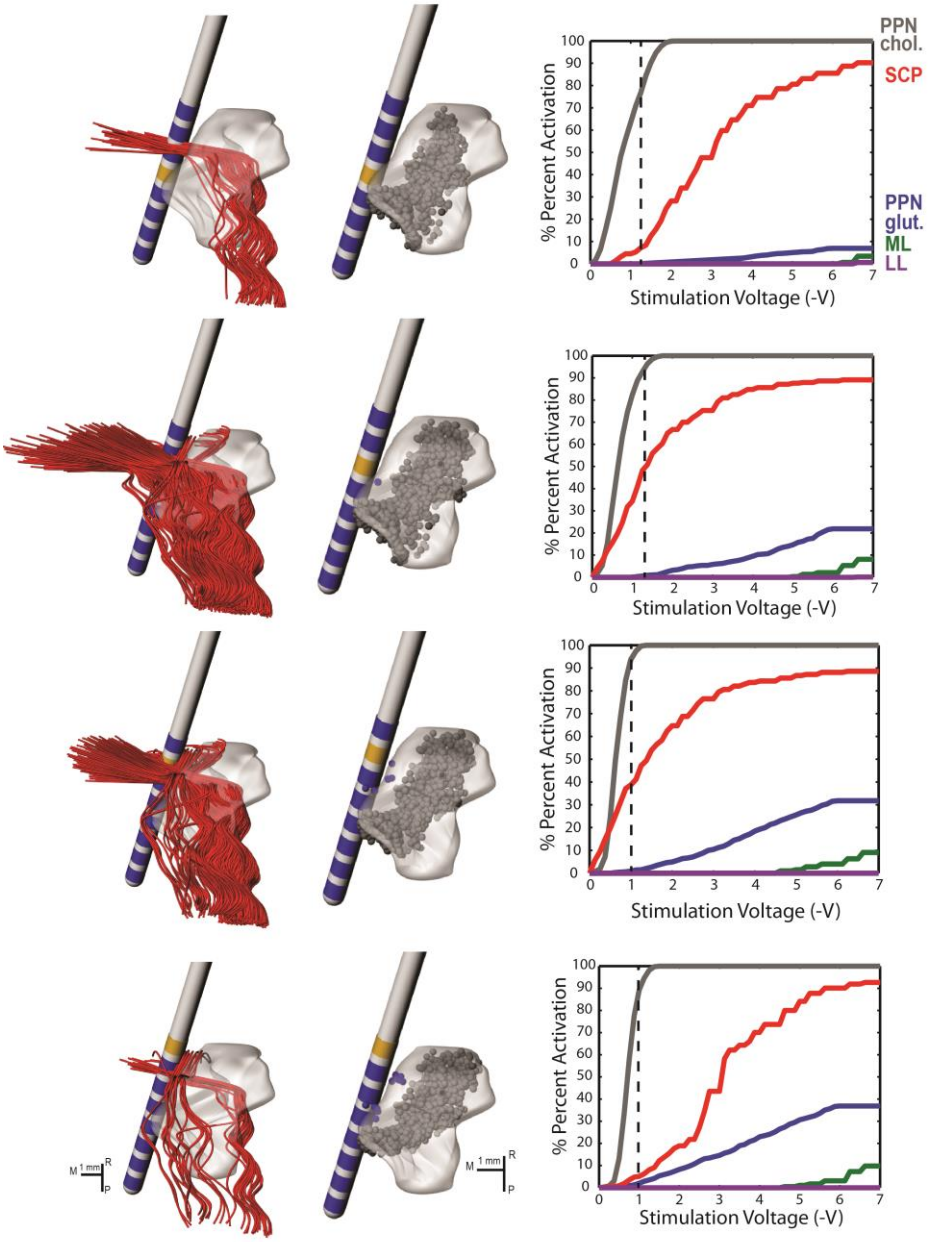

Figure 28. Prediction of fibers and cells activated.
(Right) Predicted percent activation for monopolar stimulation from 0-7 V. (Left) The activated fiber pathways and cells during -1.2 V cathodic monopolar stimulation through Contact 4 and Contact 5 and -0.9 V stimulation through Contact 6 and Contact 7.

6.3 Results

6.3.1 Prospective Modeling Results

Due to time constraints, simulations of voltage-controlled stimulation in the PPN area were used in combination with side effect thresholds to determine the stimulation settings to test during gait. The models predicted the highest activation of PPN cells with monopolar stimulation through contacts 4-7 (contacts 0-3 not shown). Based on the results of the models and the side effect thresholds (1.4 mA in contacts 4 and 5, 1.1 mA in contact 6, and 1.0 mA in contact 7), gait was evaluated during sub-threshold stimulation levels of 1.2 mA in contacts 4 and 5 and 0.9 mA in contacts 6 and 7 (denoted by the vertical dashed line in Figure 28). The models assumed an impedance value of 1 kΩ. Stimulation through contact 7 at 0.9 mA was predictably the most therapeutic, with the highest percent activation of PPN cells and the lowest percent activation of SCP.

6.3.2 Gait Analysis Results

As shown in Figure 29, stance time was found to increase in the parkinsonian state. While no DBS stimulation setting reduced stance time back to baseline consistently, some stimulation settings increased stance time or effected no change. The most promising stimulation setting was contact 7. Due to slower gait and the signature shuffling of step seen in parkinsonian patients, the stance time parameter was expected to increase in the parkinsonian state and decrease with therapeutic stimulation.

Similar results were obtained when evaluating the maximum angle of the knee joint. This joint displayed the most rigidity in the parkinsonian state; therefore the maximum angle was expected to decrease due to rigidity symptoms. Again stimulation through contact 7 was the most promising setting, but no stimulation setting tested produced observable therapeutic effects (Figure 30). Again due to rigidity, the peak velocity in the down swing is expected to decrease in the parkinsonian state. This difference was seen between the normal and parkinsonian states, but no DBS stimulation setting provided consistently significant improvement in this parameter (Figure 31).

6.3.3 Retrospective Model Results

Retrospective computational models utilized both current-controlled stimulation and histology-based lead location. These models predicted that monopolar cathodic stimulation through contact 4 activated the highest percentage of both glutamatergic and cholinergic PPN cells (Figure 32). The model-predicted activation of select fiber pathways is described in Chapter 4.

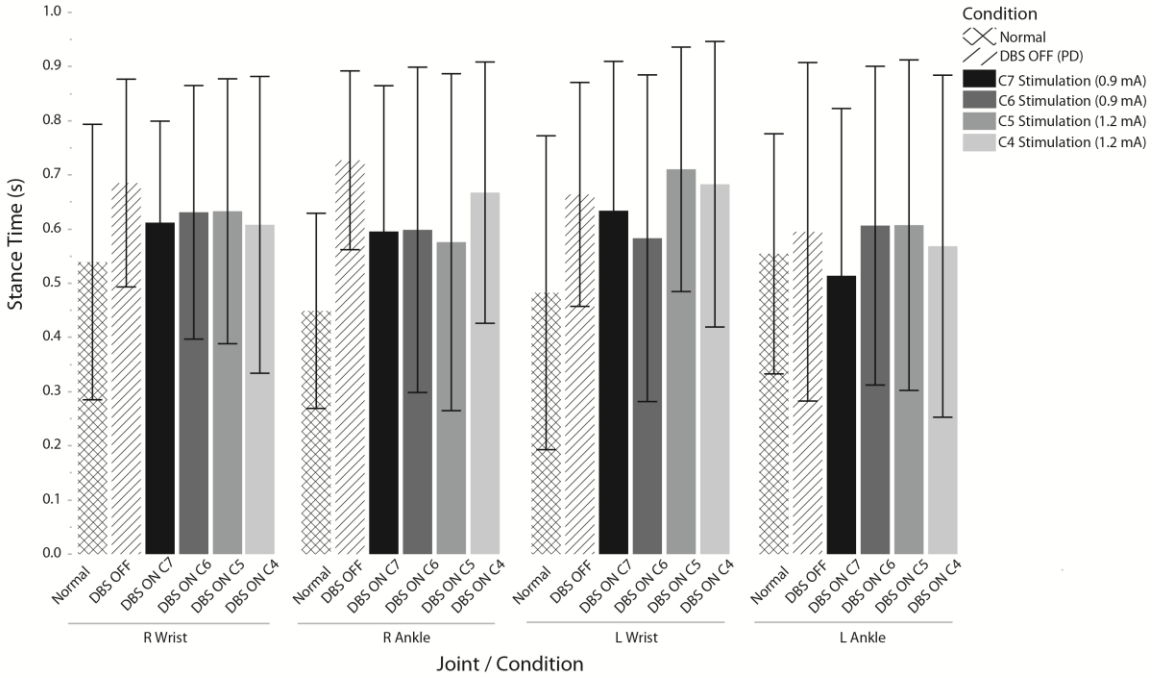

Figure 29. The effects of DBS on stance time during treadmill gait.
Stance time is measured in the normal, parkinsonian (DBS OFF), and DBS ON state. Four different stimulation parameters were tested. The values for the wrists and ankles are shown here (mean ± standard deviation).

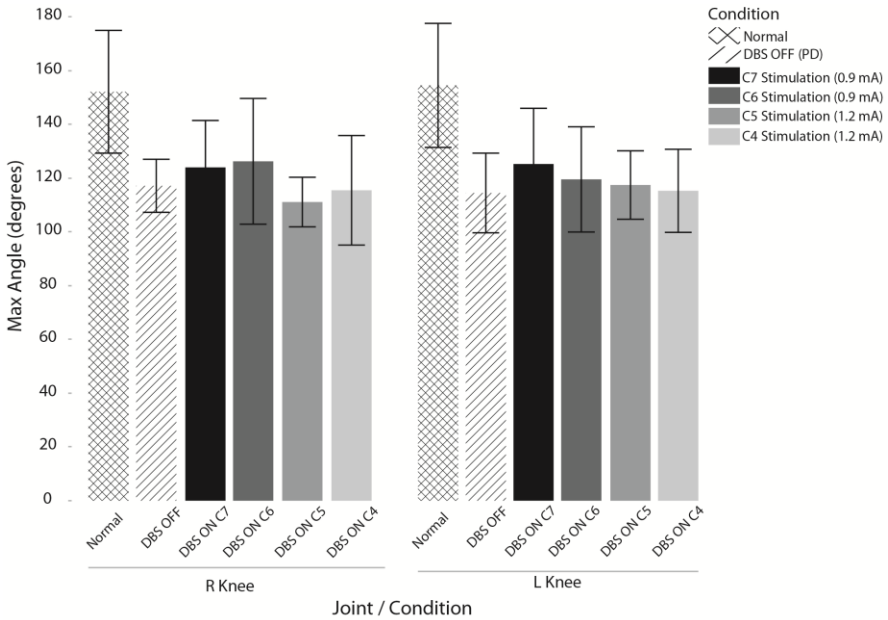

Figure 30. The effects of DBS on maximum angle during treadmill gait.
Maximum knee angle is measured in the normal, parkinsonian (DBS OFF), and DBS ON state. Four different stimulation parameters were tested. The values for the knees are shown here (mean ± standard deviation).

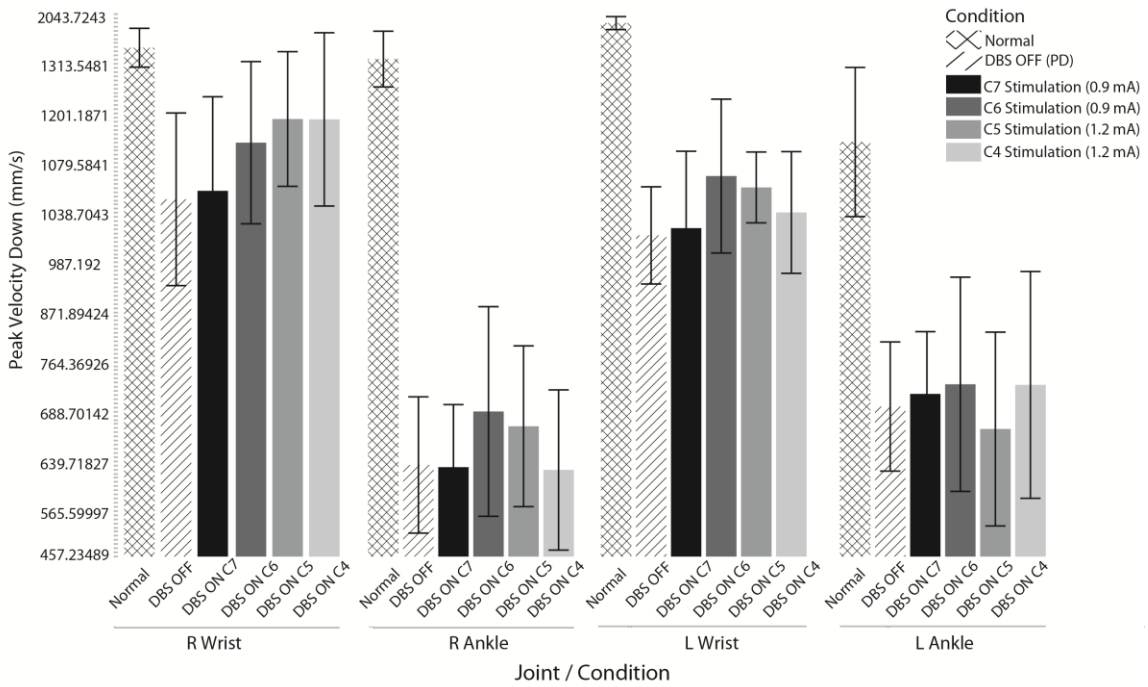

Figure 31. The effects of DBS on peak velocity in the down swing during treadmill gait.
Peak velocity in the down swing is measured in the normal, parkinsonian (DBS OFF), and DBS ON state. Four different stimulation parameters were tested. The values for the ankles and wrists are shown here (mean ± standard deviation).

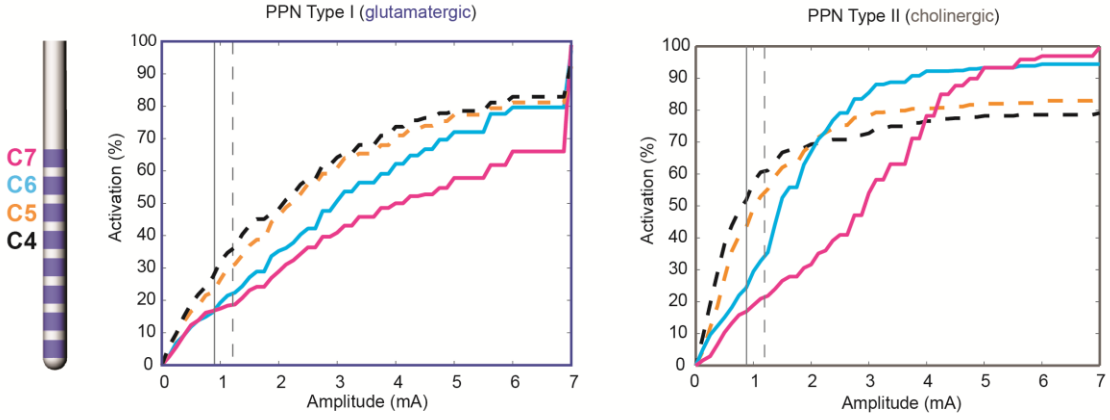

Figure 32. Model-predicted activation of PPN Type I and Type II cells during monopolar stimulation.
(Left) The geometry of the 8-contact lead is shown, with the contacts used for stimulation labeled.C4 (black), C5 (orange), C6 (light blue), C7 (pink). (Right) Percent activation is plotted for monopolar stimulation through each contact for stimulation amplitudes between 0-7 mA. The experimental stimulation amplitudes used are shown in each plot as a dashed line (1.2 mA for C4 and C5) and a solid line (0.9 mA for C6 and C7).

6.4 Discussion

While some stimulation settings improved certain parameters of gait, no stimulation setting produced a visible improvement in overall locomotion. This lack of improvement

could be due to the lead placement on the medial edge of PPN or the use of a treadmill to investigate gait. Perhaps there were improvements in freezing of gait that were not measureable due to the constant cue of the treadmill. Future studies will investigate the effects of DBS while walking freely instead of using a treadmill in hopes to examine freezing of gait.

Additionally, there are modifications that should be made to the modeling pipeline. All of the models in this study assumed isotropic conductivity neural tissue, which was shown in Chapter 4 to be extremely inaccurate compared to anisotropic conductivity neural tissue models when predicting the activation of fiber pathways. The prospective models were also voltage-controlled and modeled using 30 Hz stimulation, contrary to the current-controlled, 20 Hz stimulation frequency used in the experiments. The impedance assumption was also inaccurate, as the measured impedances were later found to be 2.3 kΩ in contact 7, 2.5 kΩ in contact 6, 2.0 kΩ in contact 5, and 2.1 kΩ in contact 4. Additionally, the histological lead location was slightly more lateral than the imaging-based lead location. The results of this study are further confounded by the presence of gliosis surrounding the DBS lead, discovered on the histological slices.

7 Appendix II: Subject-specific Human PPN DBS models

7.1 Introduction

This thesis describes the development of computational models of DBS in the brainstem (Chapter 2). These models can be used to guide lead implantation, select stimulation parameters, and understand the experimental results. The original model geometry was based upon atlases of the NHP and human until a new pipeline allowed for the extraction of 3D anatomical information from MRI (Chapter 3) [271]. This was used to develop subject-specific computational models of DBS in the brainstem of NHPs (Chapter 4). Here, a similar pipeline was applied to patient data from one human subject who was implanted in the PPN and experienced a therapeutic effect. Based on post-operative imaging, PPN cells and surrounding fiber tracts were modeled in relation to each subject-specific lead placement. Results were compared between two subjects that experienced therapy to determine guidelines for future implantations.

7.2 Methods

7.2.1 Subjects

One patient, diagnosed with parasupranuclear palsy, was implanted in the PPN area with the Medtronic 3389 DBS lead. Post-implantation 1.0 T T1 MRI images were obtained in order to visualize the location of the DBS lead. During bipolar stimulation (25 Hz, 60 μs), significant effects on gait and posture were seen, based on UPDRS III clinician motor ratings and the Hoehn and Yahr disability scale [78]. Since no diffusion-weighted imaging was collected for this patient, a diffusion imaging template was used, that is composed of 67 healthy human subjects' data and aligned in ICBM-152 space [272].

7.2.2 Subject-specific geometry

Subject-specific geometry of the PPN and surrounding fiber tracts was extracted from the low resolution T1 MRI images using the method of atlas warping, as defined previously (Chapter 3). The traditional method of warping an atlas to an MRI involved aligning and re-slicing the MRI to match identical slices of the MRI to the atlas slices. Since the final geometry for these models must be in the same orientation as the diffusion-weighted imaging in order to align with the finite element model, the traditional method of warping an atlas to the MRI was not feasible. A new method for subject-specific visualization of brainstem structures was created in which the atlas was re-sliced to exactly match the MRI, creating a subject-specific atlas.

7.2.2.1 MRI Image Alignment

First, the MRI data was aligned to diffusion space using the FLIRT linear registration tool in FSL. The patient's brain was extracted from the MRI using the BET brain extraction tool and aligned using FLIRT to the MNI atlas with 2 mm spacing (that is in the same space as the DTI atlas). Alignment to the DTI atlas was verified visually by overlaying the eigenvectors of the DTI atlas on top of the registered MRI in FSLView.

7.2.2.2 Atlas preparation

To prepare for re-slicing the atlas, each image from the Paxinos and Huang human brainstem atlas was cropped and accurately scaled in MATLAB [16]. These slices were then imported as background bitmap images into Rhino at 1 mm intervals. The InterpCrv command was used to outline over 60 brainstem structures of interest, including the outside border. Each individual structure was lofted into a 3D object. Using the Cutplane and Section commands, the 3D atlas was then re-sliced to match the slice angles of the MRI and saved as a .jpg image with a white background for warping. The structures of interest were labelled on these images to assist with warping, including: ML, LL, SCP, PPN, SPTh, CTG, MLF, cerebral aqueduct, substantia nigra (SN), and RN.

7.2.2.3 Warping

Each MRI slice that matched an atlas slice exactly was cropped around the brainstem in Mimics for warping. The warping algorithm was then run in MATLAB, as described previously in Chapter 3. Briefly, control points were placed around the outside border and visible internal structures on each atlas slice. Corresponding control points were then placed on each MRI slice. The warping script applied a nonlinear warping algorithm without foldback to alter the standard atlas slice to match the MRI slice. The output atlas slice was overlaid on the MRI to verify accuracy. Contours from each slice were then lofted to created subject-specific 3D volumes of brainstem structures in Rhinoceros for use as the model geometry (Figure 33). Correct proportions were maintained in Rhinoceros using the scale bar that was calculated and printed on the images in the final steps of the warping algorithm.

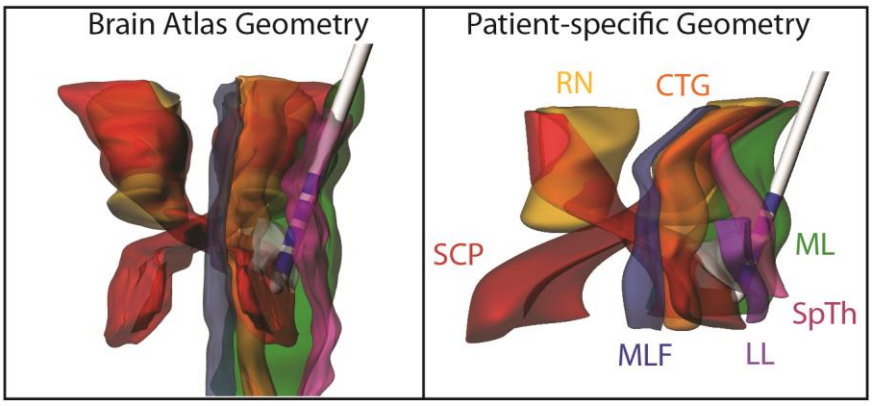

Figure 33. Subject-specific geometry compared to atlas geometry.
(Left) A selection of the lofted human brain atlas geometries. (Right) Patient-specific nuclei and axons after warping. PPN (grey), central tegmental tract (orange), lateral lemniscus (purple), medial lemniscus (green), medial longitudinal fasciculus (blue), red nucleus (yellow), spinothalamic tract (pink), and superior cerebellar peduncle (red).

7.2.3 Axon and PPN Cell Models

The previously generated contours were used to build the geometry of each axon. Each contour slice was randomly populated with seed points and connected using a Jordan

curve algorithm. To avoid sharp curves in the axons, 3000 seed points were placed for 1000 axons. Each 2 micron diameter axon was divided into a multi-compartment axon model containing repeating patterns of four types of pre-defined length segments connected through axial resistance: NODE (node of Ranvier), MYSA (myelin attachment segments), FLUT (paranode main segments), STIN (internode segments). Axonal membrane dynamics in NEURON were consistent with previous studies [107]–[109], [122], [123], [186].

Cholinergic PPN type II cells were also modeled, 1154 in total. The geometry and morphology was consistent with previous studies [36], [40], [125], [186], [273]. The cell geometry, based on camera lucida drawings [36], were placed within the lofted PPN volume based on histological soma locations [26]. These soma location slices were placed within the PPN volume and spread to encompass the entire volume. Axons were positioned to project in the direction of the thalamus, substantia nigra, brainstem, and spinal cord. Axonal processes were modeled in the same myelinated, double-cable structure as discussed above, without synaptic dynamics. Ten stimulation pulses were applied to determine the threshold voltage or the amplitude when at least 8 stimulation pulses (or 80%) produce an action potential.

7.2.4 Finite element models

MRI images aligned to the MNI atlas were imported into Mimics to determine the DBS lead trajectory. A mask was created over the artifact, a visible dark contrast area on each slice of the MRI, and interpolated into a 3-D mask. An STL file of the DBS lead was imported into Mimics and aligned with this mask. This aligned DBS lead was then saved and imported into both Rhino for viewing along with the subject-specific geometry and COMSOL for developing the subject-specific finite element model.

In COMSOL, the lead location was used to properly orient the model DBS lead, a Medtronic 3389 lead (four 1.5 mm height contacts with 0.5 mm spacing). This model lead was translated and rotated until it aligned with the subject-specific lead orientation. A .25 mm encapsulation tissue layer and a 50 mm radius sphere of anisotropic neural tissue surrounded the lead. Four bipolar stimulation parameters were tested, based on clinical stimulation settings [78]. To mimic the clinical settings, the model cathodes were set as a cathode, while the anodes were set to ground.

Anisotropic tissue conductivity maps were calculated in MATLAB from the DTI atlas diffusion eigenvalues and eigenvectors based on the linear relationship between diffusion tensor eigenvalues and conductivity derived by Tuch et al [227], with a scaling factor of 0.844. These values were imported into COMSOL as an interpolation function, with each column representing a directional component of the conductivity (xx, xy, xz, yy,yz, zz), and set as the electrical conductivity material property of the anisotropic brain tissue. Material parameters for all other objects were consistent with previous models. An extremely-fine mesh (as defined by COMSOL) was set to avoid errors in interpolation.

7.3 Results

7.3.1 Fiber pathways modulated

These subject-specific computational models predicted the activation of six fiber pathways during four different stimulation settings. The pathways studied included the CTG, LL, ML, MLF, SCP, and SPTh. Stimulation settings included four bipolar stimulation settings (Table 11, Figure 34). Stimulation was applied at two different frequencies, 25 Hz and 40 Hz with 60 μs pulse widths, however no significant differences in predicted activation thresholds were found. Therefore, reported results are from simulations using 25 Hz stimulation frequency.

Stimulation Setting	*Cathode*	*Anode*	*Frequency (Hz)*	*Pulse Width (μs)*
1	Contact 1	Contact 2	25, 40	60
2	Contact 0	Contact 3	25, 40	60
3	Contact 1	Contact 3	25, 40	60
4	Contact 0	Contact 1	25, 40	60

Table 11. Stimulation settings modeled in both patients.

In the models, none of the stimulation settings, applied up to 10 V, predicted any activation of CTG, MLF, or SCP. All stimulation settings predicted less than 20 percent activation of ML, with the lowest activation of ML during stimulation setting 4 (maximum of 0.5% activation at 10 V). Contrarily, stimulation setting 4 and stimulation setting 2 elicited the highest prediction of activation of LL, up to 75% at 10 V. SPTh activation was predicted to be highest with stimulation settings 1 and 2, with up to 76% activation at 10V.

Initially the therapeutic stimulation setting was stimulation setting 1 (25 Hz, 60 μs pulse width) applied with an amplitude of 2 V. After 3 months the amplitude was increased to 4.5 V, which was constant through 8 months of follow-up. At this clinical setting, 56.4% of SPTh axons, 8.8% of ML axons, and 0.5% of LL axons were predicted to be activated (Figure 34).

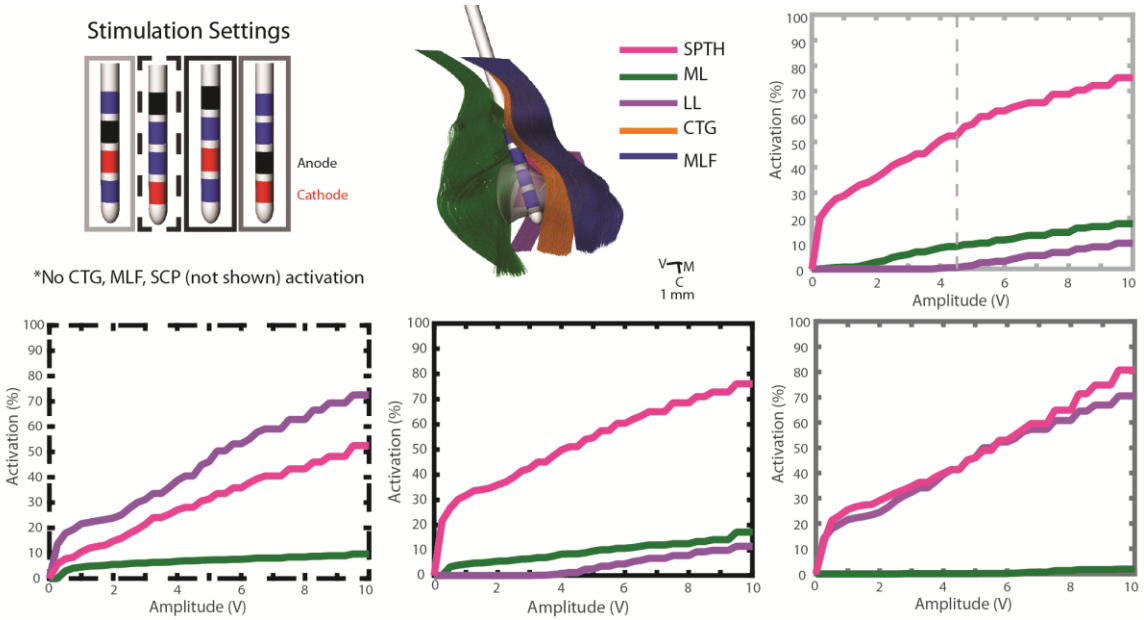

Figure 34. Computational models results of fiber tract stimulation.
Activation threshold curves are shown for three fiber tracts surrounding PPN: the spinothalamic tract (SPTh), medial lemniscus (ML), and lateral lemniscus (LL). No activation was elicited in the models for the central tegmental tract (CTG), medial longitudinal fasciculus (MLF), and superior cerebellar peduncle (SCP). Four different stimulation settings were tested (upper left) with the results shown here. The clinical setting for Subject 1 was bipolar stimulation through contact 1 (cathode) and contact 2 (anode). Results for this simulation are shown in light gray, with the clinical amplitude setting demarcated by the light gray dashed line. In the center, the geometry of all modeled axons (except SCP) are shown in relation to PPN (gray) and the DBS lead.

7.3.2 PPN cell activation

Computational models predicted the activation of cholinergic PPN cells. These cells were divided into two populations, rostral and caudal. Activation was again predicted during the same four bipolar stimulation settings. Again, no significant different was seen between the results of 25 Hz and 40 Hz stimulation, so the results of 25 Hz stimulation are reported here.

The models predicted a higher activation of rostral PPN cells when applying stimulation settings 1 and 4. On the contrary, higher activation of caudal PPN cells was predicted when applying stimulation settings 2 and 3. At the therapeutic stimulation amplitude of 4.5 V, 68.86%, 88.55%, 94.28%, and 54.2% of rostral PPN cells were predicted to be activated at stimulation settings 1, 2, 3, and 4, respectively. At the same amplitude, caudal PPN cells were predicted to be activated 33.95%, 94.45%, 50.59%, and 86.39% when 4.5 V was applied through stimulation setting 1, 2, 3, and 4. Most importantly, when comparing the predicted activation from the therapeutic stimulation setting 1, more cells were activated in rostral PPN compared to caudal PPN (Figure 35).

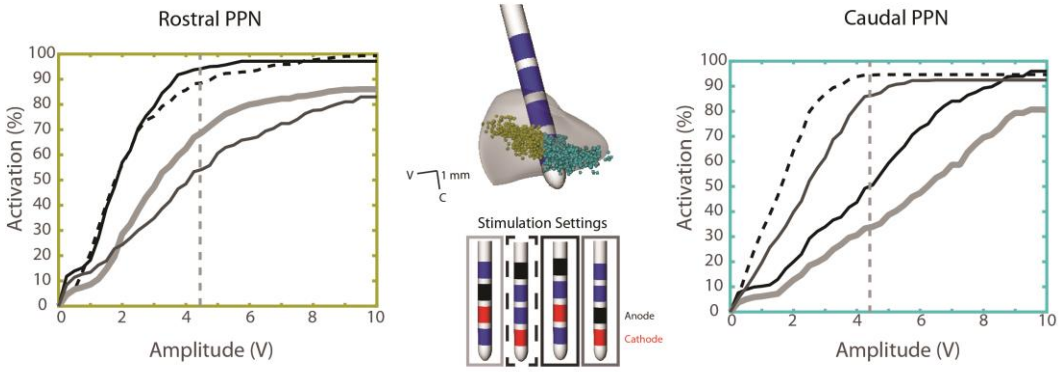

Figure 35. Computational model results of PPN cholinergic cell stimulation.
Activation threshold curves are shown for two groups of PPN type II (cholinergic) cells. The cells were divided into rostral (yellow) and caudal (cyan) populations. Four different stimulation settings were modeled (center) with results shown here. The clinical setting for Subject 1 was bipolar stimulation through contact 1 (cathode) and contact 2 (anode), denoted in light gray, with the final clinical amplitude setting demarcated by the vertical light gray dashed line.

7.4 Discussion

Computational models of DBS are a useful tool to explore the mechanisms of DBS in the brainstem. By modeling cells in the therapeutic and side effect regions, information can be obtained regarding which structures are responsible for each outcome. In this paper, subject-specific models were created for two subjects who received therapeutic benefit in regards to gait and balance symptoms of Parkinson's disease.

A possible mechanism for therapy is the greater activation of rostral cholinergic PPN cells as opposed to caudal cells. This would mean that the lead was activating the cells within PPNd more than those within PPNc. Although they weren't modeled, the lead location within PPNd could imply that the activation of glutamatergic or combination cholinergic/glutamatergic cells within PPNd were more important for therapy. The cell population was split into the rostral and caudal cells in an attempt to separate these two functional populations. It is interesting to note that other stimulation settings that had higher activation of both caudal and rostral PPN cells (stimulation setting 2) were not chosen. This may be due to a side effect from a higher activation of the lateral lemniscus as well. Also, stimulation setting 3 was not chosen, which activated comparable side effect fiber pathways and even greater rostral PPN cells. However, a higher amount of caudal PPN cells were activated. Degeneration of the cholinergic cells in this region (PPNc) is not included in these models, which could affect the analysis.

Activation of fiber pathways is highly dependent on lead location. In this case, the lead was closest to the SPTh, ML, and LL. Since the lead was located in the rostrolateral portion of PPN, CTG, MLF, and SCP, more medial and caudal tracks, were out of the target range of the stimulation. More superior contact configurations (Stimulation settings 1, 2, and 3) were more likely to activate ML, though only marginally, as only the very lateral portion of ML was close enough to the lead to be activated. More inferior contact

configurations, where Contact 0 was a cathode, were more likely to activate a higher percentage of LL axons since contact 0 was located directly medial of LL. SPTh was activated for all stimulation settings, though settings with Contact 1 set as a cathode activated the highest percentage. This makes sense since SPTh runs directly lateral and caudal of Contact 1.

The clinical stimulation setting (Stimulation setting 1) activated 39.2% of SPTh axons at the original amplitude of 2 V and 56.4% of SPTh axons at the final amplitude of 4.5 V. This substantial amount of activation would have most likely caused a side effect. Side effects of SPTh stimulation include change in temperature sensation. Only 2.3% of ML axons were activated at 2V and 8.8% at 4.5 V, which were most likely below the threshold for eliciting paresthesias. Unfortunately, clinician notes were not available to confirm these side effects. It is interesting to note the increase in stimulation amplitude after 3 months of follow-up, most likely due to the formation of glial scar tissue around the DBS lead.

8 Appendix III: High Field Imaging Techniques: Thalamus

This appendix contains excerpts from a submission to Frontiers in Neuroscience Brain Imaging Methods:

Yizi Xiao, Laura M. Zitella, Yuval Duchin, Benjamin Teplitzky, Daniel Kastl, Gregor Adriany, Essa Yacoub, Noam Harel, and Matthew D. Johnson, "Multimodal 7T imaging of thalamic nuclei for deep brain stimulation applications." *Frontiers in Neuroscience.* (In review)

8.1 Introduction

Structural brain imaging has become a valuable tool to guide the implantation and programming of deep brain stimulation (DBS) systems for the treatment of numerous brain disorders [154], [274], [275]. Current clinical magnetic resonance imaging (1.5-3.0T) provides reasonable imaging contrast to identify borders of the globus pallidus and to some extent the subthalamic nucleus [276]. However, clearly demarcating targets within the thalamus, another surgical target of DBS, at these field strengths remains a considerable challenge [182], [277]. Improvement in structural imaging of intra-thalamic nuclei would have important clinical applications given that interventional stereotactic procedures within thalamus have shown marked promise for the treatment of pain [278], essential tremor [279], [280], epilepsy [281], [282], Tourette's syndrome [283], disorders of consciousness [268], with other brain disorder indications on the horizon including schizophrenia [284], [285].

Thalamic nuclei can be difficult to visualize with clinical (1.5-3T) scanners due to inadequate contrast, thus requiring the identification of fixed coordinates based on an internal reference, such as the anterior commissure and posterior commissure plane [286] Several non-invasive imaging approaches have been used to demarcate various thalamic nuclei beyond typical clinical imaging protocols. These include functional imaging

[287]–[290], high-field magnetic resonance imaging [175], [291]–[293], and corticothalamic diffusion-weighted imaging with probabilistic tractography [294], [295][291], [292][296], [297]. Here, we show in seven NHPs that high-field (7T) susceptibility-weighted imaging and high-angular resolution diffusion imaging enable demarcation of intra-thalamic nuclei.

8.2 Methods

8.2.1 Imaging Data Acquisition

High-field magnetic resonance imaging (7T, Magnex Scientific) was performed on seven rhesus macaque monkeys (*macaca mulatta*, 6 female and 1 male, Table 12) at the University of Minnesota's Center for Magnetic Resonance Research using a Siemens console and head gradient insert capable of 80 mT/m with a slew rate of 333 mT/m/s. A customized head coil was developed with 16-channel transmit and 16+6 receive channels, in which 4 coils mounted on top of each subject's head and 2 ear-loop coils were added to enhance signal detection from subcortical structures [187]. Animals were anesthetized (isofluorane, 2.5%) during the imaging sessions and monitored continuously for depth of anesthesia. At the conclusion of the study and in order to validate the magnetic resonance imaging data, two animals were deeply anesthetized with sodium pentobarbital and perfused with phosphate buffered saline followed by a 4% paraformaldehyde fixative solution, consistent with the recommendations of the Panel on Euthanasia of the American Veterinary Medical Association. Similar methods and some of the same subjects were used previously for the study in Chapter 3, described on page 42.

Susceptibility-weighted imaging (SWI) was collected in all subjects (n=7) and consisted of a 3D flow-compensated gradient echo sequence using a FOV of 128 x 96 x 48 mm^3, matrix size of 384 x 288 x 144 (0.3 - 0.4 mm isotropic resolution), TR/TE of 35/29 msec, flip angle of 15°, BW of 120 Hz/pixel, and acceleration factor of 2 (GRAPPA) along the phase-encoding direction. Additionally, diffusion-weighted imaging (DWI) was collected and analyzed in a subset of subjects (n=3). DWI consisted of a single refocused 2D single-shot spin echo EPI sequence [188][3], matrix size of 128 x 84 x 50 (1 mm isotropic resolution), TR/TE of 3500/53 msec, flip angle of 90°, BW of 1860 Hz/pixel, and an acceleration factor of 3 (GRAPPA). Diffusion-weighted images (b-value = 1500 s/mm^2) were collected with diffusion gradients applied along 55-143 uniformly distributed directions [298]. Fifteen additional non-diffusion-weighted images (b=0 s/mm^2) were acquired for every 10 diffusion-weighted images. We utilized TOPUP [189] in FSL to correct for geometric distortions in the EP images due to magnetic field inhomogeneities. This approach used multiple non-diffusion-weighted (b0) scans with bidirectional (posterior-anterior and anterior-posterior) phase-encoding directions to calculate and counteract the deformation field.

Subject	Gender	Age	Resolution (mm)			DWI
			T1-W	T2-W	SWI	
1	F	22	0.667 iso	0.4x0.4x0.7	0.4 iso	
2	F	22	0.667x0.667x0.33	0.4x0.4x0.8	0.4 iso	
3	F	14	0.5 iso	0.33 iso	0.33 iso	
4	F	13	0.5 iso	0.5 iso	0.4 iso	«
5	F	10	0.667x0.667x0.7	0.4x0.4x0.8	0.4 iso	«
6	F	9	0.5 iso	0.5 iso	0.4 iso	
7	M	4	0.5x0.5x0.249	0.4x0.4x0.8	0.33 iso	«

Table 12. Subject characteristics and imaging protocols.
(iso: isometric, DWI: diffusion weighted imaging, SWI: susceptibility-weighted imaging)

8.2.2 Diffusion Tensor Imaging

Fiber tractography was performed in FSL [193]–[195] for three subjects (M4, M5, and M7) to extract several fiber tract pathways projecting into thalamus. SWI images were converted into NIfTI files (dcm2nii) and imported into the brain imaging analysis software platform, FSL. The FSL automated brain extraction tool (BET) [196] was used to remove the skull in the images. A 7-DOF FLIRT [197]–[199] linear transformation in FSL was used to obtain an alignment between the SWI and diffusion data. Since these two imaging modalities differ, inter-modal cost functions (correlation ratio, mutual information-based options) were applied. Before computation of tractography, the diffusion data was pre-processed using *bedpostx* to estimate the diffusion parameters. Seed point and waypoint masks, based upon the warped atlas, were defined in the SWI images to extract the following white mater tracts: the medial lemniscus (ML) projecting into the ventralis posterior lateralis pars caudalis (VPLc) nucleus of thalamus, the superior cerebellar peduncle (SCP) projecting into ventralis posterior lateralis pars oralis (VPLo) nucleus of thalamus, and the pallidofugal (PF) tract projecting into ventralis lateralis pars oralis (VLo) and ventralis anterior (VA) nuclei of thalamus [299]. To estimate the ML tract, seed points were placed in the ML representation of the caudal pons, and a waypoint was introduced as the entire region of the thalamus anterior to the pulvinar. Similarly, the SCP tract was extracted by placing seed points in the posterior pons, with waypoints at the decussation of SCP, and the entire thalamus. Two subjects (M5 and M7) required an additional seed point in the red nucleus. The PF tract was reconstructed using masks over the entire GPi with a waypoint at the thalamus. These masks were transformed into DWI space using the previously calculated transformation and were used for computing the probabilistic tractography (*probtrackx*). Once completed, the resulting tracts were inversely transformed back into SWI space for 3D visualization using the biomedical computer aided design software, Amira.

8.3 Results

8.3.1 Probabilistic tractography of ascending tracts to ventral nuclei in thalamus

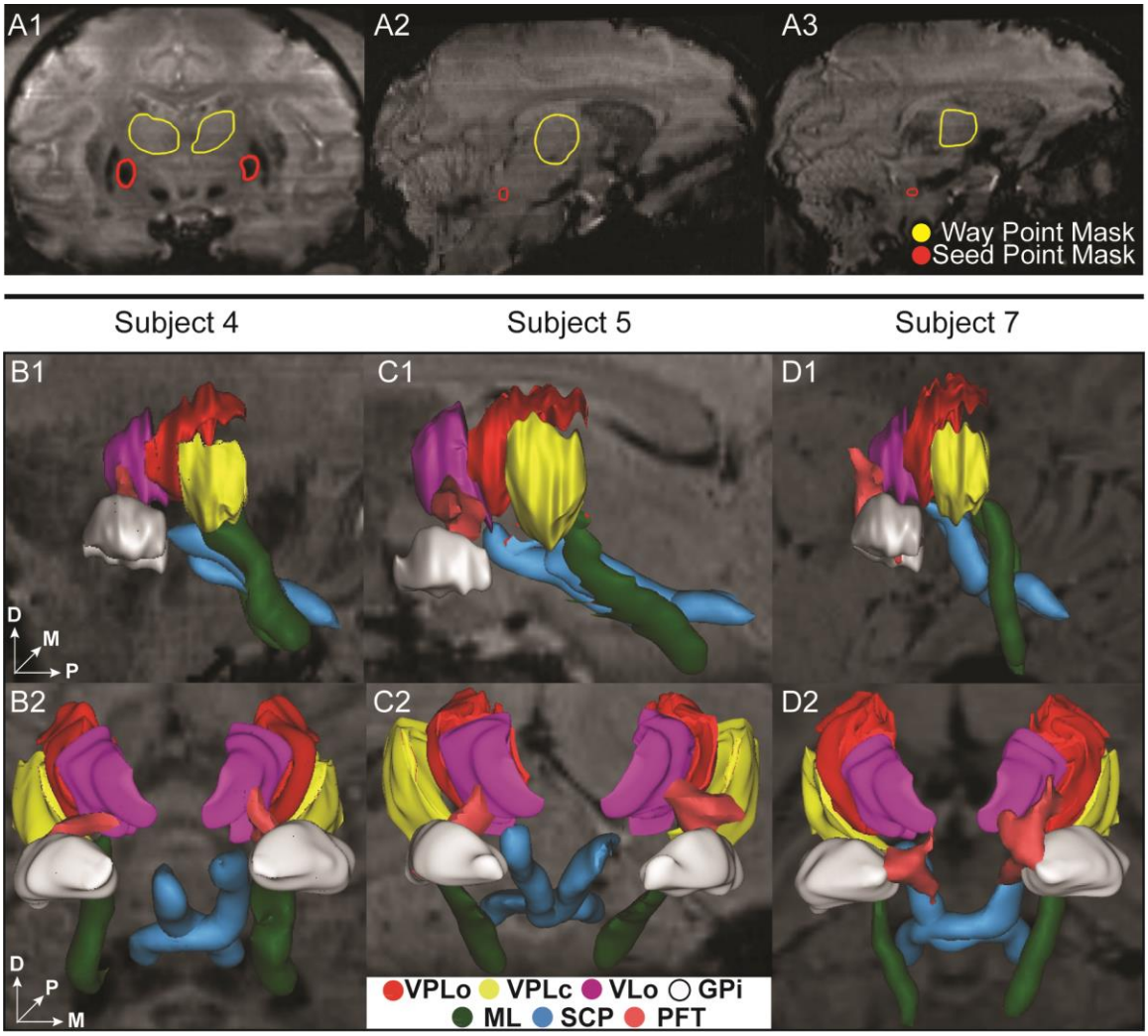

Figure 36. Ascending fiber tractography to the ventral nuclei of thalamus in three subjects.
A1-A3. Examples of seed point (red) and waypoint (yellow) masks used in the probabilistic tractography. A1. Seed point mask in GPi and waypoint mask in thalamus for reconstruction of the PF tract. A2. Seed point mask of SCP in brainstem and waypoint mask in thalamus for reconstruction of SCP. A3. Seed point mask of ML in brainstem and waypoint mask in thalamus for reconstruction of ML. B-D. Bilateral probabilistic fiber tractography reconstructions for the PF, SCP, and ML tracts and their corresponding thalamic nuclei. The nuclei of the oral (VPLo) and caudal (VPLc) parts of the ventral posterolateral nucleus are reconstructed from series of warped atlas plates. A: anterior, V: ventral, M: medial, D: dorsal, P: posterior.

While most regions of thalamus exhibited contrast sufficient to segment manually or to guide the placement of markers for the nonlinear atlas deformation algorithm (described on page 46), the internal borders of the ventral nuclei were not clearly distinguishable

from the SWI. In this case, fiber tractography was used to estimate the ventral nuclei demarcations based upon thalamic afferents coursing along the medial lemniscus (to VPLc), superior cerebellar peduncle (to VPLo), and globus pallidus (to VLo/VA) in three subjects (M4, M5, and M7). The resulting fiber tracts were spatially co-registered to the SWI data and the reconstructed thalamic nuclei. In the case of the ML and PF tracts, the fiber tractography was able to identify the ventral entry point to VPLc and VLo in all three subjects (Figure 36). In the case of the SCP tract, the tractography reconstructions were found to project into or just ventrally adjacent to the VPLo.

8.4 Discussion

8.4.1 Demarcation of the ventral nuclei using probabilistic tractography

Previous studies have found considerable variability in the location of generic atlas-based target points in thalamic nuclei in relation to major neighboring fiber tracts in individual patients, suggesting the need for individualized methods that can target structures not directly visible on conventional MRI [300]. One approach to subject-specific mapping of thalamic nuclei includes probabilistic fiber tractography for reconstructing white matter pathways [301] into the thalamus including those originating from globus pallidus internus (PF tracts) [289] and cortex [294]. Here, we extend these studies showing nearly complete demarcation of the ventral nuclei utilizing ascending ML, SCP, and PF fiber tracts. This approach provided important data to verify the atlas plate to SWI slice alignment for the anterior portion of the thalamus. The trajectories of the fiber tracts projecting into the subject-specific ventral nuclei reconstructions (i.e. VPLc, VPLo, and VLo/VA) were consistent across the three subjects.

8.5 Acknowledgements

This work was supported by grants from the National Institutes of Health (R01 NS081118, R01 NS085188, P41 EB015894, P30 076408, and the Human Connectome Project U54 MH091657) and the National Science Foundation (IGERT DGE 1069104 to LZ and GRFP 00006595 to BT).

9 Appendix IV: Corticospinal Tract Tractography in NHP

9.1 Introduction

The internal capsule lies lateral to the subthalamic nucleus (STN) and is an important consideration during deep brain stimulation (DBS) in the STN for treating Parkinson's disease (PD), as stimulation can cause tonic muscle contraction. The corticospinal tract fibers are somatotopically organized within the internal capsule, projecting to different areas of motor cortex. The top image in Figure 37 shows the results of radiotracers injected into the different somatotopic areas of the motor cortex (foot, trunk, hand, face) in the rhesus macaque [302]. The somatotopic organization within the internal capsule is also visible. This study aimed to determine if the different areas of the corticospinal tract could be identified via probabilistic diffusion tractography in an NHP.

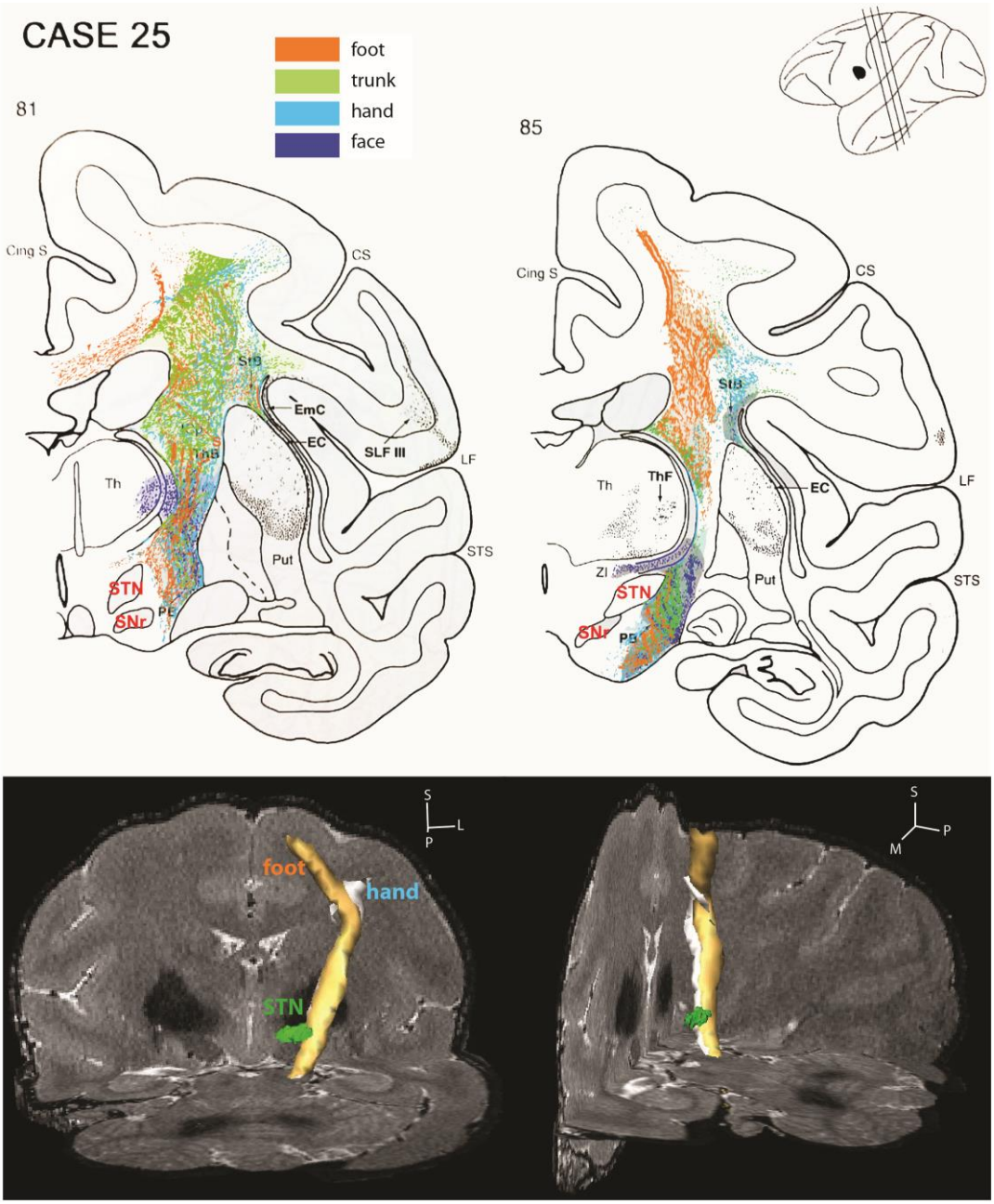

Figure 37. Somatotopic organization of the corticospinal tract and resultant fiber tractography. (Top) Somatotopic organization of the corticospinal tract in the rhesus macaque was determined from injections of radiotracers in the somatotopic areas of the motor cortex. These images are adapted from Schmahmann and Pandya 2006 [302] with permission from Oxford University Press. (Bottom) The top images were used to guide the seed points to identify different regions of the corticospinal tract using probabilistic tractography. The STN is shown in green with the hand region of the corticospinal tract identified in white and the food region of the corticospinal tract identified in yellow.

9.2 Methods

The methods of probabilistic tractography using FSL, as described in Appendix V on page 140, were followed for this study. Separate seed masks were defined in FSL for both the foot and hand regions of motor cortex, as defined in Case 25 of the Schmahmann and Pandya book [302]. These seed masks spanned several coronal slices. A waypoint region was defined as the internal capsule slightly posterior to STN. These seed masks, converted into diffusion space, were then utilized in the FDT Diffusion ProbtrackX Probabilistic tracking function in FSL to predict the corresponding tracts. These tracts were then converted back into T2 MRI space, exported as NIfTI files, and imported into Amira for 3D visualization and alignment with the histology and DBS lead placement.

9.3 Results

The foot and hand regions of the corticospinal tract were able to be identified in one rhesus macaque (Figure 37). The foot region of the corticospinal tract was found to overlap with the hand region of the corticospinal tract at the level of the STN, but extend slightly more posterior. This positioning continued until cortex where the hand and foot regions were clearly separable in both animals. Since it is possible to identify the different somatotopic regions of the corticospinal tract, this method may be useful to develop subject-specific computational models of STN DBS for evaluation of stimulation settings to avoid side effects.

10 Appendix V: Probabilistic diffusion tractography

The following protocol describes how to define fiber tracts using probabilistic tractography in the FSL program using MRI and diffusion-weighted imaging.

Setting up FSL

1. Follow instructions to download the program, FSL, at: http://fsl.fmrib.ox.ac.uk/fsl/fslwiki/FslInstallation
    a. FSL must be run on a Unix system. To run on a Windows machine use VMware Player.
2. To load MRI and diffusion-weighted imaging the files must be in the NIfti (.nii) format. Download a converter, mricron, at: (http://www.mccauslandcenter.sc.edu/mricro/mricron/)
    a. Use DICOM to NIfti (dcm2nii) GUI to convert your DICOM image files (T2, SWI, etc.) to NIfti files.
3. Once you've logged into your virtual machine (VMWare if on PC), you can drag and drop your .nii images onto the virtual machine desktop.
4. Open the terminal and type: fsl
    a. This will open up the FSL GUI, available for some functionalities of the FSL program, the rest will need to be typed into the terminal

Pre-processing of Data

5. Pre-processing of the data first needs to be done to eliminate distortion, including: bedpostx (needed to run tractography), dtifit (not needed to run tractography, but calculates diffusion tensors, fractional anisotropy, etc.), eddy current correction
    a. All found under the FDT diffusion tab of the GUI
    b. To run bedpostx (~15 hours): FDT diffusion→BEDPOSTX Estimation of diffusion parameters in drop-down menu→Input diffusion data

Probabilistic Tractography

Segmentation of Masks

6. First need to segment masks of interested in your highest resolution images. These masks will be set as either seed points (where the tract originates), waypoints (an area the tract courses through), or endpoints (where the tract terminates)
    a. Open FSLView, and Open→.nii data set
    b. File→Create Mask→Click on pencil icon in toolbar→Color in on each slice the region of interest→File→ Save as.. to save mask

Co-registration of Data Sets

7. Begin by extracting the brain region from the skull by running the BET brain extraction command.
    a. Select BET from the GUI, input .nii image and specify output image path. Increase or decrease the fractional intensity threshold value to crop more or less of the skull and brain
        i. Other options are available to improve the extraction, including the bias field & neck cleanup, etc. options in drop-down menu
    b. Examine BET output in FSLView to verify a good brain extraction was completed.
8. To linearly register the anatomical images to the diffusion images, use the FLIRT linear registration function (on GUI). More information can be found here: http://fsl.fmrib.ox.ac.uk/fsl/fslwiki/FLIRT/FAQ http://fsl.fmrib.ox.ac.uk/fslcourse/lectures/reg.pdf
    a. Set the reference image to the B0 diffusion data after pre-processing.
    b. Set the input image to the anatomical imaging dataset that you segmented masks in.
    c. Specify the path for the output image (folder and name of transformed image)
    d. The degrees of freedom (DOF) choice depends on whether the registration is inter/intra-subject and of a small/large field of view (FOV)
        i. Use 6 DOF for large FOV
        ii. Use 3 DOF for small FOV/single slice

iii. If scanner voxel size may have changed (due to calibration shifts) to compensate for global scale changed use 7 DOF instead of 6 or 4 DOF instead of 3.
iv. When images are of different subjects (or registering to standard space) use: 12 DOF for large FOV or 6 DOF for small FOV.

e. If the result is a bad registration, explore the Advanced Options. Also keep in mind the following:
   i. If registering two images of different modalities you must use an inter-modal cost function (correlation ratio, mutual information-based options).
   ii. If registering images for the same modality, either can be used but intra-modal options may be more accurate (least squares, normalized correlation).
   iii. In the Search section, specify whether the images are already aligned, not aligned but same orientation, or not in same orientation.
   iv. For interpolation method, tri-linear and nearest neighbor seem to work best.
f. FLIRT will output a .mat file with the transformation matrix along with transformed image set.

Verifying and Adjusting Registration

9. Verify the transformation is accurate by applying the transformation to the segmented masks and overlaying them on top of the data set they were aligned to.
   i. Use the "Apply FLIRT Transform" function to apply the transformation, located: FLIRT→Utils→Apply FLIRT Transform (applyXFM)
   ii. Set the paths for the transformation matrix, mask, reference volume, and output volume (transformed volume)
   iii. Visualize the output volume in FSL View on the image set and verify the location of the masks. Note that the transformed segmentations will no longer have well defined borders, as different voxels will have different intensity values associated with them. Use the crosshair to click on a voxel and look at the intensity value in the lower left corner.
      1. To refine the border of a mask use the fslmaths function in the terminal. This will threshold to the specified intensity value (lower threshold more liberal border, higher threshold more conservative border). This must be called from the terminal, for example: fslmaths unthresholdedmask.nii.gz –thr 0.9 –bin thresholded_mask.nii.gz

b. If transformed mask location is not accurate, redo FLIRT. Use a nonlinear (FNIRT in FLS or ANTS program) transformation if the linear results are not satisfactory. If calculating a non-linear transformation from FNIRT or

ANTs program, use the whole brain as the input (not the brain extracted) and use the brain mask to let the algorithm 'know' where to put less weight

Probabilistic Tractography

10. The next step is to compute the probabilistic tractography, located under the FDT Diffusion section of the GUI: FDT Diffusion→ProbtrackX Probabilistic tracking.
    a. The BEDPOSTX directory is the entire folder that was the output of BedpostX
    b. Specify whether the seed space is a single voxel, single mask, or multiple masks and set the path to the masks.
    c. Specify the path to any waypoints, exclusion, or termination masks
    d. Specify the output directory path and run. Output is in the .nii file format.
11. Once the tractography has completed inverse transform the output (using Invert FLIRT Transform then Apply FLIRT Transform) to put the tracks into the anatomical MRI space.
12. Tracts (.nii files) can be imported directly (dragged and dropped) into Amira or Avizo for 3-D visualization along with other segmented nuclei and MRI.
13. These tracts can then be thresholded and saved as .stl files.

Generate Contours for Models from Tract .STL files

14. Import .STL file of the tract reconstruction into Rhino3D.
15. To create contours:
    a. Curve→Curve from Objects→Contour
    b. If prompted, select the tract.
    c. When prompted, select a point at the end of the tract.
    d. When prompted, select a direction approximately tangential to the length of the tract.
    e. When prompted for a distance, enter a number (in mm) for the distance between slices.
    f. Move curves to their own layer.

11 Appendix VI: PPN cell models

11.1 Co-registering Images

If developing atlas-based computational models, the geometry will be generated from atlas images, which can be directly imported into Rhino for segmentation and lofting into 3D volumes. However, the geometry of subject-specific computational models is generated from clinical images. There are a number of imaging modalities incorporated into these models, including but not limited to, CT, T1-W MRI, T2-W MRI, proton density images, SWI, and DWI. If utilizing multiple imaging sequences, all image sets must be co-registered into the same space (typically AC-PC space). If utilizing probabilistic diffusion tractography to incorporate anisotropic conductivity into the

model, all image sets must be co-registered into the space of the DWI, as the transformation of diffusion tensors is difficult and may create errors.

Co-registration can take place in a number of different programs. The protocol for using Amira will be described here. Image sets can be imported into Amira in the DICOM or NifTi format. To smooth the images, utilize the bilinear view. If a crisper image is desired, the PD image set can be utilized, dividing the T1-W images by the proton density images. An arithmetic function in Amira can achieve this. Connect the arithmetic function to both the T1-W and PD image sets so that T1-W images are input A and proton density images are input B. In the properties, set the results channels to 'like input A'. Set the expression to: (A/B)*10000*(B>500).

The first step involves extracting only the brain region (eliminating all images that include the skull). Create brain masks from each imaging dataset by using the threshold feature in the segmentation editor. If threshold is not producing satisfactory results use the brush tool to manually outline the brain. Then use the fill function to fill in the slice. Navigate to a few slices away and outline the brain again. Use the interpolate function to interpolate between the two slices. Other functions under the selection category can be used to achieve the most accurate brain mask. The brain will be isolated in each imaging dataset by multiplying the imaging dataset by the brain mask. These isolated brains can now be registered to each other and brain regions can be segmented.

11.2 Generating 3D Geometry from Nonlinear Warping Algorithm

Due to the lack of contrast in the brainstem region, the nonlinear warping algorithm must be utilized in MATLAB to identify the borders of nuclei in the region, including PPN. First, .JPG images must be created for each MRI slice and corresponding atlas slice in the region of interest. If the atlas only shows half of the brain, the program can be used to mirror half of the brain to create an image of the full brain (MergeAtlasHalves.m). If not warping the entire brain, the atlas and MRI images can be cropped to the region of interest to reduce computational time.

Determine the MRI slice that exactly matches the first and last atlas slices and calculate the corresponding left and right weights for each slice (sliceComparer.m). These weights are then used to generate the MRI images that exactly match all the atlas slices between the first and last slice (MRIgenerator.m). Points will then be placed around the atlas slice (addpPts.m). Corresponding points are placed around the MRI slice (addqPts.m). The warping algorithm uses these points to warp the atlas image to the MRI (secondWarp.m), outputting the warped atlas image.

These warped atlas images are imported into Rhino to create a 3D geometry. First, the size of each atlas slice must be calculated and a rectangle of this size should be created in the front view of Rhino. Each atlas slice will then be placed in Rhino on this rectangle (Right click→Background Bitmap→Place). Create a layer for each nuclei or fiber tract with a sublayer for each slice number that the particular nuclei or fiber tract is present. Outline each nuclei or fiber tract using the InterpCrv command. For each slice and

structure outlined, be sure that the correct layer is selected as the current layer. Once all structure contours are made for all atlas slices, move the contours for each slice, spaced accordingly to atlas slice thickness (Transform→Move). Use the Loft command to create a 3D object from the contours and the Patch command to close the volume.

Now that slices are in the correct location, generate contour point text files. Select a contour and divide the contour into 100 points (Curve→Point Object→Divide Curve By... →Number of Segments→Select Curve→Enter 100). Deselect the contour, select all points along the curve, and Export Selected as a text file. Repeat for all contours in the region of interest.

11.3 Building PPN cell models

Camera lucida drawings of PPN cell type I and II morphologies [36] have been reconstructed in Rhino as a set of 3D points. Place these cells within the PPN volume such that the axons are projecting to thalamus, SN, and down to the spinal cord (relative to other segmented structures). There should be 13 layers for PPN type I (ChAT negative cells) and 15 layers for PPN type II (ChAT positive cells) in the Rhino files. After these cells are placed correctly, save each layer's points as a .TXT file, named as the name of the layer (i.e. axonTh.txt). Rhino does not save these points in order in the .TXT file, so the points will need to be sorted in ascending or descending order in MATLAB, based on the position of the points.

Histology slices from Lavoie et al. were imported into Rhino, where the soma positions of PPN type I (1139 cells) and type II (1154 cells) cells were extracted from multiple slices and saves as points files [26]. These sets of soma positions for both type I and type II cells (PPN_Type1_somapts and PPN_Type2_somapts) should be placed within the subject-specific PPN loft in Rhino. Once soma points are placed, select all the points for each cell type and export the selected as a .TXT file. These points, along with the cell morphology points will be used in MATLAB to create the models.

The MATLAB files necessary to build the cell geometry includes the main code (ppn_populate_Type2.m) as well as other functions (ppn_1_neuronpop_struct_vfinal.m, ppn_print2hoc.m, spreading_soma.m, ppn_2_translate.m). The main code file may be used for both cell types, but the file names will need to be changed. The necessary text files include the soma positions, a text file for each component of the axon/dendrite/soma geometry, and the contour point text files for each slice of the PPN volume. Update the code within the main code file to include the names of these files and run the file in MATLAB. This code will read in the location of the axons, dendrites, and somas from the text files and sort the points so that they will be plotted in order. It will then divide the neuronal reconstruction from Rhino into reconstructed neuronal segments (NODE, MYSA, FLUT, STIN) and calculate the midpoint of each segment. Then, the soma points are spread throughout the PPN volume. Check the figure for accuracy and adjust the spreading parameters to fill the PPN volume (spreading_soma.m). The midpoints calculated in the previous step are then translated to each soma position, creating a cell

model at each soma position. This information is saved in a .mat file that will be used to run the Python with Neuron code.

11.4 FEM with anisotropic tissue conductance

Based on the paper by Tuch et al., brain tissue conductance values can be linearly correlated to diffusion tensor eigenvalues with a scaling factor of 0.844. The output of dtifit in FSL (see Appendix V) contains the eigenvalues and eigenvectors necessary to compute the corresponding conductance values. Download the appropriate MATLAB script from the NRTL Intranet (i.e. calcConductance_Tuch.m) and update the paths to the subject's L1, L2, L3 (1^{st}, 2^{nd}, and 3^{rd} eigenvalues) and V1, V2, V3 (1^{st}, 2^{nd}, and 3^{rd}, eigenvectors). This code will then calculate the conductance values and save them in a .TXT file.

To incorporate the conductance values calculated from the DTI into the COMSOL model, import the conductance value text file into the COMSOL model as an interpolation variable. Under functions, define six functions named xx, xy, xz, yy, yz, and zz, specifying their positions in the file as 1, 2, 3, 4, 5, and 6, respectively. Choose the nearest neighbor interpolation method and set the extrapolation to a specific value of 0.3. Be sure to specify the units of the arguments (mm) and function (S/m). Use the function names to define the brain tissue electrical conductivity properties as a 3x3 matrix: {xx,xy,yy,xz,yz,zz}.

For a subject-specific model, extract lead location in MIMICS or Amira from histology or CT that is co-registered to the subject's DWI dataset. Save the segmented lead as a .STL file. Also segment a rough 3D mask of the brain and save as a .STL file. Build the necessary DBS lead in COMSOL (or download lead design template from intranet if already made). Import the subject specific lead location .STL file into the COMSOL model. Translate and rotate the lead geometry until it is aligned with the subject-specific lead location. Next, import the 3D brain mask and translate and rotate chamber and brain ellipsoid until it roughly matches the brain mask.

Use MATLAB with COMSOL to compute the voltage values at each compartment of each PPN cell for each electrode configuration (MSI_RunFEM_Laura.m). Active cathodes, anodes, and grounds can be set in MATLAB with COMSOL using the surface numbers of each electrode contact in the COMSOL model. Load the cell geometry .mat file and run the FEM for each configuration. Save these voltage values as a structure field called voltage in the .mat file that also contains the compartment information from the previous step.

11.5 Running NEURON models on MSI

Set up the GitHub and install Python and NEURON on MSI account. Modify the python file (pushpull.py) as necessary for your simulation. For example, change the names of data files to match the .mat file generated in MATLAB. Specify the name of the stimulus pulse filename. This code starts with a 136 Hz waveform file and converts the waveform

to the frequency of choice. Specify the frequency as an input to the StimulusTrain function. Create a .PBS file to run the code on MSI. It may be similar to the following (editing everything in italics):

#!/bin/bash –l
#PBS –l walltime=*24:00:00*,pmem=*2580mb*,nodes=*9*:ppn=*24*
#PBS –m abe
#PBS –M *email address*
#PBS –o *pathway for output file (axon_out.txt)*
#PBS –e *pathway for error file (axon_error.txt)*
unset DISPLAY
cd *pathway to simulation folder*
module load python-epd
mpirun python *pushpull.py*

Copy the pushpull.py python file, .mat file, and .pbs file to MSI and submit the PBS job with SSH on MSI. It may be necessary to test the code in an interactive session with SSH first, allowing the observation of any errors before running an entire batch.